8-2023

Cislunar Navigation Techniques and Navigation Performance Optimization

Quinn P. Moon
Utah State University

CISLUNAR NAVIGATION TECHNIQUES AND NAVIGATION PERFORMANCE OPTIMIZATION

by

Quinn P. Moon

A thesis submitted in partial fulfillment
of the requirements for the degree

of

MASTER OF SCIENCE

in

Aerospace Engineering

Approved:

David Geller, Ph.D. Major Professor	Matthew Harris, Ph.D. Committee Member
Todd Moon, Ph.D. Committee Member	D. RichardCutler,Ph.D. Vice Provost of Graduate Studies

UTAH STATE UNIVERSITY

Logan, Utah

2023

ABSTRACT

Cislunar Navigation Techniques and Navigation Performance Optimization

by

Quinn P. Moon, Master of Science

Utah State University, 2023

Major Professor: David Geller, Ph.D
Department: Mechanical and Aerospace Engineering

Houston-based company Intuitive Machines plans on sending the first commercial lander, the NOVA-C, to the lunar south pole in 2023. Through various navigation techniques, including Monte Carlo analysis and Linear Covariance (LinCov) analysis, inertial estimation has been performed for various key mission segments. LinCov studies have demonstrated that selecting diverse geographic stations in tracking schedules significantly impacts navigation performance. This research outlines the effort undergone to create optimal ground station tracking schedules to reduce estimation errors for key mission segments. LinCov analysis is used to determine optimal placement of constrained range measurements given a range-rate tracking schedule. As the lander's position and velocity contribute the largest errors, the dynamic measurement geometry is analyzed with a Dilution of Precision (DOP) algorithm. The DOP algorithm is derived to implement both range and range-rate measurement data by incorporating a measurement noise ratio. The DOP algorithm is analyzed recursively and set within a genetic algorithm. Optimal ground station tracking schedules are found for each OD segment with respect to position errors and Nav-Dollars, a metric derived from analyzing the trade-off between operational costs and navigation performance.

(156 pages)

PUBLIC ABSTRACT

Cislunar Navigation Techniques and Navigation Performance Optimization

Quinn P. Moon, Master of Science

Nova-C is a lunar lander developed by the private company Intuitive Machines to deliver commercial payloads to the Moon. The IM-1 mission set for 2023 will launch and land the Nova-C near the Moon's south pole. In this research, various navigation techniques are explored to determine the lander's position and velocity during key segments. This process is studied for key mission events including trajectory correction maneuvers (TCMs), lunar orbit insertion (LOI), and descent orbit insertion (DOI). Each mission segment, referred to as an Orbit Determination Segment (OD), is analyzed with three different navigation techniques: Monte Carlo Analysis, Linear Covariance Analysis, and Dilution of Precision Analysis. The results are matched against each other to validate consistency. The quicker navigation techniques, specifically Linear Covariance and Dilution of Precision, are implemented into a genetic algorithm to determine optimal ground station tracking schedules. Said optimal schedules are optimal with respect to various objectives, including final position errors and operational costs. Operational costs and navigation errors are combined to form a new metric, referred to as Nav-Dollars, that analyzes the trade off between real costs and estimation performance.

ACKNOWLEDGMENTS

Intuitive Machines has been a driving force for the ideas and requirements presented in this research. Many individuals have been influential and a pleasure to know. First, the navigation team: Sam Welsh, Don Kuettel, and Shen Ge. Second, the executives and leaders at IM: Tim Crain, Shaun Stewart, and John Graves. I am incredibly grateful for the time and research funding they have provided for this work, along with their kind mentor-ship.

A special thanks to Joel Getchius at Blue Origin for his initial research into generalized Dilution of Precision and background on ground station optimization. Additional thanks to Carlos Roithmayr at NASA for providing his insight and tools to implement higher order gravity terms. Without his contributions, the work done to implement higher order gravity gradients would have delayed taken significantly more time.

I would like to acknowledge all of my professors at USU during my 5 years here, but none more than those on my committee: Dr. Geller, Dr. Harris, and Dr. Moon. To Dr. Moon for teaching one of my favorite math classes of all time and for expanding my knowledge of mathematical methods and signal processing more than I ever thought possible in a four month period. To Dr. Harris for employing me as a Teaching Assistant, for teaching me the principles of optimization, spacecraft guidance, and astrodynamics. Without these topics being taught to me by Dr. Harris significant work done in this thesis would not have been possible.

Lastly to my major professor, my advisor, and good friend Dr. Geller. With all the kindness in the world, Dr. Geller took a second year undergraduate student and mentored him to the student I am today. His contribution, friendship, and time have been the most important aspects of my life for years and his impact will change my career and life for the foreseeable future.

(Quinn P. Moon)

CONTENTS

Page

ABSTRACT . . . iii

PUBLIC ABSTRACT . . . iv

ACKNOWLEDGMENTS . . . v

LIST OF TABLES . . . ix

LIST OF FIGURES . . . xi

NOTATIONS . . . xiii

1 INTRODUCTION . . . 1

2 LITERATURE SURVEY . . . 3
2.1 Estimation and Navigation . . . 3
2.1.1 Batch Least-Squares and Dilution of Precision . . . 3
2.1.2 Kalman Filtering and Linear Covariance Analysis . . . 7
2.2 Ground-Based Navigation . . . 8
2.2.1 Measurements . . . 8
2.2.2 Ground Station Tracking Schedule . . . 9
2.3 Optimization Techniques . . . 10

3 MONTE CARLO SIMULATION MODELS . . . 12
3.1 Monte Carlo Procedure . . . 13
3.2 State Vector . . . 14
3.3 Measurement Information . . . 15
3.4 Extended Kalman Filter . . . 19
3.4.1 State Differential Equations . . . 19
3.4.2 Filter Covariance Propagation . . . 22
3.4.3 Filter Covariance and State Updates . . . 26
3.5 Monte Carlo Performance . . . 26

4 LINEAR COVARIANCE ANALYSIS . . . 27
4.1 Linearized Kalman Filter . . . 27
4.1.1 State Vector . . . 27
4.1.2 Dynamic Linearization and Covariance Propagation . . . 28
4.1.3 Linearized Measurements and Covariance Update . . . 30
4.2 Linear Covariance Performance . . . 30

5 LINEAR COVARIANCE VALIDATION WITH MONTE CARLO ANALYSIS . . . 31
5.1 Reference Trajectory, OD Segments, Contact Schedule . . . 32
5.2 Cislunar Simulation Setup . . . 34
5.3 Cislunar Results . . . 35
5.4 Lunar Orbit Simulation Setup and Values . . . 42
5.5 LLO Results . . . 43
5.6 Validation Discussion . . . 47

6 OPTIMAL RANGE PLACEMENT WITH LINEAR COVARIANCE . . . 48
6.1 Problem Overview . . . 49
6.2 1 Segment Range Optimization . . . 50
6.2.1 Optimization Variables and Considerations . . . 50
6.2.2 One Segment Results . . . 51
6.3 Two Segment Range Optimization . . . 55
6.3.1 Optimization Object Properties with 2 Range Segments . . . 55
6.3.2 Two Segment Results . . . 56
6.4 Optimal Range Measurement Discussion . . . 59

7 DILUTION OF PRECISION METHODS . . . 60
7.1 Generalized Dilution of Precision . . . 60
7.2 Computational Efficiency and Recursive Methods . . . 63
7.3 Condition Number Implementation . . . 64
7.4 DOP with Multiple Measurement Types . . . 66
7.5 DOP Validation Through LinCov . . . 69
7.6 DOP for Ground Station Optimization . . . 70

8 POSITION DILUTION OF PRECISION: OPTIMAL TRACKING SCHEDULES . 71
8.1 Objective Functions and Optimization Objects . . . 71
8.1.1 Position Dilution of Precision . . . 72
8.1.2 Continuous PDOP Optimization Object . . . 73
8.2 Optimization Procedure . . . 75
8.2.1 Genetic Algorithm . . . 75
8.2.2 Visibility Report . . . 77
8.2.3 Number of Stations Implemented . . . 79
8.3 Optimal PDOP Tracking Schedules: Cislunar Space . . . 81
8.4 Optimal PDOP Tracking Schedules: Lunar Orbit . . . 89
8.5 PDOP Results Analysis . . . 90

9 NEAR-CONTINUOUS NAV-DOLLARS: OPTIMAL TRACKING SCHEDULES . . 91
9.1 Nav-Dollars and Operational Costs . . . 92
9.2 Nav-Dollar Implementation . . . 93
9.3 Cislunar Near-Continuous Nav-Dollars Results . . . 95
9.4 Lunar Orbit Near-Continuous Nav-Dollars Results . . . 109
9.5 Optimal PDOP and Nav-Dollar Comparison and Discussion . . . 111

10 NON-CONTINUOUS NAV-DOLLARS: OPTIMAL TRACKING SCHEDULES . . . 113
10.1 Non-Continuous Optimization Object . . . 114
10.2 Number of Stations Implemented . . . 116
10.3 Cislunar Non-Continuous Results . . . 117
10.4 Lunar Orbit Non-Continuous Nav-Dollar Results . . . 131
10.5 Non-Continuous Discussion . . . 133

11 CONCLUSION AND FUTURE WORK . . . 134
11.1 Monte Carlo and Linear Covariance Analysis . . . 134
11.2 Optimal Range Measurement Placement . . . 135
11.3 Dilution of Precision Methods . . . 136
11.4 PDOP Optimal Schedules . . . 136
11.5 Nav-Dollar Optimal Schedules . . . 137

LIST OF TABLES

Table Page

5.1 Simulation Setup Values 34

5.2 Monte Carlo Simulation Errors 35

5.3 Linear Covariance Errors 36

5.4 Simulation Setup Values: Lunar Orbit 42

5.5 Monte Carlo Simulation Errors: LLO 43

5.6 Linear Covariance Errors: LLO 44

6.1 Optimal 1 Range Measurement Segment Placement: Position RSS 53

6.2 Optimal Range Measurement Segment Placements: Position RSS 58

7.1 DOP and LinCov Comparison: $Q = 1e^{-14}\frac{m^2}{s^3}$ 69

8.1 Optimal PDOP Results: Cislunar Space 88

8.2 Optimal PDOP Schedules: LLO 89

9.1 Optimal PDOP/Nav-Dollar Schedule Comparison: LVS-CM 96

9.2 Optimal PDOP/Nav-Dollar Schedule Comparison: CM-TCM1H 98

9.3 Optimal PDOP/Nav-Dollar Schedule Comparison: TCM1H-TCM1 100

9.4 Optimal PDOP/Nav-Dollar Schedule Comparison: TCM1-TCM2H 102

9.5 Optimal PDOP/Nav-Dollar Schedule Comparison: TCM2H-TCM2 104

9.6 Optimal PDOP/Nav-Dollar Schedule Comparison: TCM2-TCM3 106

9.7 Optimal PDOP/Nav-Dollar Schedule Comparison: TCM3-LOI 108

9.8 Optimal PDOP/Nav-Dollar Schedule Nav-Dollar Comparison: LLO 109

10.1 Nav-Dollar Schedule Comparisons: LVS-CM 118

10.2 Nav-Dollar Schedule Comparisons: CM-TCM1H 120

10.3 Nav-Dollar Schedule Comparisons: TCM1H-TCM1 122

10.4 Nav-Dollar Schedule Comparisons: TCM1-TCM2H 124

10.5 Nav-Dollar Schedule Comparisons: TCM2H-TCM2 126

10.6 Nav-Dollar Schedule Comparisons: TCM2-TCM3 128

10.7 Nav-Dollar Schedule Comparisons: TCM3-LOI 130

10.8 Nav-Dollar (NAVD) Schedule Comparison: LLO 132

LIST OF FIGURES

Figure		Page
2.1	Measurement Geometry	5
3.1	Monte Carlo Analysis	13
3.2	Measurement Generation	15
3.3	N-Body Gravitational Forces	19
5.1	IM-1 Nominal Trajectory	32
5.2	Benchmark Schedule	33
5.3	Inertial Position Errors: CM-TCM1	37
5.4	Inertial Velocity Errors: CM-TCM1	38
5.5	SRP_y Inertial Errors: TLI-CM	39
5.6	Range Biases: CM-TCM1	40
5.7	Range-rate Biases: CM-TCM1	41
5.8	Inertial Position Errors: Orbit 3	45
5.9	Inertial Velocity Errors: Orbit 3	46
6.1	CM-TCM1 Benchmark Tracking Schedule	49
6.2	1D 1hr Optimal Range Placement: CM-TCM1	51
6.3	1D 1hr Optimal Range Placement: TCM1-TCM2	52
6.4	2D 1hr Optimal Range Placement: Position TCM1-TCM2	56
6.5	2D 1hr Optimal Range Placement: Velocity TCM1-TCM2	57
7.1	DOP Algorithm Flow Chart	65
7.2	DOP Algorithm Flow Chart: Multi-Measurement Incorporation	68
8.1	Ground Station Tracking Schedule Optimization Procedure	76

8.2 Visibility Generation 77
8.3 Lunar Occultation 78
8.4 Optimal PDOP Schedule: LVS-CM 81
8.5 Optimal PDOP Schedule: CM-TCM1H 82
8.6 Optimal PDOP Schedule: TCM1H-TCM1 83
8.7 Optimal PDOP Schedule: TCM1-TCM2H 84
8.8 Optimal PDOP Schedule: TCM2H-TCM2 85
8.9 Optimal PDOP Schedule: TCM2-TCM3 86
8.10 Optimal PDOP Schedule: TCM3-LOI 87
9.1 Optimal Nav-Dollar Schedule: LVS-CM 95
9.2 Optimal Nav-Dollar Schedule: CM-TCM1H 97
9.3 Optimal Nav-Dollar Schedule: TCM1H-TCM1 99
9.4 Optimal Nav-Dollar Schedule: TCM1-TCM2H 101
9.5 Optimal Nav-Dollar Schedule: TCM2H-TCM2 103
9.6 Optimal Nav-Dollar Schedule: TCM2-TCM3 105
9.7 Optimal Nav-Dollar Schedule: TCM3-LOI 107
9.8 Optimal PDOP and Nav-Dollar Comparison: CM-TCM1H 111
9.9 Optimal PDOP and Nav-Dollar Comparison: TCM1-TCM2H 112
10.1 Non-Continuous Nav-Dollars: LVS-CM 117
10.2 Non-Continuous Nav-Dollars: CM-TCM1H 119
10.3 Non-Continuous Nav-Dollars: TCM1H-TCM1 121
10.4 Non-Continuous Nav-Dollars: TCM1-TCM2H 123
10.5 Non-Continuous Nav-Dollars: TCM2H-TCM2 125
10.6 Non-Continuous Nav-Dollars: TCM2-TCM3 127
10.7 Non-Continuous Nav-Dollars: TCM3-LOI 129
10.8 Non-Continuous Nav-Dollars: LLO 131

NOTATIONS

$\boldsymbol{a}$	Acceleration Vector
$\boldsymbol{b_r}$	Range Measurement Bias
$\boldsymbol{b_{\dot{r}}}$	Range-Rate Measurement Bias
D	Dyadic Matrix
$\boldsymbol{f}$	Dynamic Vector Function
F	Jacobian of the Dynamics
$\boldsymbol{h}$	Measurement Vector Function
H	Measurement Partial Matrix
$\boldsymbol{i_r}$	Position Unit Vector
$\boldsymbol{i_v}$	Velocity Unit Vector
K	Kalman Gain, Normalized Weighting Matrix
M	Mapping Matrix
P	Navigation Covariance Matrix
T	Rotation Matrix
$\boldsymbol{r}$	Position Vector
$\boldsymbol{s}$	Optimization Object
t	Time
$\boldsymbol{v}$	Velocity Vector
$\boldsymbol{w}$	Process Noise
W	Weighting Matrix
$\boldsymbol{x}$	State Vector
$\boldsymbol{z}$	Measurement Vector

α	General Angle Value
β	General Angle Value
$\boldsymbol{\delta}$	Vector Linearization or Difference
Δ	Scalar Difference
ϵ	Residual
λ	Longitude
ν	Measurement Noise
$\boldsymbol{\omega}$	Rotation Vector
ϕ	Latitude
Φ	State Transition Matrix
$\boldsymbol{\psi}$	Solar Radiation Pressure Vector
σ	Standard Deviation, Singular Value
τ	Range Measurement Time, ECRV Time Constant
θ	General Angle Value
$\boldsymbol{\xi}$	Instance of a Random Variable

The following superscripts, subscripts, etc. will be used throughout on vectors and scalars:

$\boldsymbol{\alpha}^-$	Before measurement Update
$\boldsymbol{\alpha}^+$	After measurement Update
$\dot{\boldsymbol{\alpha}}$	Time Derivative
$\tilde{\boldsymbol{\alpha}}$	Measured Value
$\hat{\boldsymbol{\alpha}}$	Estimated Value
$\boldsymbol{\alpha}^{ECI}$	In the Earth Centered Inertial Frame
$\boldsymbol{\alpha}^{ECEF}$	In the Earth Centered Earth Fixed Frame
$\boldsymbol{\alpha}^{LCI}$	In the Lunar Centered Inertial Frame
$\boldsymbol{\alpha}^{LCF}$	In the Lunar Centered Fixed Frame
$\boldsymbol{\alpha}^{I}$	In an Inertial Frame
$\boldsymbol{\alpha}^{F}$	In a Fixed Frame
$\boldsymbol{\alpha}_{A/B}$	Position, Velocity, Acceleration of body A w.r.t body B
$\boldsymbol{\alpha}_{A,B}$	Acceleration on body A from body B
$\boldsymbol{\alpha}_k$	At Discrete Time k
$\boldsymbol{\alpha}_E$	Relating to the Earth
$\boldsymbol{\alpha}_l$	Relating to the Lander
$\boldsymbol{\alpha}_S$	Relating to the Sun
$\boldsymbol{\alpha}_M$	Relating to the Moon
$\boldsymbol{\alpha}_{St}$	Relating to a tracking station

CHAPTER 1

INTRODUCTION

The Houston-based company Intuitive Machines (IM) is set to launch and land its NOVA-C Lander on the lunar surface in 2023. Various studies have been performed for IM by Utah State University. These studies have included trajectory dispersion analysis, trajectory navigation analysis, and trajectory correction maneuver planning.

As the launch approaches, an increasing interest has been generated in the navigational ability and performance of the current ground station tracking system. The success of the Guidance, Navigation, and Controls (GN&C) team critically depends on the precision and accuracy of the state estimate for maneuver planning and ultimately lunar landing. Various efforts has been made to study and validate the navigation performance through Monte Carlo simulations and Traditional Linear Covariance (LinCov) analyses.

Observations during these navigation studies has shown the importance of the diversity and availability of ground stations in developing a ground station tracking schedule. Furthermore, the more recent development of a Recursive Dilution of Precision (DOP) Tool has further demonstrated that some ground station tracking schedules provide better estimation solutions than other schedules.

This research studies how navigation tools have been utilized in the past and develops new navigation tools that can provide optimal tracking schedules for future lunar missions. The document begins by providing a literature search into various navigation and optimization techniques and how these may be applied to cislunar estimation. The document then dives into three different navigation techniques: Monte Carlo Analysis, LinCov Analysis, and DOP Analysis.

The Monte Carlo analysis is used to analyze the precision of the true navigation errors using an Extended Kalman Filter (EKF) based on the dynamics of the cislunar problem and Earth-based ground tracking stations. Through linearization about the nominal trajectory,

LinCov provides a faster alternative to analyze the estimation errors and is validated through the Monte Carlo results. By focusing on the dominant error sources from the lander's position and velocity, a recursive DOP algorithm is derived to analyze the dynamic measurement geometry. The DOP analysis is validated by a LinCov analysis, and both algorithms are used to find optimal tracking schedules according to various parameters for the IM-1 mission.

CHAPTER 2
LITERATURE SURVEY

2.1 Estimation and Navigation

Spacecraft Navigation is the process of incorporating measurements in order to determine the spacecraft's state [1]. Navigation and guidance algorithms work together to provide accurate estimates and subsequent targeting maneuvers for mission success. Associated with state estimation is the estimation error, quantified traditionally with the State Error Covariance. Various methods and equations have been derived and used for spacecraft navigation and are explored in the literature search below.

2.1.1 Batch Least-Squares and Dilution of Precision

Systems that have a minimum of n measurements to estimate an n-dimension state vector to estimate the state are referred to as deterministic solutions [2]. An example of solving for the state using measurement data in a deterministic system is shown below:

$$\boldsymbol{z}_{n\times 1} = H_{n\times n}\boldsymbol{x}_{n\times 1} \tag{2.1}$$

$$\boxed{\hat{\boldsymbol{x}} = H^{-1}\boldsymbol{z}} \tag{2.2}$$

However, measurement and dynamic modeling errors persist in all real world systems. Thus, extra measurements are taken and a Least-Squares solution is calculated. The Least-Squares method was first derived by Gauss in 1795 for early spacecraft estimation [3]. Battin provides a detailed derivation of the Least-Squares solution by minimizing the squared of the residuals [2]. Note that for the equations below $m > n$, thus the matrix H is not invertible, and thus

a minimum of the measurement equation residuals is sought.

$$\boldsymbol{z}_{m\times 1} = H_{m\times n}\boldsymbol{x}_{n\times 1} \tag{2.3}$$

$$\epsilon = \boldsymbol{z} - H\boldsymbol{x} \tag{2.4}$$

$$\epsilon^2 = (\boldsymbol{z} - H\boldsymbol{x})^T(\boldsymbol{z} - H\boldsymbol{x}) \tag{2.5}$$

By setting the partial derivative of ϵ^2 (with respect to the state) to zero, the Least-Squares solution is found:

$$\frac{\partial \epsilon^2}{\partial \boldsymbol{x}} = 0 \tag{2.6}$$

$$\boxed{\hat{\boldsymbol{x}} = \left(H^T H\right)^{-1} H^T \boldsymbol{z}} \tag{2.7}$$

Least-Squares navigation solutions have been used for a variety of inner and outer solar system missions, including: the Apollo missions [4], the Mariner missions to Venus and Mercury [5], the Galileo mission to Jupiter [6], and the Cassini mission to Saturn and its moons [7].

Further work has been done by Battin to derive a Least-Squares solution for nonlinear systems, a weighted Least-Squares solution for systems with measurement noise, and methods to recursively update the optimal estimate [2].

A key factor for Least-Squares solutions is the measurement geometry. The quality of the measurement geometry can be measured using Dilution of Precision (DOP). Traditionally used for GPS systems, DOP provides a metric that can be used to study the measurement geometry of various estimation problems [8]. Consider Fig. 1, depicting two transmitters measuring the distance to an object with measurement error [9]:

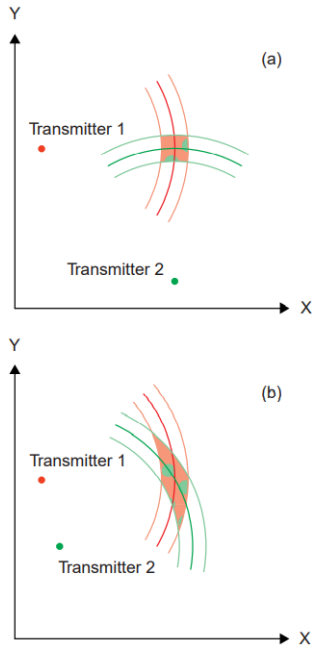

Fig. 2.1: Measurement Geometry

Graph **(a)** depicts two transmitters placed such that the measurements taken are nearly orthogonal to each other, minimizing the error associated with the position estimate. Graph **(b)** depicts Transmitter 2 placed close to Transmitter 1, which does not minimize the error as effectively as the configuration in **(a)**.

Using the Least-Squares solution previously derived, the DOP can be calculated and measurement noise incorporated [8]. The State Error Covariance of a state estimate can be found using the Expectation Operator $E[\cdot]$ [9]:

$$P_{\boldsymbol{x}} = E\left[(\boldsymbol{x} - \hat{\boldsymbol{x}})(\boldsymbol{x} - \hat{\boldsymbol{x}})^T\right] \tag{2.8}$$

The Least-Squares solution is substituted into Eq. 2.8 to obtain:

$$\boldsymbol{z} = H\boldsymbol{x} + \boldsymbol{\nu} \tag{2.9}$$

$$\hat{\boldsymbol{x}} = \left(H^T H\right)^{-1} H^T (H\boldsymbol{x} + \boldsymbol{\nu}) \tag{2.10}$$

$$\hat{\boldsymbol{x}} = \left(H^T H\right)^{-1} H^T H\boldsymbol{x} + \left(H^T H\right)^{-1} H^T \boldsymbol{\nu} \tag{2.11}$$

$$\boldsymbol{x} - \hat{\boldsymbol{x}} = -\left(H^T H\right)^{-1} H^T \boldsymbol{\nu} \tag{2.12}$$

$$P_{\boldsymbol{x}} = E\left[\left(H^T H\right)^{-1} H^T \boldsymbol{\nu}\boldsymbol{\nu}^T H \left(H^T H\right)^{-1}\right] \tag{2.13}$$

Where the expectation of each measurement is equivalent, the expectation of $\boldsymbol{\nu}^T\boldsymbol{\nu}$ is expressed as $\sigma_\nu^2 I$, and the scalar value σ_ν^2 is factored out of the expectation operator:

$$P_{\boldsymbol{x}} = \sigma_\nu^2 E\left[\left(H^T H\right)^{-1} H^T I H \left(H^T H\right)^{-1}\right] \tag{2.14}$$

$$\boxed{P_{\boldsymbol{x}} = \sigma_\nu^2 \left(H^T H\right)^{-1}} \tag{2.15}$$

Thus the State Error Covariance can be expressed in terms of the measurement information and the measurement noise. Position and Velocity Dilution of Precision (PDOP and VDOP respectively), are found by taking the square root of the trace of the respective portion of $\left(H^T H\right)^{-1}$:

$$\text{PDOP} = \sqrt{\text{tr}\left[M_r^T \left(H^T H\right)^{-1} M_r\right]} \tag{2.16}$$

$$\text{VDOP} = \sqrt{\text{tr}\left[M_v^T \left(H^T H\right)^{-1} M_v\right]} \tag{2.17}$$

where M_r and M_v are mapping matrices to analyze solely the position or velocity components of $\left(H^T H\right)^{-1}$.

Note that taking the square root of the trace is the same method by which the Root Sum Square (RSS) of the State Error Covariance is found, thus the relationship exists between the RSS of the State Error Covariance and DOP.

$$\mathrm{RSS}_r(P_{\boldsymbol{x}}) = \sigma_\nu \mathrm{PDOP} \tag{2.18}$$

$$\mathrm{RSS}_v(P_{\boldsymbol{x}}) = \sigma_\nu \mathrm{VDOP} \tag{2.19}$$

DOP values less than one reduce the effects of measurement error, while DOP values greater than one amplify measurement error.

2.1.2 Kalman Filtering and Linear Covariance Analysis

Rudolf E. Kalman published his work for linear filters and prediction theory in 1960; the resulting work is commonly referred to as a Kalman Filter [10]. The Kalman Filter relies on conditional probability to determine the state, conditioned on measurement information.

The Kalman Filter, unlike Batch Least-Squares methods, is an optimal, *recursive* measurement processing algorithm [11]. The Kalman Filter is optimal in the sense that it takes an *a priori* estimate of the state and incorporates all useful information from incoming measurements and formulates an *a posterior* estimate. Measurement information is corrupted by noise, often assumed to be white, Gaussian noise [11,12].

Because the traditional Kalman Filter assumes linear dynamics and nominal space trajectories rely heavily on nonlinear gravitational dynamics, it is often more useful to consider the Linearized Kalman Filter (LKF). The LKF linearizes the dynamics about a nominal state or trajectory to provide a more accurate state estimate for a nonlinear system [12]. Furthermore, the LKF is utilized in Traditional LinCov analysis to determine the expected performance of the LKF by analyzing the State Error Covariance [13].

In addition, the Kalman Filter can take into account nonlinearities by using an Extended Kalman Filter (EKF). The EKF introduces initial perturbations to produce an estimated state that is off-nominal. The EKF propagates the estimated state forward using nonlinear dynamics and incorporates a nonlinear measurement model to converge the estimated state

to the true state. A Monte Carlo analysis implements multiple EKF's to determine a true State Error Covariance that is comparable to the covariance produced by the EKF and in many circumstances comparable to the covariance produced by the LKF in a LinCov. Traditional LinCov has been validated for a variety of missions, including: orbital rendezvous [14], powered descent [15], for the Mars Pathfinder [16], and for cislunar trajectories [17].

2.2 Ground-Based Navigation

Ground-Based Navigation systems have been implemented since the early 1960s [1]. While onboard measurement metrics are powerful, Earth-based observables provide highly accurate state estimates [18]. NASA originally utilized a ground station configuration of three large dishes, known as the Deep Space Network (DSN). As the number of space operations have increased, tracking stations have been built by private companies and universities [19] worldwide.

2.2.1 Measurements

While various measurement types have been developed and used throughout the years, the most common measurement types are range and range-rate measurements [18].

Range measurements are based on the *"time of flight"* principle, in which a signal is transmitted from a ground station, reflected off of the vehicle, and the total time of flight used to calculate the distance. Range-rate, or Doppler, measurements are based on frequency shifts, i.e. Doppler effect [20].

In practice, the equations for calculating range and range-rate measurements based on the time of flight and frequency shift can be burdensome and often are not expressed in terms of the vehicle's state. Instead, ideal measurements are used for navigation filters.

Ideal measurements are based solely on the position and velocity vectors between a ground station and vehicle. The ideal measurements for range and range-rate metrics are provided below [18, 20]:

$$z_r = ||\boldsymbol{r}|| \tag{2.20}$$

$$z_{\dot{r}} = \boldsymbol{i_r}^T \boldsymbol{v} \tag{2.21}$$

The equations above are for 1-way measurements, where the ground station provides a signal to and is processed aboard the vehicle. More commonly used are 2-way measurements, where the signal is reflected off of the vehicle and processed by the ground station. Ideal 2-way range and range-rate measurements are simply twice the value of 1-way measurements. 3-way measurements include the spacecraft and two different ground stations.

The realization of these measurement types are corrupted through various means: measurement noise, measurement biases, atmospheric effects, and relativistic effects. Atmospheric effects are manifested as an additional bias as a function of a station's position relative to the space vehicle with a greater bias occurring when the signal travels through more atmosphere [20].

2.2.2 Ground Station Tracking Schedule

Creating ground station tracking schedules in the early days of space exploration was less complicated due to the limited number of ground stations. However, as space exploration has ventured further and has become more privatized, the number of ground stations has increased and creating tracking schedules has become more complicated. The main factors to consider when creating a ground station tracking schedule are connection quality, estimation performance, and monetary costs [21].

Connection quality describes the station's ability to send data to and from a vehicle in space. Various Earth orbiting missions, including GPS, geosynchronous, and LEO weather satellites, rely heavily on multiple connections with ground stations, and choosing an optimal ground station configuration varies depending on atmospheric effects [22, 23]. For space

missions beyond a geosynchronous orbit, ground station size impacts signal strength and range [24]. Some stations have a smaller Field of View (FOV) or may be surrounded by mountains and thus may not provide as much visibility as other stations.

The ground stations also need to provide some level of estimation performance. Individual stations have measurement noise and biases that impact the measurement information, Furthermore, the location of multiple stations impacts the quality of the state estimation via the measurement geometry. The majority of ground stations are located in the Northern Hemisphere due to available landmass, and navigation experts emphasize the necessity of ground station latitude variety for cislunar space [21]. Some stations may be unable to provide both range and range-rate measurements [24].

Lastly, monetary costs impact any business and must be considered for long-term operations. Implementing a tracking schedule that meets mission requirements while also minimizing operational costs will promote future missions [24].

2.3 Optimization Techniques

Creating a ground station tracking schedule has been done manually following the guidelines of connection quality, estimation performance, and monetary costs for years. Creating an optimal tracking schedule requires an optimization algorithm that determines the values of a set of problem parameters that minimize some objective function. This branch of optimization is known as parameter optimization or as combinatorial optimization, with the most famous example being that of the Traveling Salesman. Parameter optimization is the search for an optimal object among a finite, discrete set of objects [25].

In theory, since the set of objects is discrete and finite, each configuration could be tested and the optimal object chosen. However, doing so is usually infeasible, leading to the necessity of more sophisticated methods. Various parameter optimizations algorithms have been created, including Genetic Algorithms, Simulated Annealing, Tabu Searches, and Slime Molds [26].

Genetic Algorithms are based on the idea of natural selection in biology, where an initial population reproduces with the best children surviving and repopulating [27]. Genetic

Algorithms have been used for a variety of space missions and ground tracking optimization problems, including trajectory planning [28], GPS satellite configuration for optimal station tracking [29], and network optimization for the DSN [30]. Simulated Annealing is a probabilistic optimization algorithm based on the idea of heat treatment in metallurgy. Simulated Annealing is more easily suited for problems with multiple constraints and has been used by NASA for internal satellite constellation communications [31, 32].

CHAPTER 3

MONTE CARLO SIMULATION MODELS

Monte Carlo simulations are used for a variety of space applications, including estimation performance and true state dispersion analysis [13]. By performing a large number of EKF runs, the final true estimation state errors are calculated. Estimation errors generated from a Monte Carlo analysis are the most accurate representation of what the true estimation errors will be in mission flight due to the EKF's ability to propagate the nonlinear dynamics and incorporate nonlinear measurements. This chapter outlines the equations and process to generate true and estimated measurements and how said measurements are implemented in an EKF. The details are described on how a Monte Carlo analysis is used to analyze the state estimation errors through multiple EKF runs.

3.1 Monte Carlo Procedure

The Monte Carlo analysis is depicted below in Fig. 3.1, where the initial true state is perturbed from the initial nominal state by a Gaussian instance $\boldsymbol{\xi}$ of the initial covariance matrix:

$$\boldsymbol{x}_{true} = \boldsymbol{x}_{nom} + \boldsymbol{\xi} \tag{3.1}$$

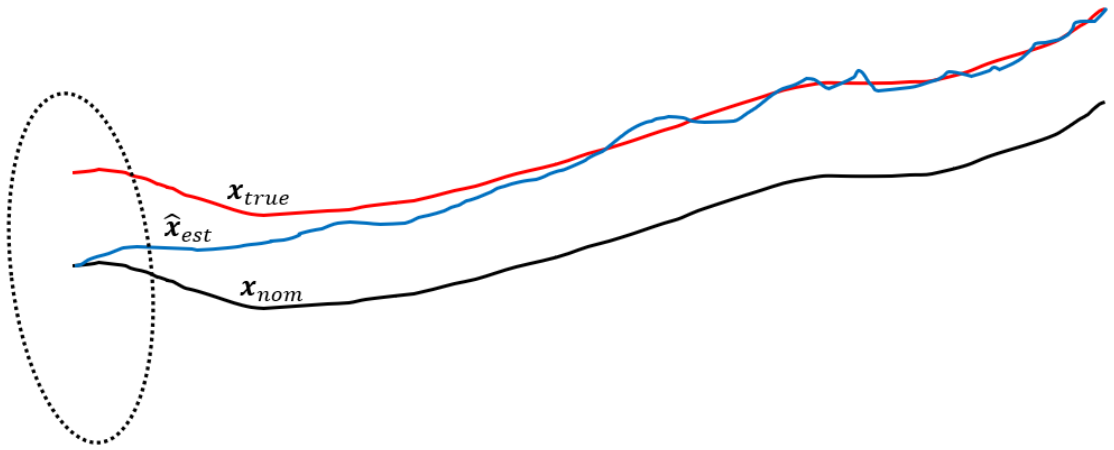

Fig. 3.1: Monte Carlo Analysis

The true state is propagated using the true state dynamics, including random disturbances. The estimated state is initialized at the nominal state and is propagated using the estimated state dynamics, which do not include process noise. Through the use of an EKF, the estimated state is updated and approaches the true state. At each time step, the true estimation errors are calculated as:

$$\boldsymbol{\delta_e} = \boldsymbol{x}_{true} - \hat{\boldsymbol{x}}_{est} \tag{3.2}$$

Once the EKF reaches a set final time, the true estimation errors are stored and the simulation is repeated a large number of times with different random true state initializations. The covariance of the true estimation errors are calculated as:

$$P(t) = \frac{1}{n-1} \sum_{i=1}^{n} \boldsymbol{\delta_e}(t) \boldsymbol{\delta_e}(t)^T \tag{3.3}$$

As the number of simulations are run, the confidence associated with the estimation covariance increases [13]. The following sections outline how the true and estimated states are propagated and updated in an EKF.

3.2 State Vector

The state vector to be analyzed consists of the lander's position and velocity vectors in LCI coordinates. For the Monte Carlo analysis, the true state vector contains the same elements as the estimated state vector. The state vector includes the lander's position and velocity vectors, acceleration due to SRP $\boldsymbol{\psi}$, and station range and range-rate biases:

$$\boldsymbol{x} = \begin{bmatrix} \boldsymbol{r}^{LCI} \\ \boldsymbol{v}^{LCI} \\ \boldsymbol{\psi} \\ \boldsymbol{b}_r \\ \boldsymbol{b}_{\dot{r}} \end{bmatrix} \tag{3.4}$$

where the SRP acceleration is a 3×1 vector, and the station biases are $N \times 1$ vectors corresponding to the number of stations N. The lander's position and velocity vectors are analyzed in the lunar centered inertial frame to facilitate analysis in lunar orbit.

3.3 Measurement Information

For a Monte Carlo analysis, true measurements are generated based on the true state and corrupted by measurement biases and noise:

$$\tilde{\boldsymbol{z}}_k = \boldsymbol{h}(\boldsymbol{x}_k, t) + \boldsymbol{\nu}_k \tag{3.5}$$

Measurements are generated from the ground stations based on a tracking schedule. Figure 3.2 depicts the vectors used to generate the measurements:

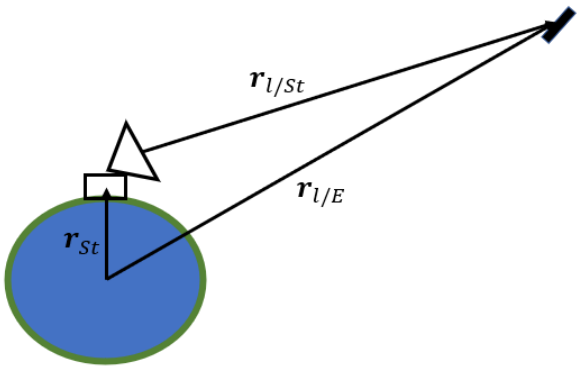

Fig. 3.2: Measurement Generation

True 2-way range measurements are generated according to the lander's true position relative to the station, The station's positions are determined based on their latitude and longitude, ϕ and λ:

$$\boldsymbol{r}_{st}^{ECEF} = R_E \begin{bmatrix} \cos(\phi)\cos(\phi) \\ \cos(\phi)\sin(\phi) \\ \sin(\lambda) \end{bmatrix} \tag{3.6}$$

The station's position vector is then rotated to the inertial frame based on the current Julian Date

$$T_{ECEF\rightarrow ECI} = \begin{bmatrix} \cos(\omega) & \sin(\omega) & 0 \\ -\sin(\omega) & \cos(\omega) & 0 \\ 0 & 0 & 1 \end{bmatrix} \tag{3.7}$$

$$\boldsymbol{r}_{St}^{ECI} = T_{ECFE\rightarrow ECI}\boldsymbol{r}_{St}^{ECEF} \tag{3.8}$$

The relative position of the lander with respect to the station is found as:

$$\boldsymbol{r}_{l/St}^{ECI} = \boldsymbol{r}_{l/E}^{ECI} - \boldsymbol{r}_{St}^{ECI} \tag{3.9}$$

For notational convenience, assume all subsequent vectors used are in the inertial J2000 frame. True range measurements are then calculated with the true bias associated with the correct station and measurement noise.

$$\tilde{z}_r = 2||\boldsymbol{r}_{l/St}|| + b_r + \nu_r \tag{3.10}$$

True 2-way range-rate measurements are generated according to the lander's true position and velocity relative to the station. The relative velocity is calculated

$$\boldsymbol{v}_{l/St} = \boldsymbol{v}_{l/E} - (\boldsymbol{\omega}_E \times \boldsymbol{r}_{St}) \tag{3.11}$$

where the station's velocity is determined from the Earth's rotation. The true range-rate measurements are then calculated with the true range-rate bias associated with the correct station and measurement noise.

$$\tilde{z}_{\dot{r}} = 2\boldsymbol{v}_{l/St}^T\boldsymbol{i}_{\boldsymbol{r}_{l/St}} + b_{\dot{r}} + \nu_{\dot{r}} \tag{3.12}$$

Similarly, the estimated measurements are based on the estimated states without measurement noise:

$$\hat{z}_r = 2||\hat{\boldsymbol{r}}_{l/St}|| + \hat{b}_r \tag{3.13}$$

$$\hat{z}_{\dot{r}} = 2\hat{\boldsymbol{v}}_{l/St}^T \hat{\boldsymbol{i}}_{\boldsymbol{r}_{l/St}} + \hat{b}_{\dot{r}} \tag{3.14}$$

Lastly, the measurement partial matrix is evaluated at the estimated state:

$$H = \frac{\partial \boldsymbol{h}}{\partial \boldsymbol{x}}\Big|_{\hat{\boldsymbol{x}}} \tag{3.15}$$

$$H = \begin{bmatrix} \frac{\partial \boldsymbol{h}_r}{\partial \boldsymbol{r}} & \frac{\partial \boldsymbol{h}_r}{\partial \boldsymbol{v}} & \frac{\partial \boldsymbol{h}_r}{\partial \psi} & \frac{\partial \boldsymbol{h}_r}{\partial b_r} & \frac{\partial \boldsymbol{h}_r}{\partial b_{\dot{r}}} \\ \\ \frac{\partial \boldsymbol{h}_{\dot{r}}}{\partial \boldsymbol{r}} & \frac{\partial \boldsymbol{h}_{\dot{r}}}{\partial \boldsymbol{v}} & \frac{\partial \boldsymbol{h}_{\dot{r}}}{\partial \psi} & \frac{\partial \boldsymbol{h}_{\dot{r}}}{\partial b_r} & \frac{\partial \boldsymbol{h}_{\dot{r}}}{\partial b_{\dot{r}}} \end{bmatrix}\Bigg|_{\hat{\boldsymbol{x}}} \tag{3.16}$$

Filling in the partials:

$$\frac{\partial \boldsymbol{h}_r}{\partial \boldsymbol{r}} = \frac{\partial \boldsymbol{h}_r}{\partial \boldsymbol{r}_{l/St}} \frac{\partial \boldsymbol{r}_{l/St}}{\partial \boldsymbol{r}} = \frac{\partial \boldsymbol{h}_r}{\partial \boldsymbol{r}_{l/St}} \tag{3.17}$$

$$\frac{\partial \boldsymbol{h}_r}{\partial \boldsymbol{r}} = \frac{\partial}{\partial \boldsymbol{r}_{l/St}} \left[2||\boldsymbol{r}_{l/St}|| + b_r + \nu_r\right] \tag{3.18}$$

$$\boxed{\frac{\partial \boldsymbol{h}_r}{\partial \boldsymbol{r}}\Big|_{\hat{\boldsymbol{x}}} = 2\hat{\boldsymbol{i}}_{\boldsymbol{r}_{l/St}}^T} \tag{3.19}$$

The range measurements do not depend on the lander's velocity, and thus the partial $\frac{\partial \boldsymbol{h}_r}{\partial \boldsymbol{v}}$ is 0. Furthermore, the partial $\frac{\partial \boldsymbol{h}_r}{\partial b_r}$ is 1. Proceeding with the range-rate partial with respect to the lander's position:

$$\frac{\partial \boldsymbol{h}_{\dot{r}}}{\partial \boldsymbol{r}} = \frac{\partial \boldsymbol{h}_{\dot{r}}}{\partial \boldsymbol{r}_{l/St}} \frac{\partial \boldsymbol{r}_{l/St}}{\partial \boldsymbol{r}} = \frac{\partial \boldsymbol{h}_{\dot{r}}}{\partial \boldsymbol{r}_{l/St}} \tag{3.20}$$

$$\frac{\partial \boldsymbol{h}_{\dot{r}}}{\partial \boldsymbol{r}} = \frac{\partial}{\partial \boldsymbol{r}_{l/St}} \left[2\boldsymbol{v}_{l/St}^T \boldsymbol{i}_{\boldsymbol{r}_{l/St}} + b_{\dot{r}} + \nu_{\dot{r}}\right] \tag{3.21}$$

$$\boxed{\frac{\partial \boldsymbol{h}_{\dot{r}}}{\partial \boldsymbol{r}}\Big|_{\hat{\boldsymbol{x}}} = \frac{2\hat{\boldsymbol{v}}_{l/St}^T}{||\hat{\boldsymbol{r}}_{l/St}||}(I - \hat{\boldsymbol{i}}_{\boldsymbol{r}_{l/St}} \hat{\boldsymbol{i}}_{\boldsymbol{r}_{l/St}}^T)} \tag{3.22}$$

Proceeding with the range-rate partial with respect to the lander's velocity:

$$\frac{\partial \boldsymbol{h}_{\dot{r}}}{\partial \boldsymbol{v}} = \frac{\partial \boldsymbol{h}_{\dot{r}}}{\partial \boldsymbol{v}_{l/St}} \frac{\partial \boldsymbol{v}_{l/St}}{\partial \boldsymbol{v}} = \frac{\partial \boldsymbol{h}_{\dot{r}}}{\partial \boldsymbol{v}_{l/St}} \tag{3.23}$$

$$\frac{\partial \boldsymbol{h}_{\dot{r}}}{\partial \boldsymbol{v}} = \frac{\partial}{\partial \boldsymbol{v}_{l/St}} \left[2\boldsymbol{v}_{l/St}^T \boldsymbol{i}_{\boldsymbol{r}_{l/St}} + b_{\dot{r}} + \nu_{\dot{r}} \right] \tag{3.24}$$

$$\boxed{\left. \frac{\partial \boldsymbol{h}_{\dot{r}}}{\partial \boldsymbol{v}} \right|_{\hat{\boldsymbol{x}}} = 2\hat{\boldsymbol{i}}_{\boldsymbol{r}_{l/St}}^T} \tag{3.25}$$

Again note that the partial $\frac{\partial \boldsymbol{h}_{\dot{r}}}{\partial b_{\dot{r}}}$ is simply 1. Filling out the H matrix:

$$H = \begin{bmatrix} 2\hat{\boldsymbol{i}}_{\boldsymbol{r}_{l/St}}^T & 0_{1\times 3} & 0_{1\times 3} & 1 & 0 \\ \frac{2\hat{\boldsymbol{v}}_{l/St}^T}{||\hat{\boldsymbol{r}}_{l/St}||}(I - \hat{\boldsymbol{i}}_{\boldsymbol{r}_{l/St}} \hat{\boldsymbol{i}}_{\boldsymbol{r}_{l/St}}^T) & 2\hat{\boldsymbol{i}}_{\boldsymbol{r}_{l/St}}^T & 0_{1\times 3} & 0 & 1 \end{bmatrix} \tag{3.26}$$

Note for compactness the partials with respect to the station biases have been written as scalar 1s and 0s. The complete measurement partial with multiple stations consists of a vector of 0's, with a 1 placed corresponding the correct station. The H matrix above is correct if only one station is being analyzed.

3.4 Extended Kalman Filter

3.4.1 State Differential Equations

For the Monte Carlo analysis, state differential equations are required to propagate both the true and estimated state vectors. The true and estimated state differential equations are expressed using multi-body gravitational dynamics. Figure 3.3 below depicts the multi-body acceleration vectors in an arbitrary inertial frame:

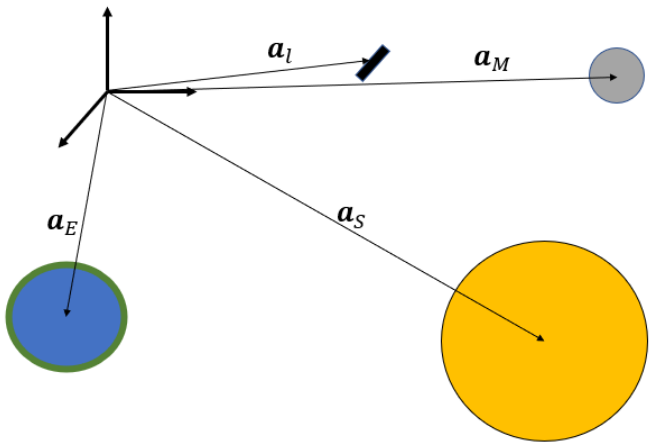

Fig. 3.3: N-Body Gravitational Forces

The acceleration of the lander is calculated from the gravitational acceleration from the Earth, Moon, and Sun:

$$\boldsymbol{a}_{l,E} = -\frac{\mu_E}{||\boldsymbol{r}_{l/E}||^3}\boldsymbol{r}_{l/E} + \sum_{n=0}^{8}\sum_{m=1}^{n}\boldsymbol{a}_{nm,E} \tag{3.27}$$

$$\boldsymbol{a}_{l,M} = -\frac{\mu_M}{||\boldsymbol{r}_{l/M}||^3}\boldsymbol{r}_{l/M} + \sum_{n=0}^{25}\sum_{m=1}^{n}\boldsymbol{a}_{nm,M} \tag{3.28}$$

$$\boldsymbol{a}_{l,S} = -\frac{\mu_S}{||\boldsymbol{r}_{l/S}||^3}\boldsymbol{r}_{l/S} \tag{3.29}$$

Note that the double sums for the Earth and Moon represent higher order, spherical harmonic gravity model accelerations. Spherical harmonic models better simulate the complicated mass structures of the Earth and Moon. The spherical harmonic gravitational potential is expressed as [33]:

$$V(r,\phi,\lambda) = \frac{\mu}{r}\sum_{n=0}^{\infty}\sum_{m=0}^{n}\left(\frac{R}{r}\right)^{n} P_{nm}(\sin(\phi))\left[C_{nm}\cos(m\lambda) + S_{nm}\sin(m\lambda)\right] \tag{3.30}$$

Where ϕ and λ represent the lander's latitude and longitude, respectively, to the central body. P_{nm} represents the Associated Legendre polynomial, and C_{nm} and S_{nm} represent a set of gravity coefficients unique to the Earth and Moon. The acceleration is found by taking the partial derivative of the gravitational potential with respect to r, ϕ, and λ:

$$\boldsymbol{a} = \begin{bmatrix} \frac{\partial V}{\partial r} & \frac{1}{r}\frac{\partial V}{\partial \lambda} & \frac{1}{r\cos(\phi)}\frac{\partial V}{\partial \phi} \end{bmatrix} \tag{3.31}$$

and then rotating the acceleration vector to the inertial frame. For this research, 8×8 and 25×25 gravity models are used for the Earth and Moon, respectively. Note that in Eq. 3.27 and 3.28 the summation begins at $n = 1$, as the acceleration of the $n = 0$ and $m = 0$ term corresponds to the point mass acceleration.

Thus the inertial acceleration of the lander can be expressed as the gravitational acceleration from the Sun, Earth, and Moon:

$$\boldsymbol{a}_l = \boldsymbol{a}_{l,S} + \boldsymbol{a}_{l,E} + \boldsymbol{a}_{l,M} \tag{3.32}$$

To obtain a gravitational acceleration with respect to the Moon, the acceleration of the Moon due to the point masses of the Earth and Sun is found as:

$$\boldsymbol{a}_{M,S} = -\frac{\mu_S}{||\boldsymbol{r}_{M/S}||^3}\boldsymbol{r}_{M/S} \tag{3.33}$$

$$\boldsymbol{a}_{M,E} = -\frac{\mu_E}{||\boldsymbol{r}_{M/E}||^3}\boldsymbol{r}_{M/E} \tag{3.34}$$

$$\boldsymbol{a}_M = \boldsymbol{a}_{M,S} + \boldsymbol{a}_{M,E} \tag{3.35}$$

Note that while the lander's acceleration from the Earth is modeled with higher order gravity terms, the Moon's acceleration from the Earth is not. This is due to the consistently large distance between the two bodies, where the higher order gravity terms are negligible. The lander's acceleration with respect to the Moon is:

$$\boldsymbol{a}_{l/M} = \boldsymbol{a}_l - \boldsymbol{a}_M \tag{3.36}$$

Using the gravitational acceleration, the true state differential equations are expressed as:

$$\dot{\boldsymbol{r}} = \boldsymbol{v} \tag{3.37}$$

$$\dot{\boldsymbol{v}} = \boldsymbol{a}_{l/M} + \boldsymbol{\psi} + \boldsymbol{w}_a \tag{3.38}$$

$$\dot{\boldsymbol{\psi}} = -\frac{\boldsymbol{\psi}}{\tau_\psi} + \boldsymbol{w}_\psi \tag{3.39}$$

$$\dot{\boldsymbol{b}}_r = -\frac{\boldsymbol{b}_r}{\tau_{b_r}} + \boldsymbol{w}_{b_r} \tag{3.40}$$

$$\dot{\boldsymbol{b}}_{\dot{r}} = -\frac{\boldsymbol{b}_{\dot{r}}}{\tau_{b_{\dot{r}}}} + \boldsymbol{w}_{b_{\dot{r}}} \tag{3.41}$$

where the SRP acceleration and station biases are modeled as Exponentially Correlated Random Vectors (ECRVs). Note that the true dynamics are impacted by random disturbances $\boldsymbol{w}$. The true state dynamics are integrated with a fixed step rk4 integrator to hold disturbances constant over integration steps. The estimated state vector differential equations are similar, but do not include random disturbances:

$$\dot{\hat{\boldsymbol{r}}} = \hat{\boldsymbol{v}} \tag{3.42}$$

$$\dot{\hat{\boldsymbol{v}}} = \hat{\boldsymbol{a}}_{l/M} + \hat{\boldsymbol{\psi}} \tag{3.43}$$

$$\dot{\hat{\boldsymbol{\psi}}} = -\frac{\hat{\boldsymbol{\psi}}}{\tau_\psi} \tag{3.44}$$

$$\dot{\hat{\boldsymbol{b}}}_r = -\frac{\hat{\boldsymbol{b}}_r}{\tau_{b_r}} \tag{3.45}$$

$$\dot{\hat{\boldsymbol{b}}}_{\dot{r}} = -\frac{\hat{\boldsymbol{b}}_{\dot{r}}}{\tau_{b_{\dot{r}}}} \tag{3.46}$$

The estimated state differential equations are propagated using MATLAB's ode45 tool.

3.4.2 Filter Covariance Propagation

The filter covariance is initialized based on the same covariance in which the true states are perturbed. The filter covariance is propagated using the gravitational dynamics and the random process noise. First, the Jacobian is calculated and analyzed at the estimated state:

$$\dot{\hat{\boldsymbol{x}}} = \boldsymbol{f}(\hat{\boldsymbol{x}}, t) \tag{3.47}$$

$$F = \left.\frac{\partial \boldsymbol{f}}{\partial \boldsymbol{x}}\right|_{\hat{\boldsymbol{x}}} \tag{3.48}$$

Expanding the elements of the Jacobian

$$F = \left.\begin{bmatrix} \frac{\partial \dot{\boldsymbol{r}}}{\partial \boldsymbol{r}} & \frac{\partial \dot{\boldsymbol{r}}}{\partial \boldsymbol{v}} & \frac{\partial \dot{\boldsymbol{r}}}{\partial \boldsymbol{\psi}} & \frac{\partial \dot{\boldsymbol{r}}}{\partial \boldsymbol{b}_r} & \frac{\partial \dot{\boldsymbol{r}}}{\partial \boldsymbol{b}_{\dot{r}}} \\ \frac{\partial \dot{\boldsymbol{v}}}{\partial \boldsymbol{r}} & \frac{\partial \dot{\boldsymbol{v}}}{\partial \boldsymbol{v}} & \frac{\partial \dot{\boldsymbol{v}}}{\partial \boldsymbol{\psi}} & \frac{\partial \dot{\boldsymbol{v}}}{\partial \boldsymbol{b}_r} & \frac{\partial \dot{\boldsymbol{v}}}{\partial \boldsymbol{b}_{\dot{r}}} \\ \frac{\partial \dot{\boldsymbol{\psi}}}{\partial \boldsymbol{r}} & \frac{\partial \dot{\boldsymbol{\psi}}}{\partial \boldsymbol{v}} & \frac{\partial \dot{\boldsymbol{\psi}}}{\partial \boldsymbol{\psi}} & \frac{\partial \dot{\boldsymbol{\psi}}}{\partial \boldsymbol{b}_r} & \frac{\partial \dot{\boldsymbol{\psi}}}{\partial \boldsymbol{b}_{\dot{r}}} \\ \frac{\partial \dot{\boldsymbol{b}}_r}{\partial \boldsymbol{r}} & \frac{\partial \dot{\boldsymbol{b}}_r}{\partial \boldsymbol{v}} & \frac{\partial \dot{\boldsymbol{b}}_r}{\partial \boldsymbol{\psi}} & \frac{\partial \dot{\boldsymbol{b}}_r}{\partial \boldsymbol{b}_r} & \frac{\partial \dot{\boldsymbol{b}}_r}{\partial \boldsymbol{b}_{\dot{r}}} \\ \frac{\partial \dot{\boldsymbol{b}}_{\dot{r}}}{\partial \boldsymbol{r}} & \frac{\partial \dot{\boldsymbol{b}}_{\dot{r}}}{\partial \boldsymbol{v}} & \frac{\partial \dot{\boldsymbol{b}}_{\dot{r}}}{\partial \boldsymbol{\psi}} & \frac{\partial \dot{\boldsymbol{b}}_{\dot{r}}}{\partial \boldsymbol{b}_r} & \frac{\partial \dot{\boldsymbol{b}}_{\dot{r}}}{\partial \boldsymbol{b}_{\dot{r}}} \end{bmatrix}\right|_{\hat{\boldsymbol{x}}} \tag{3.49}$$

Most of these partial derivatives are simple:

$$F = \left.\begin{bmatrix} 0_{3\times3} & I_{3\times3} & 0_{3\times3} & 0_{N\times3} & 0_{N\times3} \\ \frac{\partial \dot{\boldsymbol{v}}}{\partial \boldsymbol{r}} & 0_{3\times3} & I_{3\times3} & 0_{N\times3} & 0_{N\times3} \\ 0_{3\times3} & 0_{3\times3} & -\frac{1}{\tau_\psi} I_{3\times3} & 0_{N\times3} & 0_{N\times3} \\ 0_{3\times N} & 0_{3\times N} & 0_{3\times3} & -\frac{1}{\tau_{b_r}} I_{N\times N} & 0_{N\times N} \\ 0_{3\times N} & 0_{3\times N} & 0_{3\times3} & 0_{N\times N} & -\frac{1}{\tau_{b_{\dot{r}}}} I_{N\times N} \end{bmatrix}\right|_{\hat{\boldsymbol{x}}} \tag{3.50}$$

The more difficult partial is $\frac{\partial \dot{\boldsymbol{v}}}{\partial \boldsymbol{r}}$, often called the gravity gradient. With a point mass gravity model, the gravity gradient from just the Sun is calculated as:

$$\frac{\partial \dot{\boldsymbol{v}}}{\partial \boldsymbol{r}} = \frac{\partial \boldsymbol{a}_l^S}{\partial \boldsymbol{r}_{l/M}} = \frac{\partial \boldsymbol{a}_l^S}{\partial \boldsymbol{r}_{l/S}} \frac{\partial \boldsymbol{r}_{l/S}}{\partial \boldsymbol{r}_{l/M}} \tag{3.51}$$

$$\frac{\partial \boldsymbol{r}_{l/S}}{\partial \boldsymbol{r}_{l/M}} = \frac{\partial}{\partial \boldsymbol{r}_{l/M}} \left[\boldsymbol{r}_{l/M} + \boldsymbol{r}_{M/S}\right] = I \tag{3.52}$$

$$\frac{\partial \dot{\boldsymbol{v}}}{\partial \boldsymbol{r}} = \frac{\partial}{\partial \boldsymbol{r}_{l/S}} \left[\frac{-\mu_S}{||\boldsymbol{r}_{l/S}||^3} \boldsymbol{r}_{l/S}\right] I \tag{3.53}$$

$$\boxed{\left.\frac{\partial \dot{\boldsymbol{v}}}{\partial \boldsymbol{r}}\right|_{\hat{\boldsymbol{x}}} = -\frac{\mu_S}{||\hat{\boldsymbol{r}}_{l/S}||^3} \left[I - \hat{\boldsymbol{i}}_{\boldsymbol{r}_{l/S}} \hat{\boldsymbol{i}}_{\boldsymbol{r}_{l/S}}^T\right]} \tag{3.54}$$

Thus, if the Sun, Earth, and Moon were all treated as point masses, the complete gravity gradient would be:

$$\left.\frac{\partial \dot{\boldsymbol{v}}}{\partial \boldsymbol{r}}\right|_{\hat{\boldsymbol{x}}} = -\frac{\mu_S}{||\hat{\boldsymbol{r}}_{l/S}||^3} \left[I - \hat{\boldsymbol{i}}_{\boldsymbol{r}_{l/S}} \hat{\boldsymbol{i}}_{\boldsymbol{r}_{l/S}}^T\right] - \frac{\mu_E}{||\hat{\boldsymbol{r}}_{l/E}||^3} \left[I - \hat{\boldsymbol{i}}_{\boldsymbol{r}_{l/E}} \hat{\boldsymbol{i}}_{\boldsymbol{r}_{l/E}}^T\right] - \frac{\mu_M}{||\hat{\boldsymbol{r}}_{l/M}||^3} \left[I - \hat{\boldsymbol{i}}_{\boldsymbol{r}_{l/M}} \hat{\boldsymbol{i}}_{\boldsymbol{r}_{l/M}}^T\right] \tag{3.55}$$

The point mass partials are the most dominant terms in the gravity gradient. Calculating the gravity gradient when the Earth and Moon are not treated as point masses is more complicated. The complete gravity gradient according to spherical harmonic models has been derived by Carlos Roithmayr, according to the equation below [33]:

$$\frac{\partial \dot{\boldsymbol{v}}}{\partial \boldsymbol{r}} = -\frac{\mu}{||\boldsymbol{r}||^3} \left[I - \boldsymbol{i}_{\boldsymbol{r}} \boldsymbol{i}_{\boldsymbol{r}}{}^T\right] + \sum_{n=1}^{\infty} \sum_{m=0}^{n} D_{nm} \tag{3.56}$$

where D_{nm} is calculated using second-order tensors, or Dyadics. For more information on how the Dyadics are calculated, see the article *Contributions of Spherical Harmonics to Graviational Moment* [33]. These higher order gravity gradients are found in a fixed frame, and are rotated to the inertial frame according to:

$$D_{nm}^I = T_{I \to F}^T D_{nm}^F T_{I \to F} \tag{3.57}$$

As presented above, the rotation matrix for the Earth is simply a function of the Julian Date. The rotation matrix for the Moon is more complex, and is obtained via a spice function *cspice_pxform* with the kernel *moon_pa_de421_1900-2050.bpc* [34].

Once the gravity gradient is found, the complete Jacobian can be used to calculate the State Transition Matrix (STM) according to Lear's method [35], which up to the second order is accurate for time-varying systems:

$$\Delta t = t_{k+1} - t_k \tag{3.58}$$

$$\Phi_{k+1,k} \approx I + (F_k + F_{k+1})\frac{\Delta t}{2} + F_k F_{k+1}\frac{(\Delta t)^2}{2} \tag{3.59}$$

With the STMs, the filter covariance can be propagated according to:

$$P_{k+1}^{-} = \Phi_{k+1,k} P_k^{-} \Phi_{k+1,k}^T + B Q_{d,k} B^T \tag{3.60}$$

Where $Q_{d,k}$ represents the strength of the discrete process noise. The strength of continuous process noise is found according to:

$$E[\boldsymbol{w}(t)\boldsymbol{w}^T(t-t')] = Q(t)\delta(t-t') \tag{3.61}$$

Where $\delta(t-t')$ is the dirac delta function. The strength of the discrete process noise is found as:

$$Q_{d,k} = Q(t_k)\Delta t \tag{3.62}$$

The discrete process noise strength for the ECRVs are found by analyzing the steady-state (ss) behavior of the system. Analyzing the propagation in Eq. 3.60 for steady state behavior:

$$P_{ss} = \Phi_{k+1,k} P_{ss} \Phi_{k+1,k}^T + Q_{d,ss} \tag{3.63}$$

$$\boxed{Q_{d,ss} = P_{ss}\left(1 - e^{\frac{-2\Delta t}{\tau}}\right)} \tag{3.64}$$

Thus the process noise at each time step is calculated given the covariance of the desired steady-state response. The complete matrix of the discrete process noise strength, including random disturbances, SRP noise, and station bias noise, is expressed as:

$$Q_d = \begin{bmatrix} Q_{d,a} & 0 & 0 & 0 \\ 0 & Q_{d,ss,\psi} & 0 & 0 \\ 0 & 0 & Q_{d,ss,b_r} & 0 \\ 0 & 0 & 0 & Q_{d,ss,b_{\dot{r}}} \end{bmatrix} \tag{3.65}$$

where the sizes of each Q matrix corresponds to the number of states impacted. $Q_{d,a}$ and $Q_{d,ss,\psi}$ are 3×3 matrices relating to the three dimensional acceleration and SRP vectors. Q_{d,ss,b_r} and $Q_{d,ss,b_{\dot{r}}}$ are $N \times N$ matrices corresponding to the number of stations in the analysis.

The true state, estimated state, and the filter covariance are propagated until a measurement becomes available to update the estimated state and filter covariance.

3.4.3 Filter Covariance and State Updates

Once a measurement becomes available, the measurement partials and filter covariance are used to calculate the Kalman gain:

$$K_{k+1} = P_{k+1}^{-} H_{k+1}^{T} (H_{k+1} P_{k+1}^{-} H_{k+1}^{T} + R)^{-1} \tag{3.66}$$

where R is the strength of the measurement noise according to:

$$R_{k+1} = E[\boldsymbol{\nu}_{k+1} \boldsymbol{\nu}_{k+1}^{T}] \tag{3.67}$$

The Kalman gain is used to update the estimated state and the filer covariance:

$$\hat{\boldsymbol{x}}_{k+1}^{+} = \hat{\boldsymbol{x}}_{k+1}^{-} + K_{k+1}(\tilde{\boldsymbol{z}} - \hat{\boldsymbol{z}}) \tag{3.68}$$

$$P_{k+1}^{+} = (I - K_{k+1} H_{k+1}) P_{k+1}^{-} (I - K_{k+1} H_{k+1})^{T} + K_{k+1} R_{k+1} K_{k+1}^{T} \tag{3.69}$$

The updated filter covariance at time t_{k+1} is set to be the new filter covariance at time t_k and the algorithm continues, propagating and incorporating measurements.

3.5 Monte Carlo Performance

While Monte Carlo analysis is a reliable method to quantify state estimation errors, it is also a time consuming process. The EKF is developed in MATLAB and converted to a *mex* function, which allows MATLAB to run the function in C [36]. Furthermore, each EKF is run inside a *parfor* loop, allowing multiple EKF runs to be executed at the same time. While both of these measures greatly decrease the runtime, a Monte Carlo analysis with 1,000 runs can take up to 15 minutes to complete. Due to the large runtime, alternative methods are studied to obtain the estimation errors.

CHAPTER 4
LINEAR COVARIANCE ANALYSIS

Linear Covariance is an alternative to a Monte Carlo analysis that runs far more quickly. By linearizing the dynamics and measurements about the nominal trajectory, a Linearized Kalman Filter (LKF) can be analyzed without any measurement incorporation. As long as the error analysis remains within a region appropriate for linearization, LinCov should produce the same estimation errors as a Monte Carlo analysis. This chapter outlines the equations and procedures to create a traditional LinCov tool to propagate and update a state estimation covariance.

4.1 Linearized Kalman Filter

4.1.1 State Vector

In order to match the Monte Carlo analysis, the state vector for the LinCov analysis is the same, consisting of the lander's position and velocity vectors in LCI coordinates, acceleration due to SRP, and station range and range-rate biases:

$$\boldsymbol{x} = \begin{bmatrix} \boldsymbol{r}^{LCI} \\ \boldsymbol{v}^{LCI} \\ \boldsymbol{\psi} \\ \boldsymbol{b}_r \\ \boldsymbol{b}_{\dot{r}} \end{bmatrix} \tag{4.1}$$

4.1.2 Dynamic Linearization and Covariance Propagation

The nonlinear dynamics are written in compact form as a function of time and the nominal trajectory:

$$\dot{\boldsymbol{x}} = \boldsymbol{f}(\boldsymbol{x}, t) + B\boldsymbol{w} \tag{4.2}$$

where $\boldsymbol{w}$ is a zero-mean Gaussian process noise. With strength according to:

$$E[\boldsymbol{w}(t)\boldsymbol{w}^T(t-t')] = Q(t)\delta(t-t') \tag{4.3}$$

$$Q_{d,k} = Q(t_k)\Delta t \tag{4.4}$$

As with the Monte Carlo analysis, the discrete process noise matrix consists of individual noise strengths corresponding to random accelerations and steady state strengths corresponding to the SRP and bias ECRVs. The dynamics are linearized about the nominal trajectory according to:

$$F = \left.\frac{\partial \boldsymbol{f}}{\partial \boldsymbol{x}}\right|_{\boldsymbol{x}_{nom}} \tag{4.5}$$

$$F = \left.\begin{bmatrix} 0_{3\times3} & I_{3\times3} & 0_{3\times3} & 0_{N\times3} & 0_{N\times3} \\ \left.\frac{\partial \dot{\boldsymbol{v}}}{\partial \boldsymbol{r}}\right|_{\boldsymbol{x}_{nom}} & 0_{3\times3} & I_{3\times3} & 0_{N\times3} & 0_{N\times3} \\ 0_{3\times3} & 0_{3\times3} & -\frac{1}{\tau_\psi} I_{3\times3} & 0_{N\times3} & 0_{N\times3} \\ 0_{3\times N} & 0_{3\times N} & 0_{3\times3} & -\frac{1}{\tau_{b_r}} I_{N\times N} & 0_{N\times N} \\ 0_{3\times N} & 0_{3\times N} & 0_{3\times3} & 0_{N\times N} & -\frac{1}{\tau_{b_{\dot{r}}}} I_{N\times N} \end{bmatrix}\right|_{\boldsymbol{x}_{nom}} \tag{4.6}$$

Note that the Jacobian is analyzed at the nominal state, unlike the EKF where the Jacobian is analyzed at the estimated state. The gravity gradient is calculated along the nominal trajectory using the point mass gravity from the Sun, Earth, and Moon. The higher order gravity gradients are again calculated with Dyadics [33]:

$$\begin{aligned}\left.\frac{\partial \dot{\boldsymbol{v}}}{\partial \boldsymbol{r}}\right|_{\boldsymbol{x}_{nom}} = &-\frac{\mu_S}{||\boldsymbol{r}_{l/S}||^3}\left[I - \boldsymbol{i}_{\boldsymbol{r}_{l/S}}\boldsymbol{i}_{\boldsymbol{r}_{l/S}}^T\right] - \frac{\mu_E}{||\boldsymbol{r}_{l/E}||^3}\left[I - \boldsymbol{i}_{\boldsymbol{r}_{l/E}}\boldsymbol{i}_{\boldsymbol{r}_{l/E}}^T\right] + \sum_{n=1}^{8}\sum_{m=0}^{n} D_{nm,E} \\ &- \frac{\mu_M}{||\boldsymbol{r}_{l/M}||^3}\left[I - \boldsymbol{i}_{\boldsymbol{r}_{l/M}}\boldsymbol{i}_{\boldsymbol{r}_{l/M}}^T\right]\sum_{n=1}^{25}\sum_{m=0}^{n} D_{nm,M}\end{aligned} \tag{4.7}$$

Note that the degree and order of the gravity models are the same as the Monte Carlo analysis. Calculating the STM using Lear's method [35]:

$$\Delta t = t_{k+1} - t_k \tag{4.8}$$

$$\Phi_{k+1,k} = I + (F_k + F_{k+1})\frac{\Delta t}{2} + F_k F_{k+1}\frac{(\Delta t)^2}{2} \tag{4.9}$$

The linearized state and covariance are propagated according to:

$$\delta \boldsymbol{x}_{k+1} = \Phi_{k+1,k}\delta \boldsymbol{x}_k + B\boldsymbol{w}_{d,k} \tag{4.10}$$

$$P_{k+1}^{-} = \Phi_{k+1,k} P_k \Phi_{k+1,k}^T + BQ_{d,k}B^T \tag{4.11}$$

As LinCov is implemented to study the covariance of the state estimation errors, the linearized state propagation in Eq. 4.10 does not need to be incorporated.

4.1.3 Linearized Measurements and Covariance Update

The general measurement equation is written as a function of time, the nominal trajectory, and measurement noise:

$$\boldsymbol{z}_k = \boldsymbol{h}(\boldsymbol{x}_k, t) + \boldsymbol{\nu}_k \tag{4.12}$$

The measurement partial matrix H is found by linearizing about the nominal state:

$$H = \frac{\partial \boldsymbol{h}}{\partial \boldsymbol{x}}\Big|_{\boldsymbol{x}_{nom}} \tag{4.13}$$

$$H = \begin{bmatrix} 2\boldsymbol{i}_{\boldsymbol{r}_{l/St}}^T & 0_{1\times3} & 0_{1\times3} & 1 & 0 \\ \frac{2\boldsymbol{v}_{l/St}^T}{||\boldsymbol{r}_{l/St}||}(I - \boldsymbol{i}_{\boldsymbol{r}_{l/St}}\boldsymbol{i}_{\boldsymbol{r}_{l/St}}^T) & 2\boldsymbol{i}_{\boldsymbol{r}_{l/St}}^T & 0_{1\times3} & 0 & 1 \end{bmatrix}\Bigg|_{\boldsymbol{x}_{nom}} \tag{4.14}$$

The Kalman gain is calculated and implemented to update the covariance matrix:

$$K_{k+1} = P_{k+1}^- H_{k+1}^T (H_{k+1} P_{k+1}^- H_{k+1}^T + R)^{-1} \tag{4.15}$$

$$P_{k+1}^+ = (I - K_{k+1}H_{k+1})P_{k+1}^-(I - K_{k+1}H_{k+1})^T + K_{k+1}RK_{k+1}^T \tag{4.16}$$

4.2 Linear Covariance Performance

Note how LinCov propagates and updates the state estimation covariance without ever generating true or estimated measurements. Furthermore, significant time is saved in LinCov by not propagating the state through numerical integration. As the nominal trajectory is provided by Intuitive Machines, all measurement partials, Jacobians, and State Transition matrices can be precomputed and passed into a LinCov function. When the system dynamics are within a region of linearization, the LinCov state estimation errors will match the results of the Monte Carlo analysis. This is done however, in a vastly faster time. On average, LinCov processes a 24-hour trajectory segment in less than one second.

CHAPTER 5

LINEAR COVARIANCE VALIDATION WITH MONTE CARLO ANALYSIS

Before a LinCov analysis is implemented, it is proper to verify that the linearization remains valid. This is done by performing a LinCov analysis on each segment of the nominal trajectory and comparing the state estimation to a Monte Carlo analysis. This chapter outlines the nominal trajectory and the key segments to be analyzed by a LinCov and Monte Carlo study. Results are presented demonstrating the validity of LinCov in both cislunar space and in lunar orbit.

5.1 Reference Trajectory, OD Segments, Contact Schedule

The IM-1 reference trajectory and maneuvers in the J2000, Earth-Centered Inertial (ECI) coordinates are shown in Fig. 5.1. The nominal trajectory is generated by NASA's Copernicus software with midcourse correction maneuvers planned by Intuitive Machines.

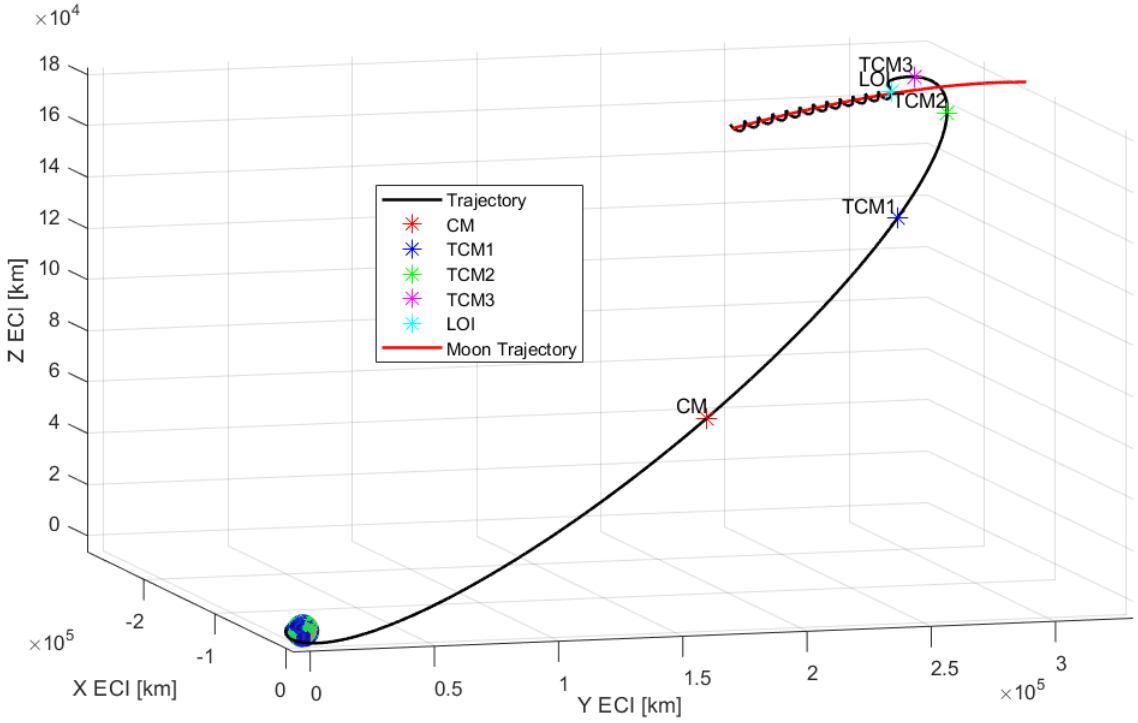

Fig. 5.1: IM-1 Nominal Trajectory

The trajectory shown in Fig. 5.1 begins as the Nova-C lander separates from SpaceX's launch vehicle, referred to as Launch Vehicle Separation (LVS). The trajectory is then divided using midcourse corrections. These midcourse corrections consist of a larger Commissioning Maneuver (CM) and three smaller Trajectory Correction Maneuvers (TCMs). The Nova-C lander is inserted into lunar orbit with a Lunar Orbit Insertion maneuver (LOI). After several lunar orbits, the Nova-C lander begins a Descent Orbit Insertion maneuver (DOI) and descends to the lunar surface.

In addition to correcting Nova-C's trajectory, the maneuvers are utilized to separate the trajectory into subsections for state estimation analysis, referred to as Orbit Determination (OD) segments. Each OD segment is analyzed separately to determine estimation errors in preparation for an upcoming maneuver. From LOI to DOI, the OD segment is broken up into twelve OD subsegments to provide a state estimation solution every orbit, where each orbit takes approximately two hours.

The tracking schedule used for this subsequent analyses is provided by Intuitive Machines, referred to as the Benchmark Schedule. The schedule alternates between 6 available stations: Hartebeesthoek, South Africa (HBK26); Kourou, French Guiana (KRU1); Byalulu, India (D32); Okinwawa, Japan (OKN2); Morehead, Kentucky (DSS17); Goonhilly, England (GHY6). The tracking schedule, depicted when a station is used for measurement generation, is depicted in Fig. 5.2 below:

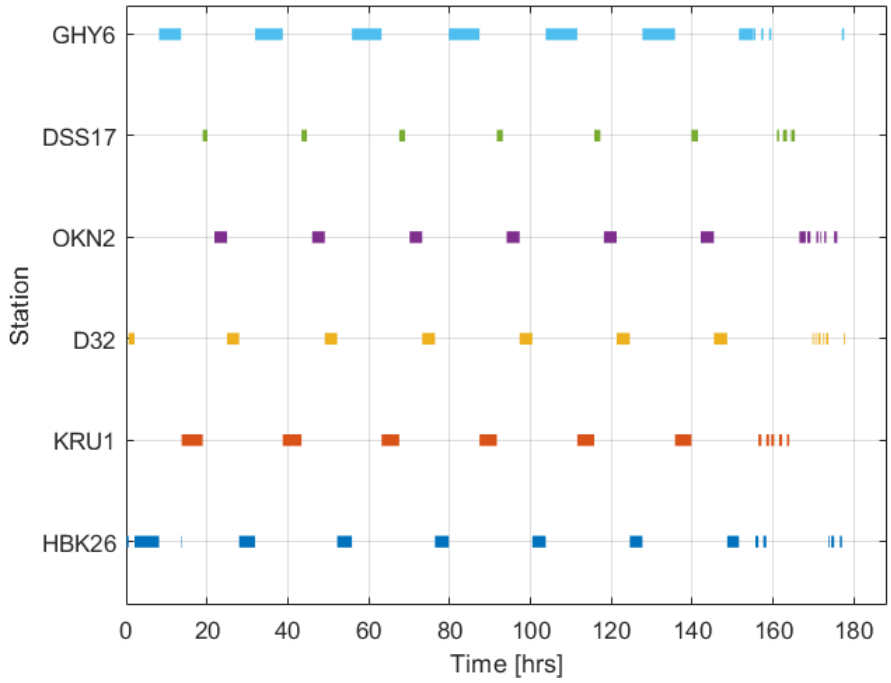

Fig. 5.2: Benchmark Schedule

5.2 Cislunar Simulation Setup

The simulation parameters used in both the LinCov and Monte Carlo analysis for the cislunar environment are recorded below in Table 5.1

Table 5.1: Simulation Setup Values

Parameter	Symbol	Value	Units
Initial Position Error	$\sigma_{r,0}$	10	km
Initial Velocity Error	$\sigma_{v,0}$	1	m/s
Range Measurement Noise	σ_r	100	m
Range-rate Measurement Noise	$\sigma_{\dot{r}}$	1	m/s
Range Bias Steady State	σ_{b_r}	100	m
Range-rate Steady State	$\sigma_{b_{\dot{r}}}$	1	m/s
Range Bias Time Constant	τ_{b_r}	$1e^9$	s
Range-rate Bias Time Constant	τ_{b_r}	$1e^9$	s
SRP Steady State	σ_{ψ}	$8e^{-9}$	m/s^2
SRP Time Constant	τ_{ψ}	$1e^9$	s
Continuous Process Noise Strength	Q	$1e^{-12}$	m^2/s^3

Note that the time constants on the station biases and SRP are large. Both the station biases and acceleration due to SRP act more as biases than noise processes. By making the time constants large, the ECRV's are simulated as nearly constant values. The continuous process noise Q for the IM-1 mission is primarily due to unmodeled

translational accelerations from misaligned attitude thrusters. Realistically this value is not expected to exceed $1e^{-14}\frac{m^2}{s^3}$, but is set as a larger value for conservative estimates in the linearization. Furthermore, the noise and bias values for measurement generation are considered conservative for ground station measurement generation. Note that each of the six stations has the same standard deviations for measurement noise values, range biases, and range-rate biases.

5.3 Cislunar Results

The true inertial navigation errors for the lander's position and velocity from 1,000 Monte Carlo runs are shown below in Table 5.2:

Table 5.2: Monte Carlo Simulation Errors

OD Segment	LVS -CM	CM -TCM1	TCM1 -TCM2	TCM2 -TCM3	TCM3 -LOI
Inertial Errors:					
σ_{r_x} [m]	73.491	94.929	88.803	147.169	15.812
σ_{r_y} [m]	238.307	145.529	124.623	577.107	41.454
σ_{r_z} [m]	379.491	735.208	982.327	3,109.181	44.093
σ_{v_x} [mm/s]	0.393	0.262	0.319	2.323	1.379
σ_{v_y} [mm/s]	2.519	1.784	1.180	10.667	10.797
σ_{v_z} [mm/s]	2.893	1.996	1.899	15.052	14.359

The true inertial navigation errors from the LinCov are shown below in Table 5.3.

Table 5.3: Linear Covariance Errors

OD Segment	LVS -CM	CM -TCM1	TCM1 -TCM2	TCM2 -TCM3	TCM3 -LOI
Inertial Errors:					
σ_{r_x} [m]	73.122	94.562	90.729	142.168	15.762
σ_{r_y} [m]	242.791	149.562	126.877	582.069	40.971
σ_{r_z} [m]	377.108	730.010	1,011.906	2,911.497	45.288
σ_{v_x} [mm/s]	0.381	0.266	0.318	2.338	1.368
σ_{v_y} [mm/s]	2.552	1.786	1.179	10.662	10.683
σ_{v_z} [mm/s]	2.809	1.988	1.883	14.864	14.388

Note how the greatest difference between the inertial navigation errors found by the Monte Carlo analysis and LinCov is 3.56%.

Figure 5.3 below depicts the individual true position navigation errors from the Monte Carlo analysis, the respective 3σ standard deviations from the Monte Carlo data, and the 3σ standard deviations from the LinCov analysis. The OD segment depicted is CM-TCM1. Note how the standard deviations from the LinCov analysis match the Monte Carlo deviations throughout.

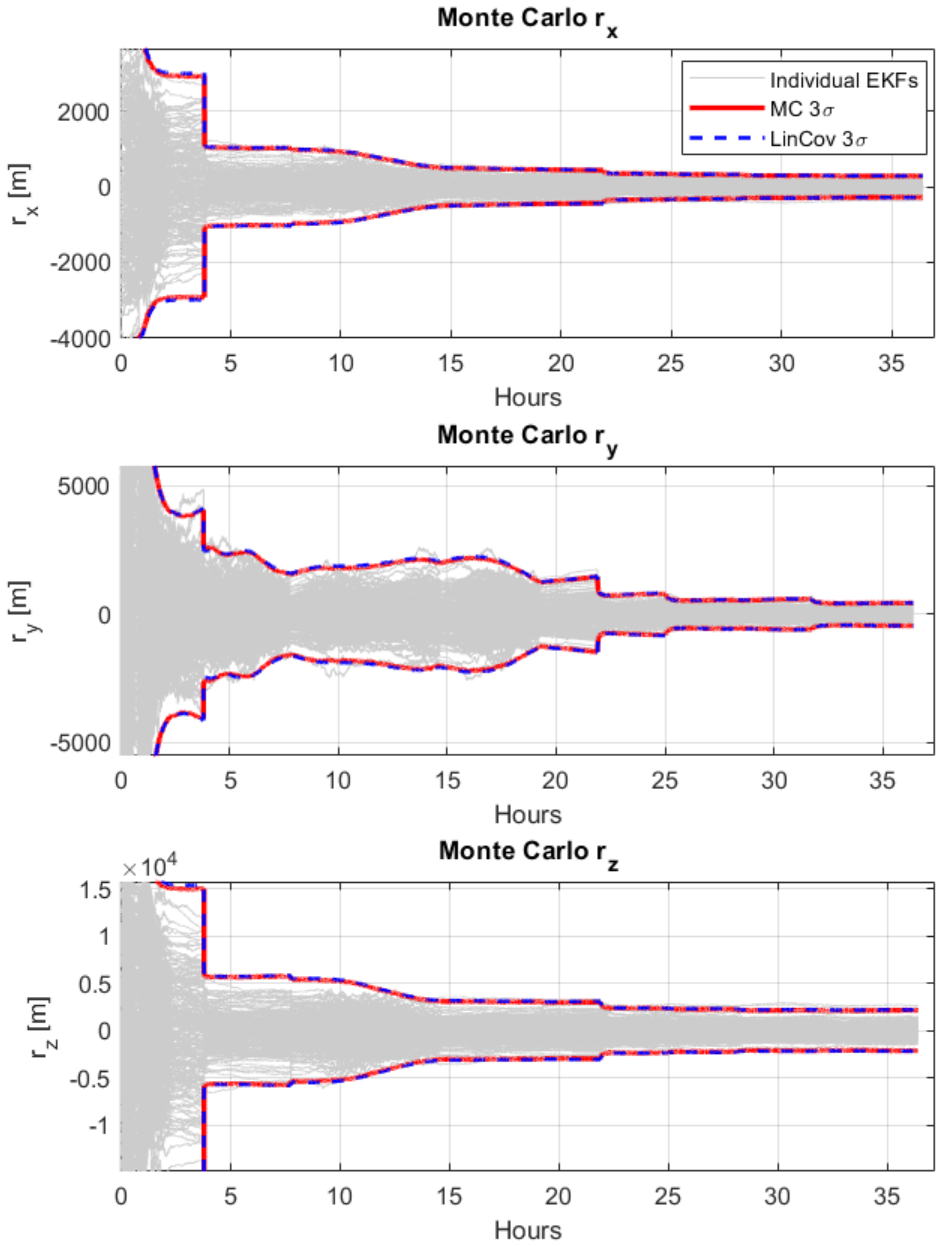

Fig. 5.3: Inertial Position Errors: CM-TCM1

Figure 5.4 below depicts the individual true velocity navigation errors from the Monte Carlo analysis, the respective 3σ standard deviations from the Monte Carlo data and LinCov analysis. Note how the standard deviations from the LinCov analysis match the Monte Carlo deviations throughout.

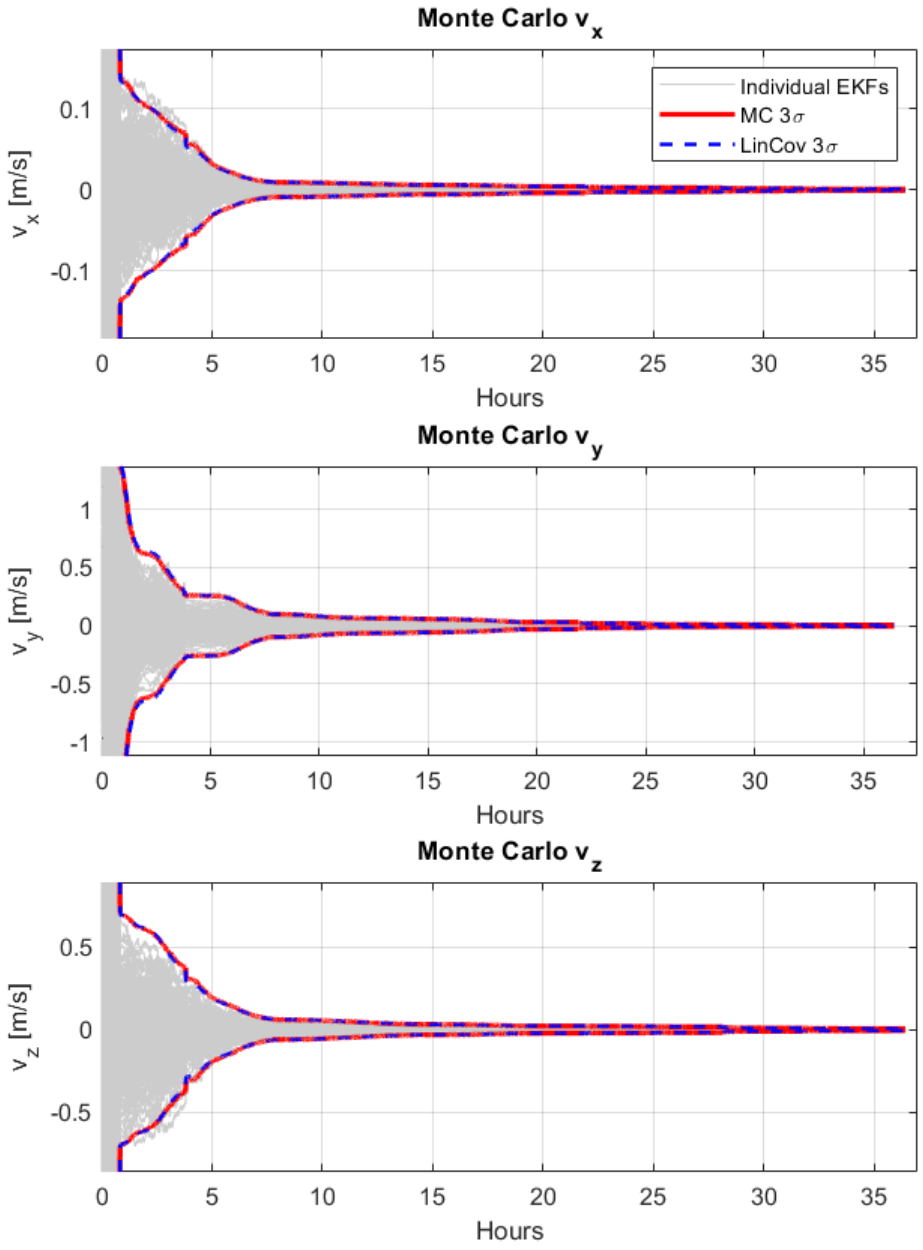

Fig. 5.4: Inertial Velocity Errors: CM-TCM1

Figure 5.5 depicts the inertial navigatoin errors from SRP in the y direction. Note how little estimation occurs, as the SRP is too small to estimate given the process noise from the misaligned thrusters.

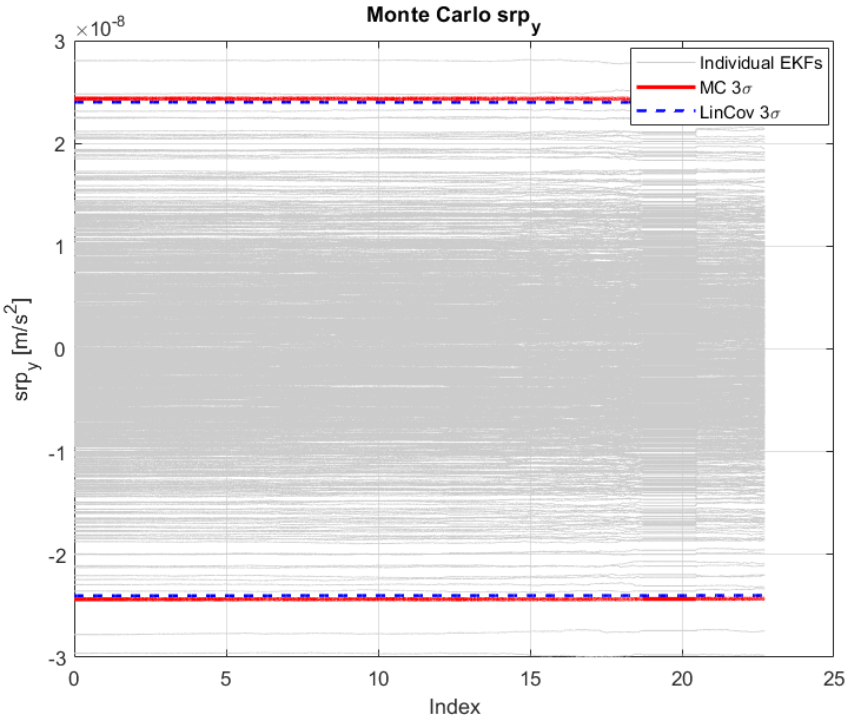

Fig. 5.5: SRP_y Inertial Errors: TLI-CM

Figures 5.6 and 5.7 on the following pages depict the six station bias errors from the Monte Carlo analysis, the respective 3σ standard deviations from the Monte Carlo data, and the 3σ standard deviations from the LinCov analysis. Note how the LinCov errors match the Monte Carlo results well throughout the entire OD segment.

The nature of the station biases is such that information is gathered as the station begins processing measurements, decreasing the errors. What is often more powerful in reducing a station's bias estimation errors is data from subsequent stations. As the correlations between stations is determined through measurement updates, errors decrease. When no measurements are being incorporated, the errors increase toward the steady state error.

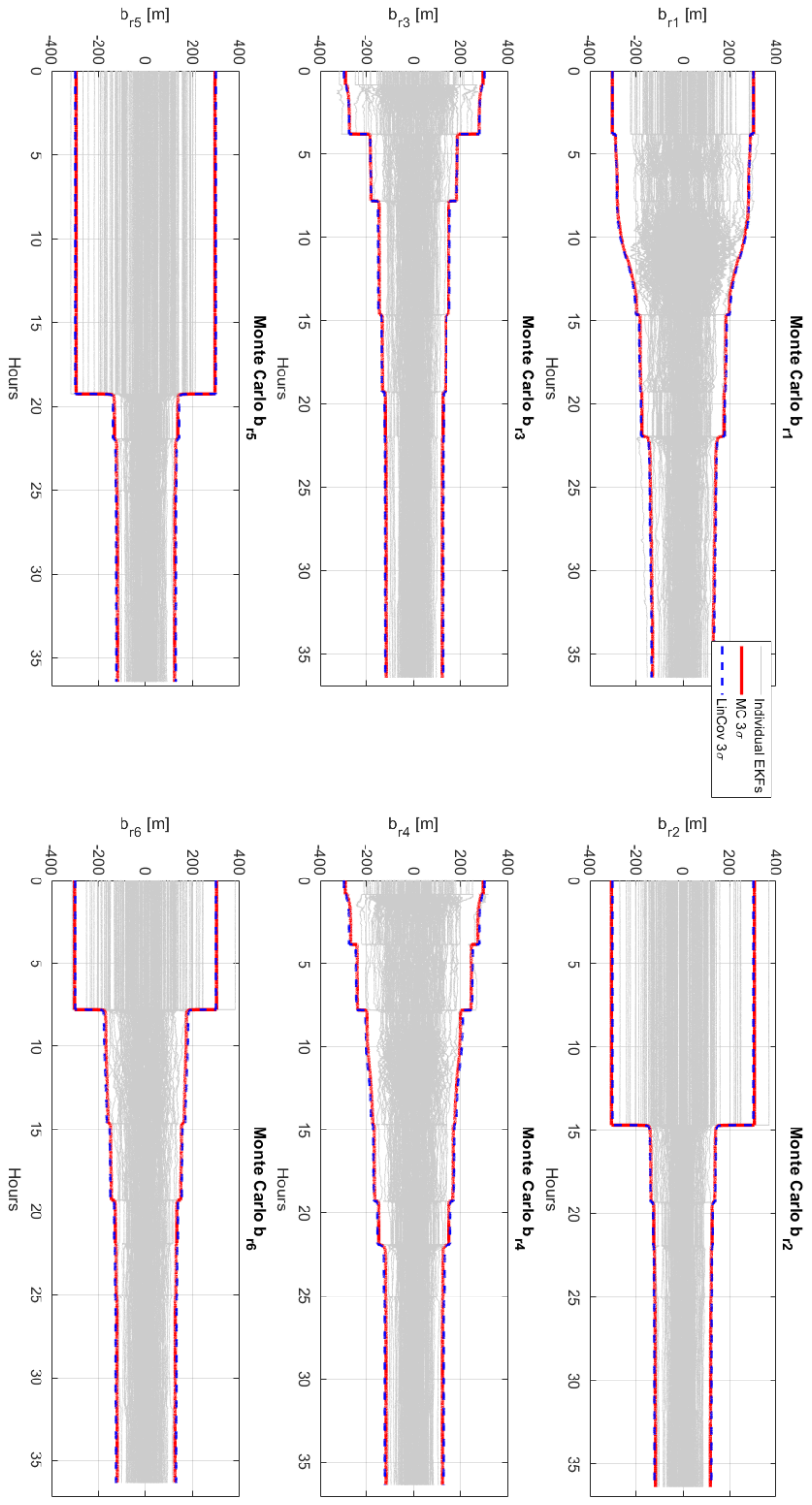

Fig. 5.6: Range Biases: CM-TCM1

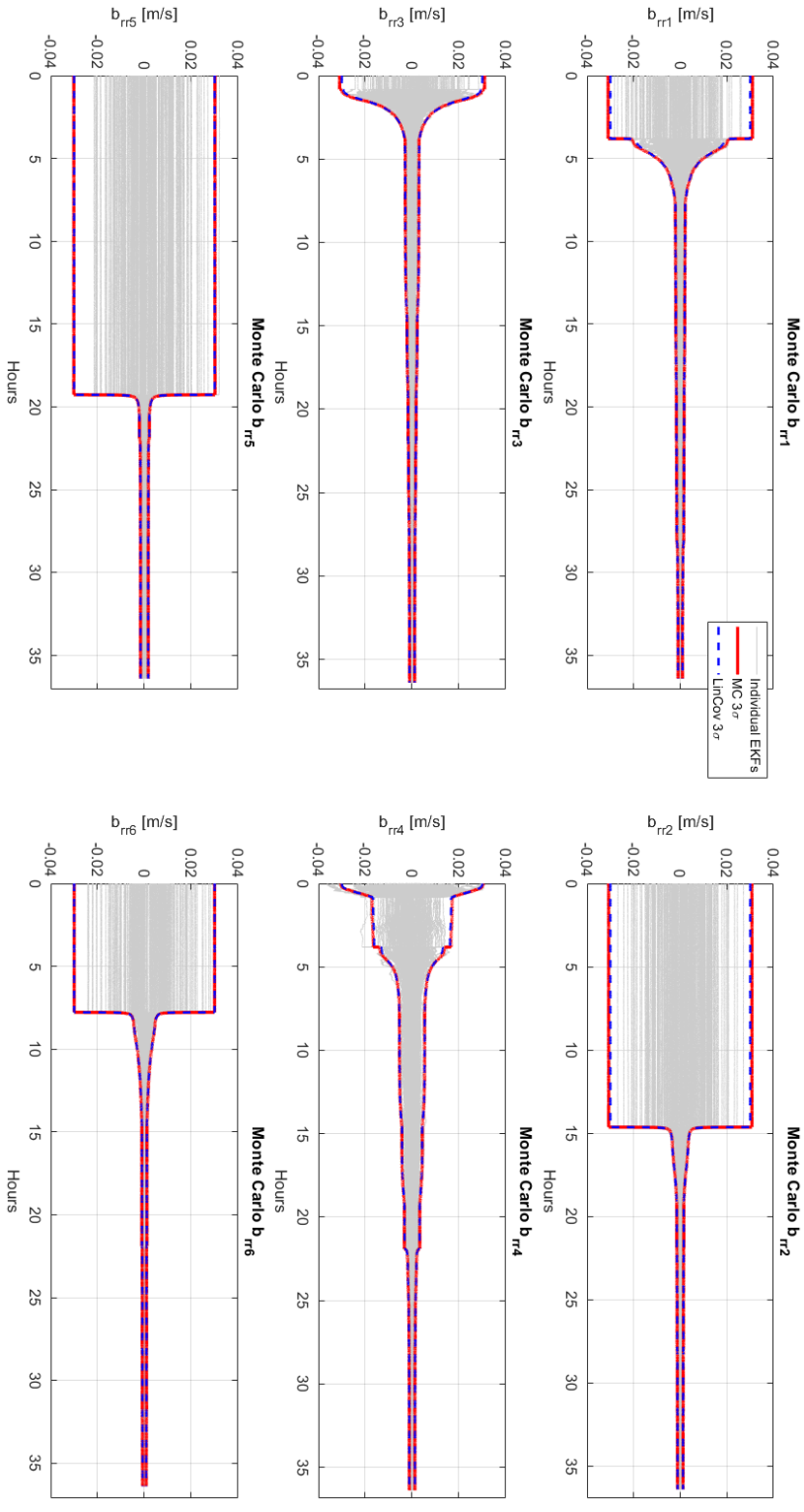

Fig. 5.7: Range-rate Biases: CM-TCM1

5.4 Lunar Orbit Simulation Setup and Values

The simulation parameters used in both the LinCov and Monte Carlo analyses in lunar orbit are recorded below in Table 5.4

Table 5.4: Simulation Setup Values: Lunar Orbit

Parameter	Symbol	Value	Units
Initial Position Error	$\sigma_{r,0}$	1	km
Initial Velocity Error	$\sigma_{v,0}$	1	m/s
Range Measurement Noise	σ_r	100	m
Range-rate Measurement Noise	$\sigma_{\dot{r}}$	1	m/s
Range Bias Steady State	σ_{b_r}	100	m
Range-rate Steady State	$\sigma_{b_{\dot{r}}}$	1	m/s
Range Bias Time Constant	τ_{b_r}	$1e^9$	s
Range-rate Bias Time Constant	τ_{b_r}	$1e^9$	s
SRP Steady State	σ_{ψ}	$8e^{-9}$	m/s^2
SRP Time Constant	τ_{ψ}	$1e^9$	s
Continuous Process Noise Strength	Q	$1e^{-12}$	m^2/s^3

Note that all values are the same except for the initial position errors. This is done since the linear region is tighter in lunar orbit. The nominal trajectory has an orbit of 100 km above the lunar surface, for a total size of 1,838 km. This small orbit, and the impact of the highly nonlinear, spherical harmonic gravity terms, makes the linearization more sensitive.

5.5 LLO Results

The true inertial navigation errors for the lander's position and velocity from 1,000 Monte Carlo runs are shown below in Table 5.5. The results from 6 orbits are shown:

Table 5.5: Monte Carlo Simulation Errors: LLO

OD Segment	LLO.1	LLO.3	LLO.5	LLO.7	LLO.9	LL0.11
Inertial Errors:						
σ_{r_x} [m]	15.176	27.411	22.825	49.685	43.366	43.103
σ_{r_y} [m]	89.676	152.120	103.489	177.113	123.629	108.362
σ_{r_z} [m]	39.728	44.317	19.067	11.503	8.658	19.055
σ_{v_x} [mm/s]	9.504	15.746	10.244	16.091	8.799	3.328
σ_{v_y} [mm/s]	31.819	37.257	13.591	6.411	8.397	19.742
σ_{v_z} [mm/s]	77.452	127.750	88.297	149.267	105.271	94.422

The true inertial navigation errors from the Linear Covariance are shown below in Table 5.6:

Table 5.6: Linear Covariance Errors: LLO

OD Segment	LLO.1	LLO.3	LLO.5	LLO.7	LLO.9	LL0.11
Inertial Errors:						
σ_{r_x} [m]	15.071	27.672	22.425	49.552	41.608	42.603
σ_{r_y} [m]	89.208	152.655	102.614	176.849	118.587	107.251
σ_{r_z} [m]	39.642	44.385	19.092	11.246	8.120	18.656
σ_{v_x} [mm/s]	9.444	15.841	10.146	16.005	8.448	3.331
σ_{v_y} [mm/s]	31.614	37.476	13.362	6.019	7.812	19.436
σ_{v_z} [mm/s]	77.156	128.097	87.558	148.990	100.960	93.379

Note how the greatest difference between the inertial navigation errors found by the Monte Carlo analysis and LinCov is 6.97%. This largest percentage error comes from an absolute difference of just 0.585 mm/s.

Figure 5.8 below depicts the individual true position navigation errors in Orbit 3 from the Monte Carlo analysis, the respective 3σ standard deviations from the Monte Carlo data, and the 3σ standard deviations from the LinCov analysis. Note how the LinCov errors match the Monte Carlo results throughout the orbit.

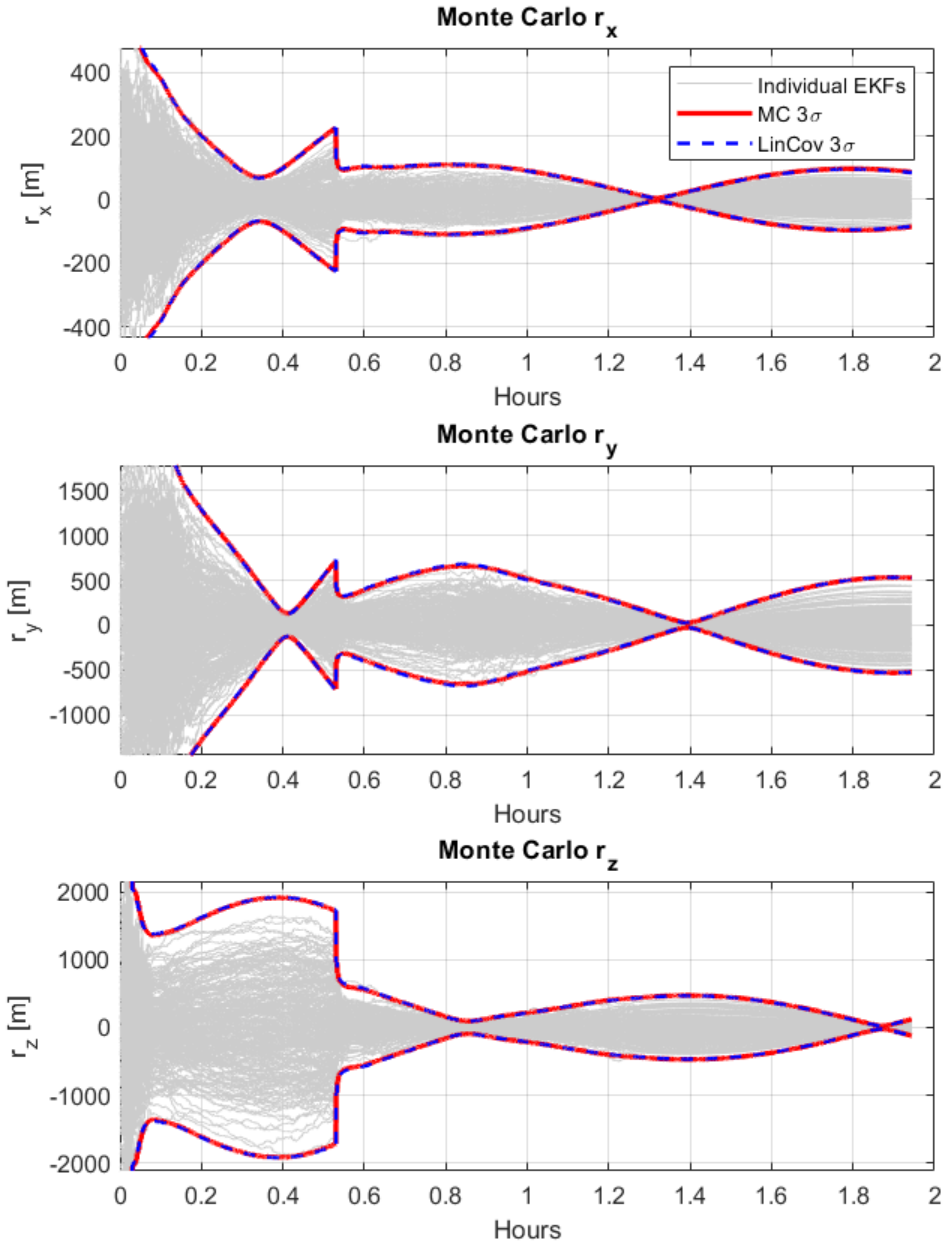

Fig. 5.8: Inertial Position Errors: Orbit 3

Figure 5.9 below depicts the individual true velocity navigation errors for Orbit 3 from the Monte Carlo analysis, the respective 3σ standard deviations from the Monte Carlo data, and the 3σ standard deviations from the LinCov analysis. Note how the LinCov errors match the Monte Carlo results throughout the orbit.

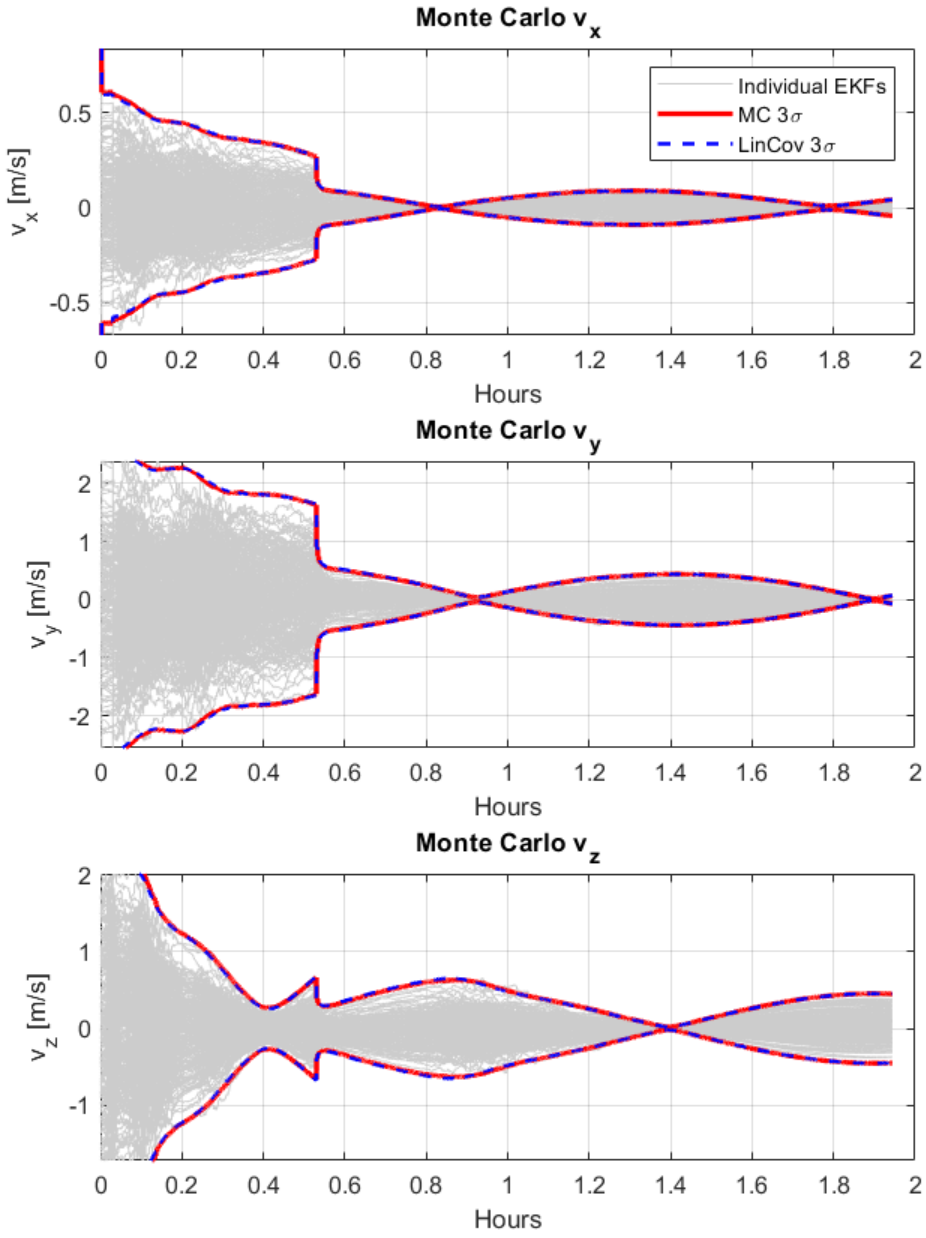

Fig. 5.9: Inertial Velocity Errors: Orbit 3

Figures depicting how the errors associated with SRP from LinCov are validated through Monte Carlo analysis are omitted due to both studies being unable to estimate the SRP, as in Fig. 5.5. Furthermore, as only one to two stations are used during lunar orbit, plots depicting the station biases are omitted. The estimation of the station biases do match between LinCov and Monte Carlo for each lunar orbit.

5.6 Validation Discussion

Thus the Linear Covariance algorithm has been validated with a Monte Carlo analysis, with the largest difference between the errors in cislunar space being 3.56% and in lunar orbit 6.97%. While the importance of determining the estimation errors from a nonlinear system with Monte Carlo analysis cannot be overlooked, the time saved by using linearization is dramatic. Depending on the length of the OD segment, a Monte Carlo analysis with 1,000 individual EKF runs can take between 15 to 25 minutes, while the LinCov analysis takes less than a second.

Linear Covariance and other linearization techniques are thus better suited for generating optimal ground station tracking schedules. Potentially thousands of tracking schedules need to be analyzed for optimization per OD segment, and doing so with a Monte Carlo analysis would not be feasible.

CHAPTER 6

OPTIMAL RANGE PLACEMENT WITH LINEAR COVARIANCE

With the LinCov tool validated by the Monte Carlo analysis, the first navigation optimization problem can be addressed. Intuitive Machines has expressed concerns that, during some OD segments, transmission of both range and range-rate data may not be feasible due to the lander's communication system bandwidth. Range measurements are to be transmitted on sub-carrier channels, and other data sent over the sub-carrier channels may be more difficult to extract if range data is present. This issue is especially more prevalent as the lander approaches distances closer to the Moon [21, 24]. For the IM-1 mission and future missions where circuitous trajectories cause the spacecraft to reach distances past the Moon, this issue deserves an analysis.

This chapter covers the simple optimization of when short bursts of range measurements should be taken given a tracking schedule. The minimization of final position and velocity errors are discussed. Through spanning the entire sample space, the optimal placement of range measurements is found for a one and two dimensional study.

6.1 Problem Overview

Figure 6.1 depicts the Benchmark schedule for the OD segment CM-TCM1, where range-rate measurements are to be processed during the entire segment. Note how range measurements are not taken during the OD segment, except for during a 3 hour segment at the beginning.

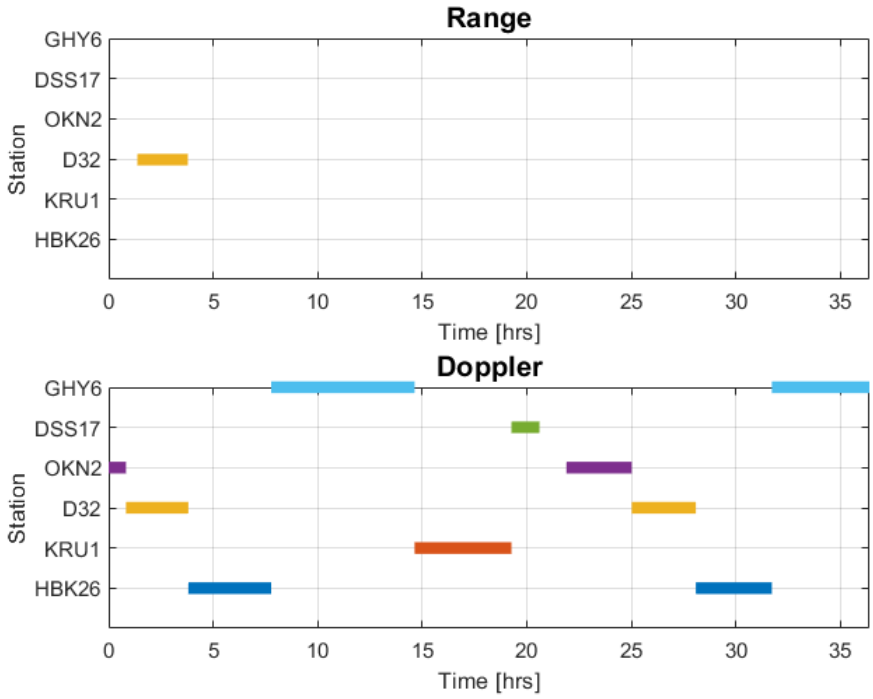

Fig. 6.1: CM-TCM1 Benchmark Tracking Schedule

Starting range measurement generation from station D32 is one of the many solutions that exist. An optimization can thus be applied where each time in the OD segment is treated as the start time in which range measurements will taken for a certain period.

This optimization problem is considerably simpler compared to other navigation optimization problems considered later in the thesis. Under the assumption that range measurements can only be generated in n portions from n station, this is an n dimensional optimization problem. Due to the simplicity of the optimization problem and the speed of LinCov, each configuration in the solution space can be individually analyzed and plotted.

6.2 1 Segment Range Optimization

6.2.1 Optimization Variables and Considerations

Optimization requires a set of parameters that are varied in order to minimize some objective. The optimization object is a vector containing all parameters that are altered in order to find the optimal solution. For one range segment, the optimization object is simply the time when range measurements will begin:

$$\boldsymbol{s}_1 = t_1 \tag{6.1}$$

Another variable to be considered is the measurement duration, which refers to how long the station is allowed to take range measurements. Since longer range measurement segments will inherently lead to better navigation solutions, the measurement duration is not considered an optimization parameter, but rather a setup variable.

Each time at a 10 minute discretization is tested. At each discretization time in an OD segment, range measurements are placed for the measurement duration. The tracking schedule, with the placed range measurement duration and full range-rate measurements, is analyzed with LinCov to determine the final position and velocity errors. The RSS of the position and velocity navigation errors are used, as both provide singular metrics that include the three dimensional estimation errors.

The problem setup is such that range measurements are taken from one station. If at a discrete time two stations are picked up by the measurement duration, only the first station is considered. Thus as discrete times near the end of station passes, the final errors are expected to increase as the full measurement duration is not being utilized.

For each OD segment in cislunar space, the optimal placement of one range measurement segment with measurement durations of 1 hour, 3 hours, and 5 hours are studied with the LinCov setup parameters in Table 5.1 on page 34. The optimal placement of range measurements in lunar orbit is not considered since studies have shown that range measurements do not significantly change estimation performance in lunar orbit [17,24].

6.2.2 One Segment Results

Figure 6.2 depicts the RSS of the position and velocity components of the final state estimation covariance matrix. The x-axis depicts the time in which range measurements begin to be taken. The y-axis depicts the RSS values of the state estimation at the final time of the OD segment. The plot colors indicate which station is being used when the range measurements are taken. The OD segment depicted is CM-TCM1, where the range measurement duration is 1 hour:

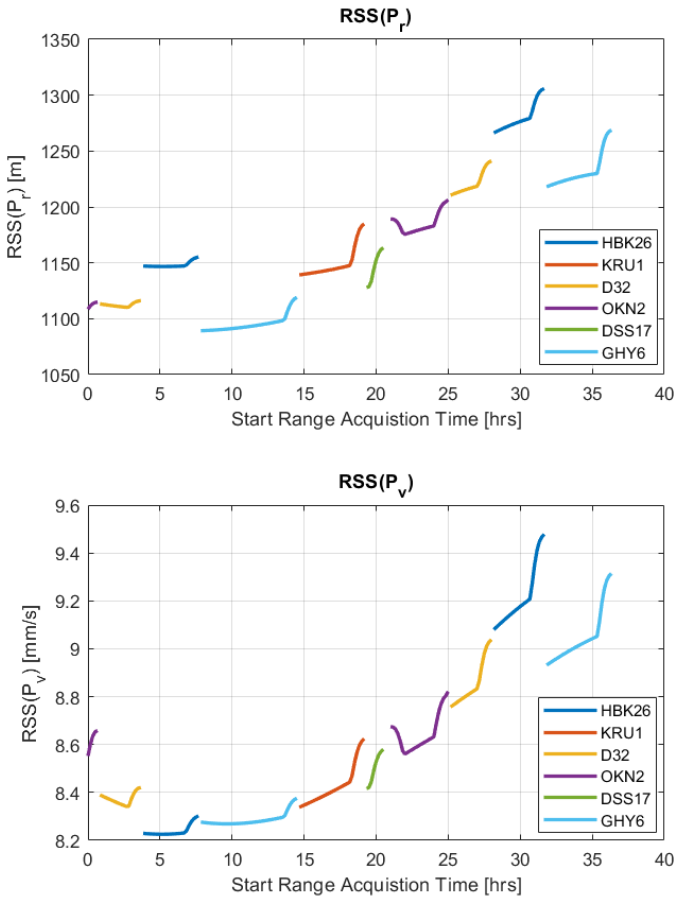

Fig. 6.2: 1D 1hr Optimal Range Placement: CM-TCM1

Note how the optimal placement to minimize position errors at the final time is to take measurements from GHY6, Goonhilly England, at about 7 hours into the OD segment. Also note that doing so does not provide the minimal solution in velocity.

Looking at another OD segment, Fig. 6.3 depicts the RSS of the position and velocity components of the final state estimation covariance matrix for the OD segment TCM1-TCM2.

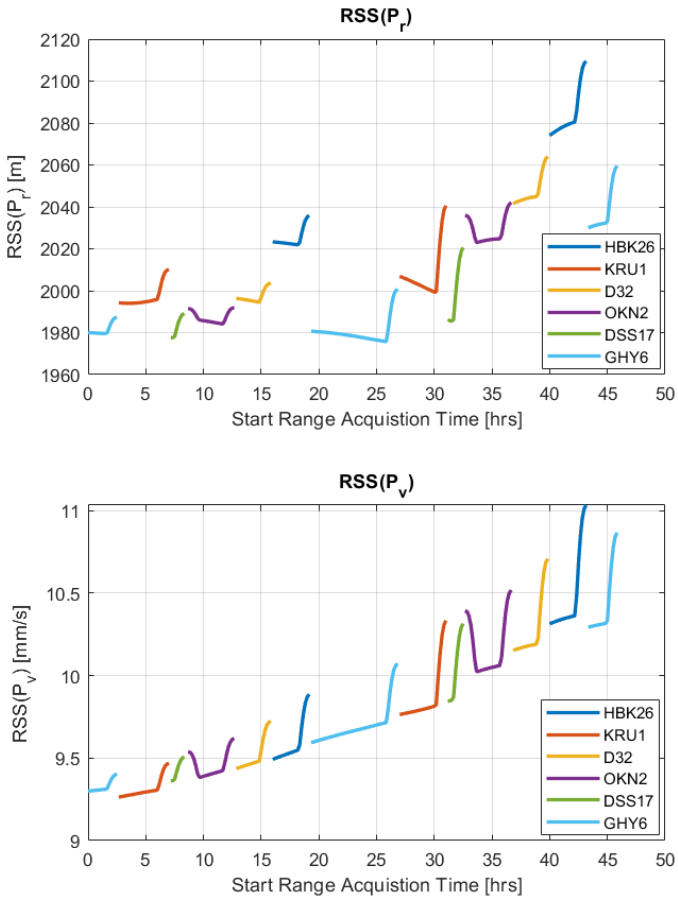

Fig. 6.3: 1D 1hr Optimal Range Placement: TCM1-TCM2

Note again how the optimal placement to minimize position errors comes from taking measurements from GHY6. Also note how in Figures 6.2 and 6.3 there is a significant drop in position errors between HBK26 and GHY6. Figure 6.3 more clearly depicts a linear-like pattern in the velocity optimization, where taking range measurements earlier decreases the final velocity errors.

The final position errors prove to be a more interesting metric as the final velocity errors are not as sensitive to the range placement. The optimal RSS position errors at the final time are reported below in Table 6.1. Reported below are the results for 1 hour, 3 hour, and 5 hour range measurement durations, included with the results where no and full range measurements are taken:

Table 6.1: Optimal 1 Range Measurement Segment Placement: Position RSS

OD Segment	LVS -CM	CM -TCM1	TCM1 -TCM2	TCM2 -TCM3	TCM3 -LOI
0hr Range: [m]	302.08	1,605.37	2,549.46	9,995.52	49.58
Optimal 1hr Range: [m]	280.13	1,089.31	1,976.47	7,526.17	46.64
From Station	OKN2	GHY6	GHY6	GHY6	GHY6
Optimal 3hr Range: [m]	278.91	1,063.82	1,939.54	7,512.91	45.95
From Station	OKN2	GHY6	GHY6	GHY6	GHY6
Optimal 5hr Range: [m]	277.91	1,062.09	1,937.57	7,496.26	45.93
From Station	OKN2	GHY6	GHY6	GHY6	GHY6
Full Range: [m]	241.98	671.96	967.67	2,817.80	36.58

With just 1 hour of range measurements, in OD segments that span up to 48 hours, the RSS of the final position errors can decrease by up to 32%. While taking full range measurements clearly yields the best final errors, the improvement in position errors with just 1 hour is significant. Note that regardless of how long the measurement duration is, the optimal station remains the same. Furthermore, increasing the measurement duration from 1 hour to 5 hours has little impact on the final RSS position errors.

Recall that GHY6 does not have smaller measurement biases or measurement noise than the other stations, and yet is the optimal station in four out of five OD segments. OD segment LVS-CM is unique in that the dynamics are dominated by the Earth's gravity, reducing the estimation problem to the 2-body problem. For each of the measurement durations applied to LVS-CM, OKN2 is chosen at the very end of the OD segment. Emphasizing range measurements near the end of well defined dynamic regions leads to a sharp decrease right before the final RSS is taken.

6.3 Two Segment Range Optimization

6.3.1 Optimization Object Properties with 2 Range Segments

For two range segments, the optimization object contains the time in which each segment starts:

$$\boldsymbol{s}_2 = \begin{bmatrix} t_1 & t_2 \end{bmatrix} \tag{6.2}$$

Thus each combination of the start time parameters is analyzed with LinCov given the setup parameters in Table 5.1 on page 34. Note that the following two optimization objects produce the same tracking schedules and final RSS position and variances as the order in which each start time is placed does not impact the solution:

$$\boldsymbol{s}_{2,1} = \begin{bmatrix} t_1 & t_2 \end{bmatrix} \tag{6.3}$$

$$\boldsymbol{s}_{2,2} = \begin{bmatrix} t_2 & t_1 \end{bmatrix} \tag{6.4}$$

This knowledge implies that the solution space is symmetric, and only half of it needs to be analyzed. Furthermore note that when an optimization object contains times that are equivalent, this will lead to the results generated from the one segment case.

6.3.2 Two Segment Results

Figure 6.4 depicts the RSS of the final position errors for OD segment TCM1-TCM2 in a contour plot. The x and y axes depict the time in which range measurements start for each range segment. For reference, the 1D plots are provided along the x-axis and y-axis to determine what combination of stations produce the optimal RSS errors.

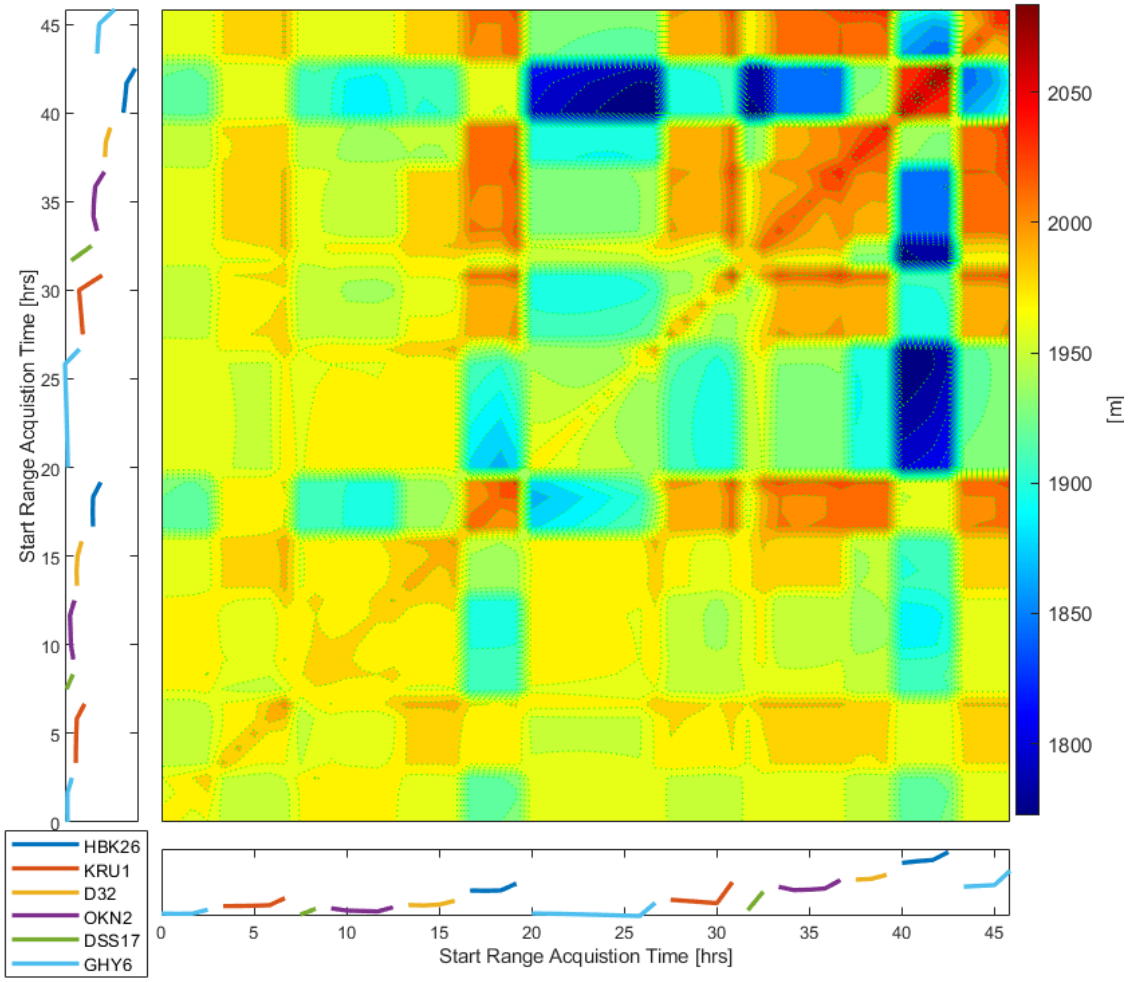

Fig. 6.4: 2D 1hr Optimal Range Placement: Position TCM1-TCM2

Note how the contour is symmetric about the diagonal. The diagonal itself is the 1D case. The optimal placement of the two stations is located in the dark blue region, corresponding to HBK26 at 40 hours into the OD segment and GHY6 at 29 hours.

Figure 6.5 depicts the RSS of the velocity errors. The segment depicted is TCM1-TCM2.

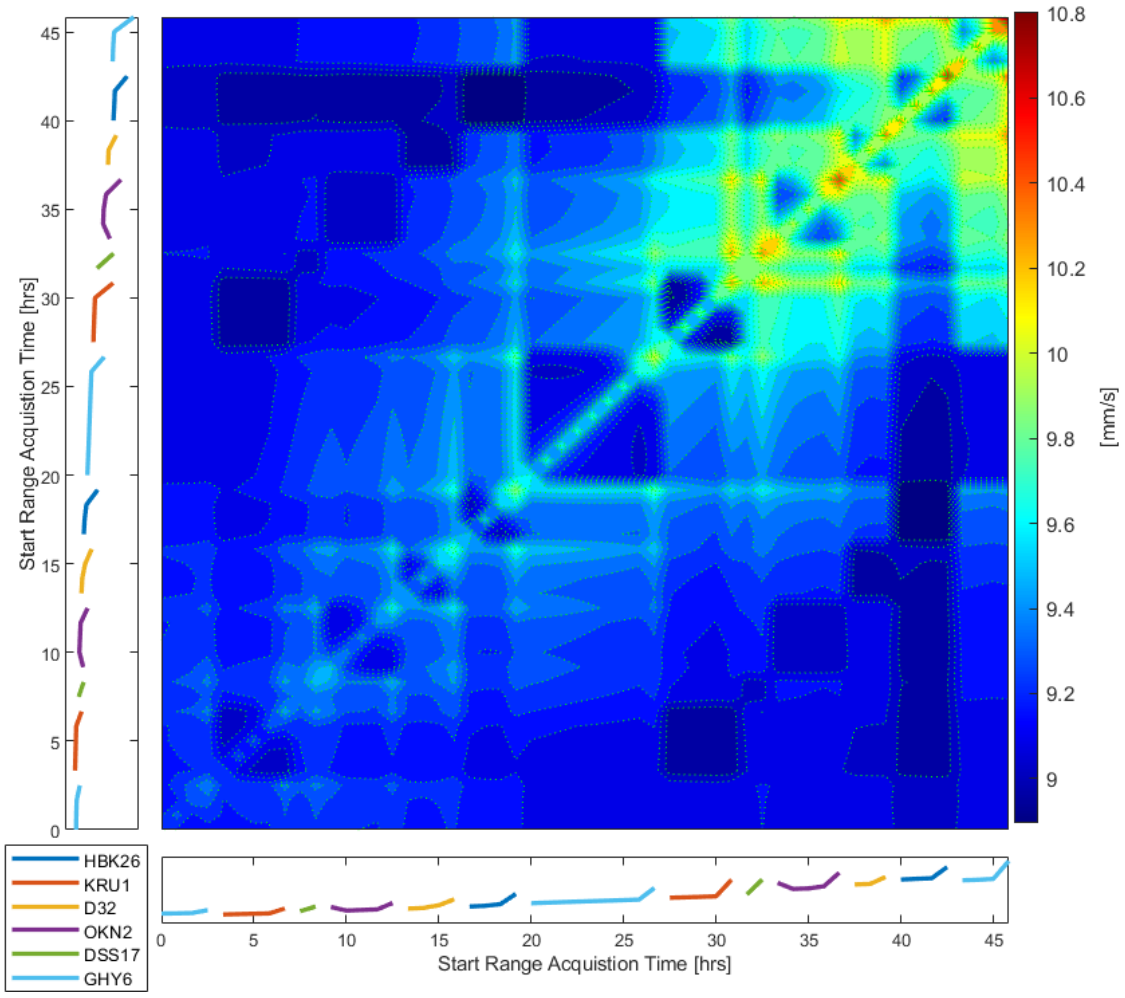

Fig. 6.5: 2D 1hr Optimal Range Placement: Velocity TCM1-TCM2

Note how, generally, the final velocity errors are not as sensitive to the placement of range measurement segments as are the position errors. Furthermore, note that as in the one segment case, the optimal solution to minimize final position errors does well at reducing final velocity errors. On the other hand, the optimal solution to minimize velocity errors does not necessarily minimize final position errors.

Table 6.2 depicts the optimal results in position RSS from the one segment and two segment range measurement placement. Note that all results are shown for a measurement duration of 1 hour.

Table 6.2: Optimal Range Measurement Segment Placements: Position RSS

OD Segment	LVS-CM	CM-TCM1	TCM1-TCM2	TCM2-TCM3	TCM3-LOI
0hr Range: [m]	302.08	1,605.37	2,549.46	9,995.52	49.58
Optimal 1 Segment: [m]	280.13	1,089.31	1,976.47	7,526.17	46.64
From Station:	OKN2	GHY6	GHY6	GHY6	GHY6
Optimal 2 Segment: [m]	275.99	1,046.61	1,772.90	3,660.20	44.95
From Stations:	GHY6	GHY6	GHY6	GHY6	GHY6
	OKN2	HBK26	HBK26	HBK26	HBK26
Full Range: [m]	241.98	671.96	967.67	2,817.80	36.58

Note the significant improvement in OD segment TCM2-TCM3 with a second hour of range. Again, while having full range measurement capability is desirable, the optimal placement of just 2 hours of range can significantly improve estimation performance.

Station GHY6 is part of the optimal solution for all five OD segments. Station HBK26 is optimal for four out of five OD segments, with GHY6, to minimize position errors. These stations are unique not for their smaller measurement biases or noise, but rather their geographic position. GHY6 is the northernmost station at 50 degrees latitude, and HBK26 is the southernmost station at -26 degrees latitude.

6.4 Optimal Range Measurement Discussion

Thus a LinCov analysis has been implemented to place constrained range measurement durations along a given tracking schedule. Due to the speed of LinCov, the time required to analyze all of two segment variations in a 48 hour OD segment takes five minutes, whereas the same analysis with a Monte Carlo analysis would take about 29 days. This analysis and the subsequent tool developed is of great use to future lunar missions when range measurements cannot be continually taken due to communication restrictions.

Furthermore, the results from this study have indicated a strong pattern of emphasizing measurements taken from stations that vary significantly in location. While LinCov is a powerful tool, other estimation methods that strictly analyze the dynamic measurement geometry run more quickly. Thus this research develops a recursive, multi-measurement DOP algorithm.

CHAPTER 7

DILUTION OF PRECISION METHODS

Dilution of Precision (DOP) analysis is a Batch Least-Squares method for navigation analysis. Traditionally used to analyze the measurement geometry of GPS satellites at a fixed instance in time [8], the equations have been expanded to include a time series of measurements to analyze the dynamic measurement geometry [37].

This chapter outlines the generalized DOP method and expands on its use by developing a recursive algorithm to calculate PDOP and VDOP. Furthermore, a weighted DOP algorithm is derived to incorporate both range and range-rate measurements in which a unitless PDOP is obtained through a measurement noise ratio. Lastly, the results obtained through the DOP algorithm are checked with the LinCov tool.

7.1 Generalized Dilution of Precision

Generalized DOP incorporates a time series of measurement data to estimate the state at the final time t_n [37]. Expressing multiple linearized measurements in vector notation:

$$\delta \boldsymbol{z} = \begin{bmatrix} H_0 \Phi_{0,n} \\ H_1 \Phi_{1,n} \\ \vdots \\ H_n \end{bmatrix} \delta \boldsymbol{x}_n + \boldsymbol{\nu} \tag{7.1}$$

Denoting the stacked matrix consisting of the measurement partials and the state transition matrices as A, the Least-Squares estimate is found using the measurement data [2, 38]:

$$\boxed{\delta \hat{\boldsymbol{x}} = \left(A^T A\right)^{-1} A^T \delta \boldsymbol{z}} \tag{7.2}$$

The state error covariance is formulated using the linearized state estimate:

$$P_{\delta \boldsymbol{x}_n} = E\left[(\delta \boldsymbol{x}_n - \delta \hat{\boldsymbol{x}}_n)(\delta \boldsymbol{x}_n - \delta \hat{\boldsymbol{x}}_n)^T\right] \tag{7.3}$$

The linearized measurement $\delta \boldsymbol{z}$ in Eq. 7.1 is substituted into Eq. 7.2:

$$\delta \hat{\boldsymbol{x}}_n = \left(A^T A\right)^{-1} A^T (A\delta \boldsymbol{x}_n + \boldsymbol{\nu}) \tag{7.4}$$

The difference between the Least-Squares estimate $\delta \hat{\boldsymbol{x}}_n$ and the linearized state $\delta \boldsymbol{x}_n$ is taken and substituted into Eq. 7.3

$$\delta \boldsymbol{x}_n - \delta \hat{\boldsymbol{x}}_n = -\left(A^T A\right)^{-1} A^T \boldsymbol{\nu} \tag{7.5}$$

$$P_{\delta \boldsymbol{x}_n} = E\left[\left(A^T A\right)^{-1} A \boldsymbol{\nu}\boldsymbol{\nu}^T A \left(A^T A\right)^{-1}\right] \tag{7.6}$$

The expectation of $\boldsymbol{\nu}^T \boldsymbol{\nu}$ is expressed as the standard deviation of the measurement noise, assuming the measurement errors are equivalent between stations:

$$E[\boldsymbol{\nu}\boldsymbol{\nu}^T] = R = \sigma_\nu^2 I \tag{7.7}$$

The scalar value σ_ν^2 can be factored out of the expectation operator:

$$P_{\delta \boldsymbol{x}_n} = \sigma_\nu^2 E\left[\left(A^T A\right)^{-1} A^T A \left(A^T A\right)^{-1}\right] \tag{7.8}$$

$$\boxed{P_{\delta \boldsymbol{x}_n} = \sigma_\nu^2 \left(A^T A\right)^{-1}} \tag{7.9}$$

Thus the state estimation error covariance is represented at the final time using the Batch Least-Squares solution. For optimization algorithms, it is convenient to provide a single metric to optimize, known as the objective function.

Position Dilution of Precision (PDOP) is formulated by taking the square root of the trace of the position variances:

$$M_r = \begin{bmatrix} I_{3\times3} \\ \\ 0_{3\times3} \end{bmatrix} \tag{7.10}$$

$$\mathrm{RSS}(P_{\delta \boldsymbol{r}_n}) = \sqrt{\mathrm{tr}\left[M_r^T \left(\sigma_\nu^2 \left(A^T A\right)^{-1}\right) M_r\right]} \tag{7.11}$$

$$\mathrm{RSS}(P_{\delta \boldsymbol{r}_n}) = \sigma_\nu \sqrt{\mathrm{tr}\left[M_r^T \left(A^T A\right)^{-1} M_r\right]} \tag{7.12}$$

$$\boxed{\mathrm{RSS}(P_{\delta \boldsymbol{r}_n}) = \sigma_\nu \mathrm{PDOP}} \tag{7.13}$$

Note how PDOP acts as a multiplying factor independent to the measurement noise. Smaller PDOP values indicate better measurement geometry, resulting in smaller state estimation errors. Thus, PDOP provides an intuitive metric to quantify the dynamic measurement geometry between the stations and the spacecraft. Furthermore, for the case where σ_ν pertains to range measurements, PDOP is unitless.

Another common metric in DOP analysis is Velocity Dilution of Precision (VDOP), where the trace of velocity variances are analyzed. For the case where σ_ν pertains to range measurements, VDOP has units of $\frac{1}{s}$, which is more arbitrary for analyzing the dynamic measurement geometry. However, for the case where σ_ν pertains to range-rate measurements, VDOP is unitless and PDOP has units of s, making VDOP the more intuitive metric.

7.2 Computational Efficiency and Recursive Methods

It can become computationally burdensome to continually increase the size of A and calculate A^TA as measurements are incorporated. Thus, a recursive relationship is derived by studying how A^TA evolves as additional measurements are taken. The matrix $\sigma_\nu^2 A^TA$ is called the information matrix. Since the measurement errors are independent of the station geometry, the matrix A^TA is sometimes referred to as the dynamic geometry information matrix, or just the information. Below A^TA is expressed for two measurements to estimate the state at time t_1:

$$A_1 = \begin{bmatrix} H_0\Phi_{0,1} \\ \\ H_1 \end{bmatrix} \tag{7.14}$$

$$\left[A^TA\right]_1 = H_1^TH_1 + \Phi_{0,1}^TH_0^TH_0\Phi_{0,1} \tag{7.15}$$

Processing another measurement at time t_2:

$$A_2 = \begin{bmatrix} H_0\Phi_{0,2} \\ \\ H_1\Phi_{1,2} \\ \\ H_2 \end{bmatrix} \tag{7.16}$$

$$\left[A^TA\right]_2 = H_2^TH_2 + \Phi_{1,2}^TH_1^TH_1\Phi_{1,2} + \Phi_{0,2}^TH_0^TH_0\Phi_{0,2} \tag{7.17}$$

Note that A^TA with three measurements at time t_2 can be expressed in terms of A^TA with two measurements at time t_1 by taking advantage of the fact that for state transition matrices $\Phi_{0,2} = \Phi_{0,1}\Phi_{1,2}$:

$$\left[A^TA\right]_2 = H_2^TH_2 + \Phi_{1,2}^T\left[A^TA\right]_1\Phi_{1,2} \tag{7.18}$$

$$\boxed{\left[A^TA\right]_{k+1} = H_{k+1}^TH_{k+1} + \Phi_{k,k+1}^T\left[A^TA\right]_k\Phi_{k,k+1}} \tag{7.19}$$

Thus new measurement data can easily be incorporated by recursively updating A^TA. However, in order to calculate PDOP at each step, the inverse of A^TA must be taken, which may be computationally difficult or impossible if the matrix is not full rank. To improve the robustness and avoid constantly taking the inverse of A^TA, the small-rank adjustment method for matrix inversion is implemented. The small-rank adjustment method outlines how to find the inverse of the sum of a rank-1 matrix and a full rank matrix [38]:

$$(X + UCV)^{-1} = X^{-1} - X^{-1}U\left(C^{-1} + VX^{-1}U\right)^{-1}VX^{-1} \tag{7.20}$$

Implementing the small-rank adjustment method to the recursive DOP equations:

$$\Gamma_k = \left[A^TA\right]_k^{-1} \tag{7.21}$$

$$\Gamma_{k+1}^- = \Phi_{k+1,k}\Gamma_k\Phi_{k+1,k}^T \tag{7.22}$$

$$\boxed{\Gamma_{k+1}^+ = \Gamma_{k+1}^- - \frac{\Gamma_{k+1}^- H_{k+1}^T H_{k+1}\Gamma_{k+1}^-}{1 + H_{k+1}\Gamma_{k+1}^- H_{k+1}^T}} \tag{7.23}$$

This recursive method does not involve any matrix inversion, except for the necessary initialization of Γ, which is more efficient and leads to fewer computational errors. Note the denominator is a scalar value since measurements are incorporated from only one measurement source.

7.3 Condition Number Implementation

As mentioned, using the matrix inversion lemma is dependent on A^TA being full rank, and thus invertible. However, given machine precision, the matrix inverse may not be accurate and could cause the DOP algorithm to become unstable, despite A^TA being full rank. To avoid inaccuracies, a condition number tolerance is set in the DOP algorithm. The condition number of a matrix is found by taking the ratio of the maximum and minimum singular values [38]:

$$\kappa(A^TA) = \frac{\sigma_{max}(A^TA)}{\sigma_{min}(A^TA)} \tag{7.24}$$

Once the condition number is small enough for accurate inversion, the matrix A^TA is inverted and the recursive method using Γ is used, as depicted below in Fig. 7.1

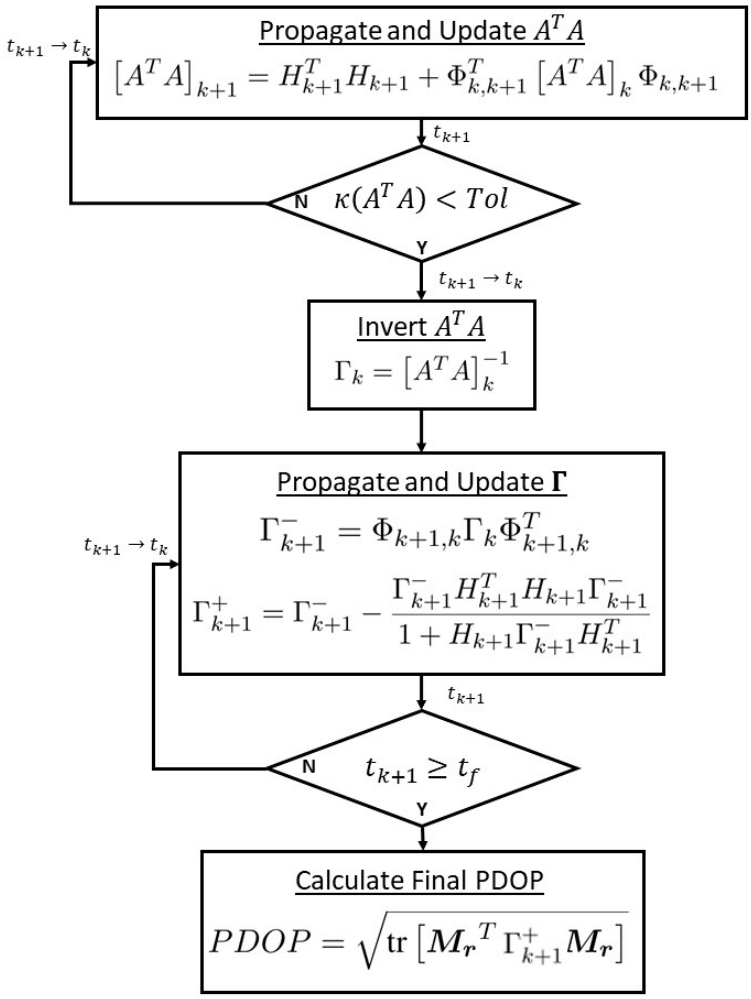

Fig. 7.1: DOP Algorithm Flow Chart

The DOP algorithm runs, propagating and incorporating available measurements, to the end of the OD segment. The PDOP can be calculated at all times once the condition number tolerance is met, ensuring that the results are numerically accurate. If a contact schedule leads to the scenario where the condition number tolerance is never met, a large, default PDOP value is returned to indicate numerical inaccuracy.

7.4 DOP with Multiple Measurement Types

In the derivation of DOP, the expectation of the measurement noise was expressed as a scalar multiplied by the identity matrix. DOP has been restricted to one measurement type since the noise cannot simply be factored out of the expectation operator with multiple measurement types. Here, a new Weighted Least-Squares DOP algorithm is derived that incorporates both range and range-rate measurements. A Weighted Batch Least-Squares solution is expressed as: [2]

$$\delta\hat{\boldsymbol{x}} = \left(A^T W A\right)^{-1} A^T W \delta\boldsymbol{z} \tag{7.25}$$

where W is a weighting matrix. The state error covariance is again formulated using the linearized state estimate:

$$P_{\delta\boldsymbol{x}_n} = E\left[(\delta\boldsymbol{x}_n - \delta\hat{\boldsymbol{x}}_n)(\delta\boldsymbol{x}_n - \delta\hat{\boldsymbol{x}}_n)^T\right] \tag{7.26}$$

The linearized measurement $\delta\boldsymbol{z}$ is substituted into the Least-Squares estimate in Eq. 7.25:

$$\delta\hat{\boldsymbol{x}}_n = \left(A^T W A\right)^{-1} A^T W (A\delta\boldsymbol{x}_n + \boldsymbol{\nu}) \tag{7.27}$$

The difference between the Least-Squares estimate $\delta\hat{\boldsymbol{x}}_n$ and the linearized state $\delta\boldsymbol{x}_n$ is taken and substituted into Eq. 7.26

$$\delta\boldsymbol{x}_n - \delta\hat{\boldsymbol{x}}_n = -\left(A^T W A\right)^{-1} A^T W \boldsymbol{\nu} \tag{7.28}$$

$$P_{\delta\boldsymbol{x}_n} = E\left[\left(A^T W A\right)^{-1} A^T W \boldsymbol{\nu}\boldsymbol{\nu}^T W A \left(A^T W A\right)^{-1}\right] \tag{7.29}$$

Here $\boldsymbol{\nu}$ is a random noise vector from both range and range-rate measurements. The expected value of $\boldsymbol{\nu}^T\boldsymbol{\nu}$ is expressed as R, again assuming each station's measurement noises are equal:

$$P_{\delta\boldsymbol{x}_n} = E\left[\left(A^T W A\right)^{-1} A^T W R W A \left(A^T W A\right)^{-1}\right] \tag{7.30}$$

Defining the weighting matrix W to be the inverse of R:

$$R = W^{-1} \tag{7.31}$$

$$P_{\delta \boldsymbol{x}_n} = E\left[\left(A^T W A\right)^{-1} A^T W W^{-1} W A \left(A^T W A\right)^{-1}\right] \tag{7.32}$$

$$P_{\delta \boldsymbol{x}_n} = \left(A^T W A\right)^{-1} \tag{7.33}$$

To find a unitless PDOP metric that is multiplied by the range measurement noise, the ratio between the range and range-rate noise k is defined:

$$k = \frac{\sigma_r}{\sigma_{\dot{r}}} \tag{7.34}$$

The weighting matrix can thus be expressed using k:

$$W = \frac{1}{\sigma_r^2} K \tag{7.35}$$

Where K is:

$$K = \begin{bmatrix} 1 & 0 \\ 0 & k^2 \end{bmatrix} \tag{7.36}$$

The matrix K here should not be confused with the Kalman gain in a Kalman filter. The value σ_r^2 is factored out of the inverse:

$$P_{\delta \boldsymbol{x}_n} = \sigma_r^2 \left(A^T K A\right)^{-1} \tag{7.37}$$

$$\mathrm{RSS}(P_{\delta \boldsymbol{r}_n}) = \sigma_r \sqrt{\mathrm{tr}\left[M_r^T \left(A^T K A\right)^{-1} M_r\right]} \tag{7.38}$$

$$\boxed{\mathrm{RSS}(P_{\delta \boldsymbol{r}_n}) = \sigma_r \mathrm{PDOP}} \tag{7.39}$$

Note this PDOP is also a dimensionless quantity, but is formulated by using both range and range-rate data. Also note that if a dimensionless VDOP were desired, the range-rate measurement noise could be factored out in a way similar to Eq. 7.35 and the matrix K

redefined. As before, a recursive algorithm is developed to process new measurements:

$$\boxed{\left[A^T K A\right]_{k+1} = H_{k+1}^T K H_{k+1} + \Phi_{k,k+1}^T \left[A^T K A\right]_k \Phi_{k,k+1}} \tag{7.40}$$

And applying the matrix inversion lemma:

$$\Gamma_k = \left[A^T K A\right]_k^{-1} \tag{7.41}$$

$$\Gamma_{k+1}^- = \Phi_{k+1,k} \Gamma_k \Phi_{k+1,k}^T \tag{7.42}$$

$$\boxed{\Gamma_{k+1}^+ = \Gamma_{k+1}^- - \Gamma_{k+1}^- H_{k+1}^T \left(I + K H_{k+1} \Gamma_{k+1}^- H_{k+1}^T\right)^{-1} K H_{k+1} \Gamma_{k+1}^-} \tag{7.43}$$

The first recursion method in Eq. 7.40 is used until the condition number tolerance is met, then Γ is calculated and the second recursion method in Eq. 7.43 is implemented, as depicted in Fig. 7.2:

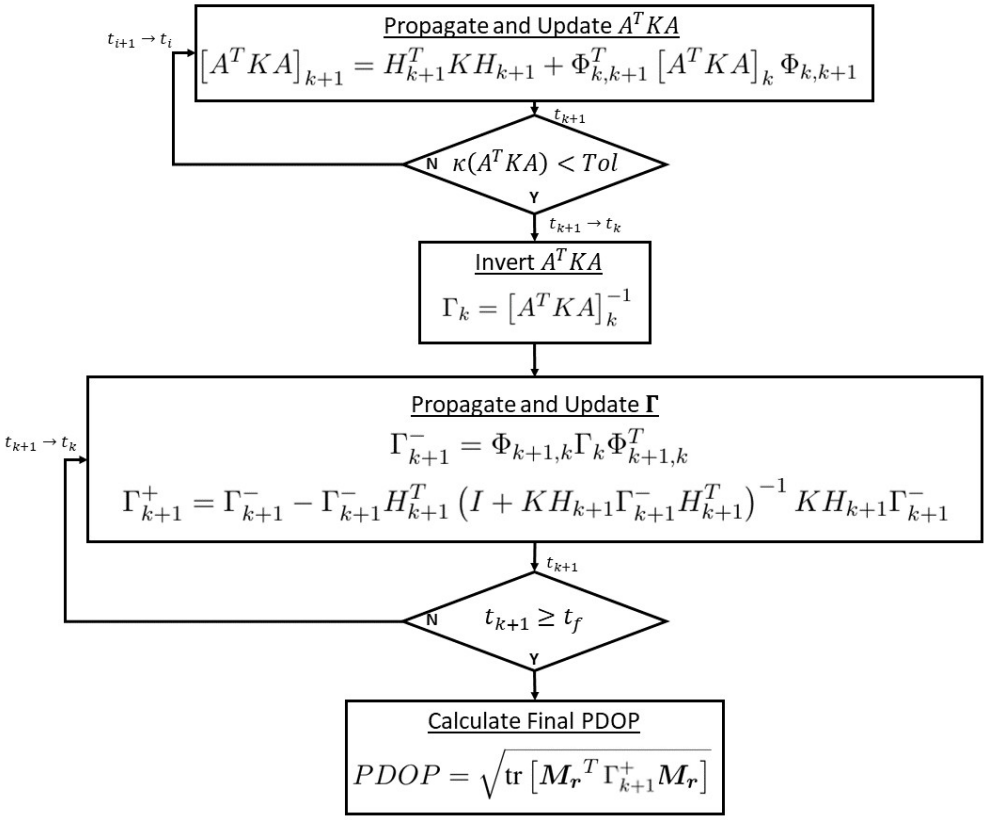

Fig. 7.2: DOP Algorithm Flow Chart: Multi-Measurement Incorporation

7.5 DOP Validation Through LinCov

DOP analysis makes the assumption that the dominant errors come from the uncertainty in the spacecraft's position and velocity, and thus ignores additional states. As DOP analyzes the dynamic measurement geometry, a ground station tracking schedule that optimizes PDOP will also improve the estimation of station biases and any extra states. Since a traditional LinCov analysis assumes conservative noise and bias values to account for any errors from linearization, realistically just focusing on optimizing the measurement geometry is best for real time tracking data. However, for cases where significant process noise or significantly influential additional states are present, LinCov may be the better suited to optimize ground station tracking schedules.

In the case where no additional states are present, DOP and LinCov analyses should produce very similar estimation results. For the IM-1 mission, the lander is expected to experience no more than $Q = 1e^{-14}\frac{m^2}{s^3}$ of continuous process noise from misaligned thruster fire. The percent error between PDOP generated by the DOP algorithm and the normalized RSS of the position covariance generated by a LinCov analysis where no additional states are present is calculated and presented in Table 7.1:

Table 7.1: DOP and LinCov Comparison: $Q = 1e^{-14}\frac{m^2}{s^3}$

OD Segment	LVS-CM	CM-TCM1	TCM1-TCM2	TCM2-TCM3	TCM3-LOI	LOI-DOI
Percent Error	0.087	0.087	0.124	0.044	0.004	0.023

As LinCov has been validated through Monte Carlo analysis, the DOP algorithm has been subsequently validated through LinCov.

7.6 DOP for Ground Station Optimization

Thus a recursive, multi-measurement DOP algorithm has been explicitly derived that may be used to quickly analyze the performance of a ground station tracking schedule. A significant benefit of DOP analysis over LinCov is that the DOP algorithm saves on runtime by strictly analyzing the dynamic measurement geometry by assuming the dominate sources of uncertainty are in the spacecraft's position and velocity. On average, the DOP analysis as derived runs $10\times$ more quickly than a LinCov analysis

Another advantage of the DOP algorithm is that it does not require explicit information regarding the measurement noise. For the DOP algorithm containing one measurement type, the algorithm is independent of the measurement noise. The DOP algorithm implementing two measurement types requires a more general knowledge of the ratio between range and range-rate noise. For ground-based range and range-rate measurements, this ratio k is generally between 1×10^3 and 1×10^5.

The DOP analysis is well suited for optimizing entire ground station tracking schedules for OD segments. By analyzing strictly the dynamic measurement geometry of the ground stations and the lander, optimal estimation performance can be achieved through schedule the correct set of stations. Furthermore, since DOP analysis runs more quickly that LinCov, it is better suited for optimization procedure. While not considered for the remainder of this research, ground station optimization with LinCov should be considered when other sources of uncertainty become important.

CHAPTER 8

POSITION DILUTION OF PRECISION: OPTIMAL TRACKING SCHEDULES

Now with the DOP algorithm derived and its validity verified, DOP is implemented in a Genetic Algorithm to produce optimal ground station tracking schedules with respect to PDOP. MATLAB's genetic algorithm is used to alter a set of discrete parameters, creating tracking schedules with varying stations and operation times [36].

This chapter details how the genetic algorithm is implemented, including a discussion on how the optimization object is formed to minimize PDOP, thus optimizing the dynamic measurement geometry. This chapter presents results depicting optimal tracking schedules given a set number of stations in both cislunar space and in lunar orbit.

8.1 Objective Functions and Optimization Objects

The objective function of an optimization problem is the primary metric that is to be minimized [25]. Objective functions must be a scalar metric. While any metric can be used as an objective function, using a value that has a real application to ground station optimization is best. Sometimes objective functions are referred to as cost functions or just the cost. The term objective function is used in this research to avoid confusion with discussions on operational costs.

The optimization object is a vector that contains the parameters that are changed by the optimization algorithm to minimize the objective function. The parameters in the optimization object can be subjected to linear constraints, nonlinear constraints, and integer constraints.

8.1.1 Position Dilution of Precision

Position Dilution of Precision (PDOP) is the primary objective function for this chapter. By minimizing PDOP, the dynamic measurement geometry is optimized with respect to the lander's position. Furthermore, PDOP provides an intuitive, unitless metric to quantify the estimation errors.

Velocity Dilution of Precision (VDOP) is another common metric that could be used for optimization and, depending on how the multi-measurement DOP algorithm is formed, may also be unitless. PDOP is chosen over VDOP due to its more common use in other forms of DOP analysis and its sensitivity to tracking schedules. Results in Fig. 6.5 on page 57 from the study done on optimal range measurement placement shows that the final velocity errors are not nearly as sensitive to measurement optimization as final position errors. The results in Fig. 6.4 also indicate that by minimizing final position errors, the final velocity errors are reduced to an acceptable and near optimal values. Ultimately, higher velocity errors directly cause position error growth through propagation. Thus when final position errors are optimal, the velocity errors should be significantly reduced.

While an optimal tracking schedule with respect to PDOP may not be optimal with respect to VDOP, the VDOP should be decreased to acceptable and potentially optimal levels. Before an optimal tracking schedule with respect to PDOP is implemented, analysis should be performed to determine whether the velocity errors are acceptable.

Lastly, PDOP has potential for future lunar missions. Future optimization may be desired to determine the location of stationary objects such as lunar rovers or stations. Since these will have little to no velocity, PDOP is the logical choice for optimizing the measurement geometry.

8.1.2 Continuous PDOP Optimization Object

The optimization object for to minimize PDOP contains parameters that identify the station and the swap times between them. For example, a tracking schedule that contains two stations has the optimization object:

$$\boldsymbol{s} = \begin{bmatrix} N_1 & N_2 & t_{1:2} \end{bmatrix}^T \tag{8.1}$$

where N_1 and N_2 are any of the six available stations, and $t_{1:2}$ indicates the time when tracking swaps from station N_1 to N_2. For an optimal tracking schedule with three stations, the optimization object is:

$$\boldsymbol{s} = \begin{bmatrix} N_1 & N_2 & N_3 & t_{1:2} & t_{2:3} \end{bmatrix}^T \tag{8.2}$$

where N_1, N_2, and N_3 are any of the six available stations, $t_{1:2}$ indicates the time when tracking swaps from station N_1 to N_2, and $t_{2:3}$ indicates the time when tracking swaps from station N_2 to N_3. This pattern is generalized to include any number of stations to an OD segment with the optimization object:

$$\boldsymbol{s} = \begin{bmatrix} N_1 & N_2 & \cdots & N_n & t_{1:2} & t_{2:3} & \cdots & t_{(n-1):n} \end{bmatrix}^T \tag{8.3}$$

where the size of the optimization object depends on the number of stations to be considered for an OD segment. The total size of the optimization object is ($2N$-1) with N stations and *N-1* swap times.

The swap times are subjected to linear constraints so that each swap time is greater than the previous. Equation **??** below depicts an example linear constraint when three stations are implemented:

$$\begin{bmatrix} 0 & 0 & 0 & 1 & -1 \end{bmatrix} \begin{bmatrix} N_1 \\ N_2 \\ N_3 \\ t_{1:2} \\ t_{2:3} \end{bmatrix} \leq -t_d \tag{8.4}$$

Practically, ground stations must be used for some duration of time, otherwise they cannot be scheduled at all. The delay time t_d is set to ensure set to ensure there is a delay between any two swap times. For this research, t_d is set at a half hour, which is considered low for practical applications, but proves interesting for analysis.

Formulating the optimization object with swap time parameters instead of start and stop time parameters is advantageous in a few ways. First, the size of the optimization object reduces from $3N$ with separate start and stop time parameters to ($2N$-1) with swap time parameters. As the number of parameters increases, the optimization algorithm less consistently converges to the optimal solution.

Second, swap time parameters encourage the formulation of continuous tracking schedules. Additional measurements never worsen estimation performance, meaning the optimal solution is as close to continuous coverage as possible, given a number of stations. Thus formulating the optimization object with swap time parameters helps the optimization algorithm focus on the sample space more likely to contain the minimum. Continuous tracking schedules are also desired by Intuitive Machines for the IM-1 mission in order to ensure mission success. For future missions, tracking schedules with less coverage may be desired to save on operational costs, which are discussed in subsequent chapters.

The optimization problem at hand is an integer problem, since the station numbers must be integer values 1-6 corresponding to an actual station. For this research, the swap time parameters are set at discrete 30 minute increments. While the ground stations are assumed to provide measurements every 10 seconds, the discretization of the swap times does not need to be so precise. By discretizing the swap times at 30 minute increments, the number of possible combinations for the optimization object dramatically decreases. For example, a 20 hour OD segment that has three stations and a swap time discretization set at 10s has over 13.64 trillion combinations. By discretizing the swap times at 30 minute increments, the number of possible configurations decreases to just over 171,000. Verification was performed by the author to ensure that optimal solutions produced at various discretizations yielded the same results.

8.2 Optimization Procedure

8.2.1 Genetic Algorithm

Genetic algorithms are well suited to find the best optimization object for integer problems with complex objective functions. [27, 28] Using MATLAB's genetic algorithm optimization toolbox [36], the genetic algorithm creates an initial random population of objects based on user defined parameters bounds. From each of these optimization objects, a ground station tracking schedule is created and run through the DOP algorithm to obtain the PDOP at the final time. The genetic algorithm creates new optimization objects based on the previous population and iterates until an optimal ground station tracking schedule is found. The optimization process is depicted in Fig. 8.1:

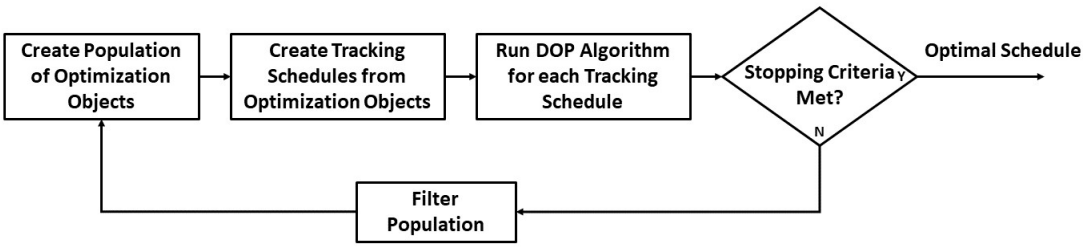

Fig. 8.1: Ground Station Tracking Schedule Optimization Procedure

The stopping criteria include run time, number of generations, and a function tolerance, where the genetic algorithm terminates if any one of the criteria is met, however, the main criteria for this work is the objective function tolerance. The genetic algorithm is applied to each OD segment and subsegment in cislunar space to find an optimal ground station tracking schedule with three stations in the optimization object. With three ground stations, each OD segment is "well covered" in terms of having continuous coverage. The inclusion of subsequent stations to the optimization object yields smaller marginal gains in DOP performance with increasing complexity for the genetic algorithm. However, including more stations decreases the PDOP and may be necessary to ensure mission success.

It is important to note that as the number of stations in the optimization object increases, the confidence that the genetic algorithm provides the global minimum decreases. For a 24 hour OD segment with the half-hour time discretization, there exists over 1.4 billion potential solutions for five stations. For continuous coverage, millions of these configurations could produce PDOP values that are near the global minimum, and the genetic algorithm may have difficulty converging to the absolute global solution due to numerical precision. Furthermore, local minima are always a concern for non-convex optimization problems. To ensure the genetic algorithm approaches the global minimum, a very large initial population is implemented that attempts to span the entire sample space. The genetic algorithm is also run multiple times with different initial populations to ensure consistent solution convergence. Ultimately, the differences between the solution found by the genetic algorithm and the true global minimum should be negligible.

8.2.2 Visibility Report

The optimization procedure requires knowledge on how all available stations may perform in the DOP algorithm. Thus, the measurement partials from every station at all times could be used in the optimization. In order to calculate the measurement partials for all stations at all times, a visibility report is calculated.

The visibility report indicates when a station can generate measurements, or simply when the lander is visible to the station. High fidelity visibility reports are created using details such as the station elevation and surrounding terrain. Intuitive Machines creates high fidelity visibility reports using STK. A simpler visibility report can be quickly calculated and altered through vector logic, and is derived here. Note that low fidelity visibility reports were verified against the high fidelity visibility reports, differing by a matter of minutes.

Figure 8.2 depicts when the lander is visible to a ground station. Each station has a Field of Vision (FOV) that is conservatively set at 15 degrees above the horizon, or at 75 degrees. When the lander is within the station's FOV, it is considered visible.

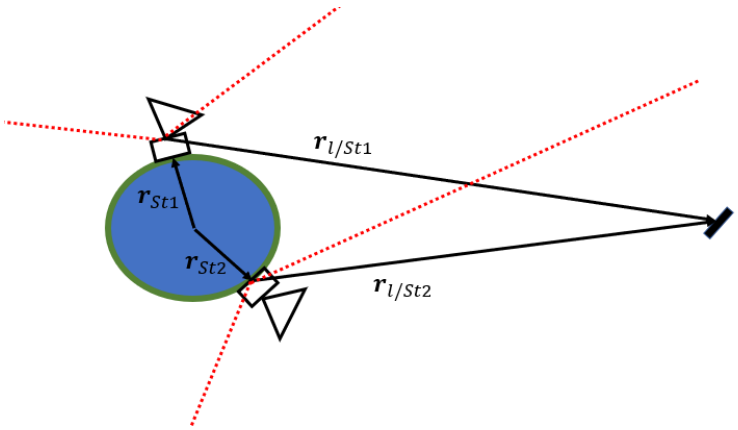

Fig. 8.2: Visibility Generation

Thus the lander is visible to a station according to:

$$\theta = \cos^{-1}(\boldsymbol{i}^T_{\boldsymbol{r}_{l/St}} \boldsymbol{i}_{\boldsymbol{r}_{St}}) \tag{8.5}$$

$$\text{if } \theta \leq \text{FOV} \tag{8.6}$$

The next element in the visibility report is to determine when visibility is lost due to lunar occulation. Figure 8.3 depicts the vector logic for determining lunar occultation:

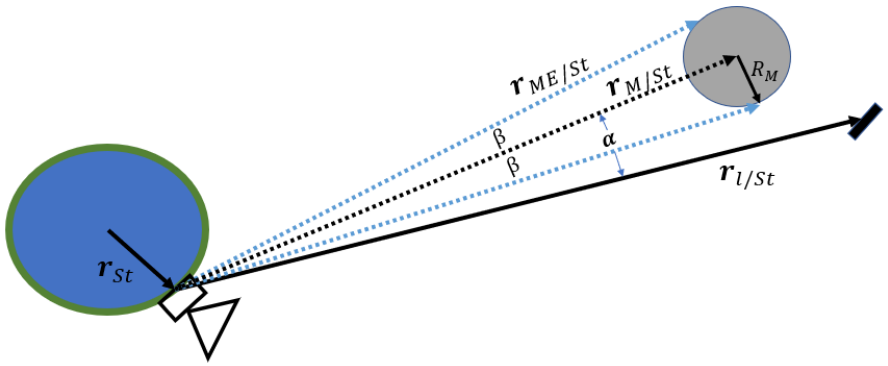

Fig. 8.3: Lunar Occultation

The angle β represents the angle between the position vector of the Moon with respect to a station and the position vector of the Moon's edge with respect to the station. The angle β is calculated as:

$$\beta = \cos^{-1}\left(\frac{||\boldsymbol{r}_{M/St}||}{R_M}\right) \tag{8.7}$$

The angle α represents the angle between the position vector of the Moon with respect to a station and the position vector of the lander with respect to the station. The angle α is calculated as:

$$\alpha = \cos^{-1}(\boldsymbol{i}^T_{\boldsymbol{r}_{l/St}} \boldsymbol{i}_{\boldsymbol{r}_{M/St}}) \tag{8.8}$$

Thus, lunar occultation occurs if both of the following conditions are met:

$$\alpha \leq \beta \tag{8.9}$$

$$||\boldsymbol{r}_{M/St}|| \leq ||\boldsymbol{r}_{l/St}|| \tag{8.10}$$

indicating that if the lander is farther away from that station than the Moon is from the station and is within the Moon's shadow, it is not visible to the station.

With the visibility report, the measurement partials for each station are calculated along the entire nominal trajectory. The measurement partials and the STMs are calculated, stored, and passed into the DOP algorithm, significantly reducing the run time of each DOP algorithm. To further improve the performance of the DOP algorithm, MATLAB's *codegen* is used to generate mex functions [36]. These mex functions allow MATLAB to run functions in C language. The improvement in runtime varies depending on what function is translated to a mex function, but the DOP mex function on average runs 7.5× more quickly that the standard function. By precomputing all of the measurement partials and STMs and by using mex functions, the genetic algorithm is able to evaluate the objective function using the DOP algorithm in less than 0.014 seconds.

8.2.3 Number of Stations Implemented

Each OD segment is analyzed separately to determine an optimal ground station tracking schedule in preparation for an upcoming maneuver. In cislunar space, the OD segments are further divided into subsegments in order to provide intermediate state estimates on an approximately daily basis. The OD subsegments help the optimization algorithm focus on one single rotation of the Earth and the corresponding visible stations. Furthermore, an accurate and precise state estimate is desired operationally by the ground navigation team in order to determine any anomalies during the mission. From LOI to DOI, the OD segment is broken up into six OD subsegments to provide a state estimation solution every two orbits, where each orbit takes approximately two hours.

For the OD segments and subsegments in cislunar space, optimal ground station tracking schedules are found with three, four, and five stations. Additional stations, as is seen in subsequent results, experience diminishing marginal gains in PDOP performance. Thus adding a sixth station to the optimization does not significantly improve PDOP for this trajectory. For the shorter OD subsegments in lunar orbit, optimal tracking schedule with two stations are found.

Note that the solutions presented are optimal given the number of stations. Determining the absolute global PDOP minimum of an OD segment would require adding as many stations as possible with no constraints on how long each station could take measurements. The focus on this research is to provide optimal tracking schedule templates with a set number of stations, allowing the navigation team at Intuitive Machines to alter the schedule as needed while still obtaining the best possible results.

8.3 Optimal PDOP Tracking Schedules: Cislunar Space

Figure 8.4 below depicts the optimal PDOP tracking schedules found by the genetic algorithm for the OD segment LVS-CM:

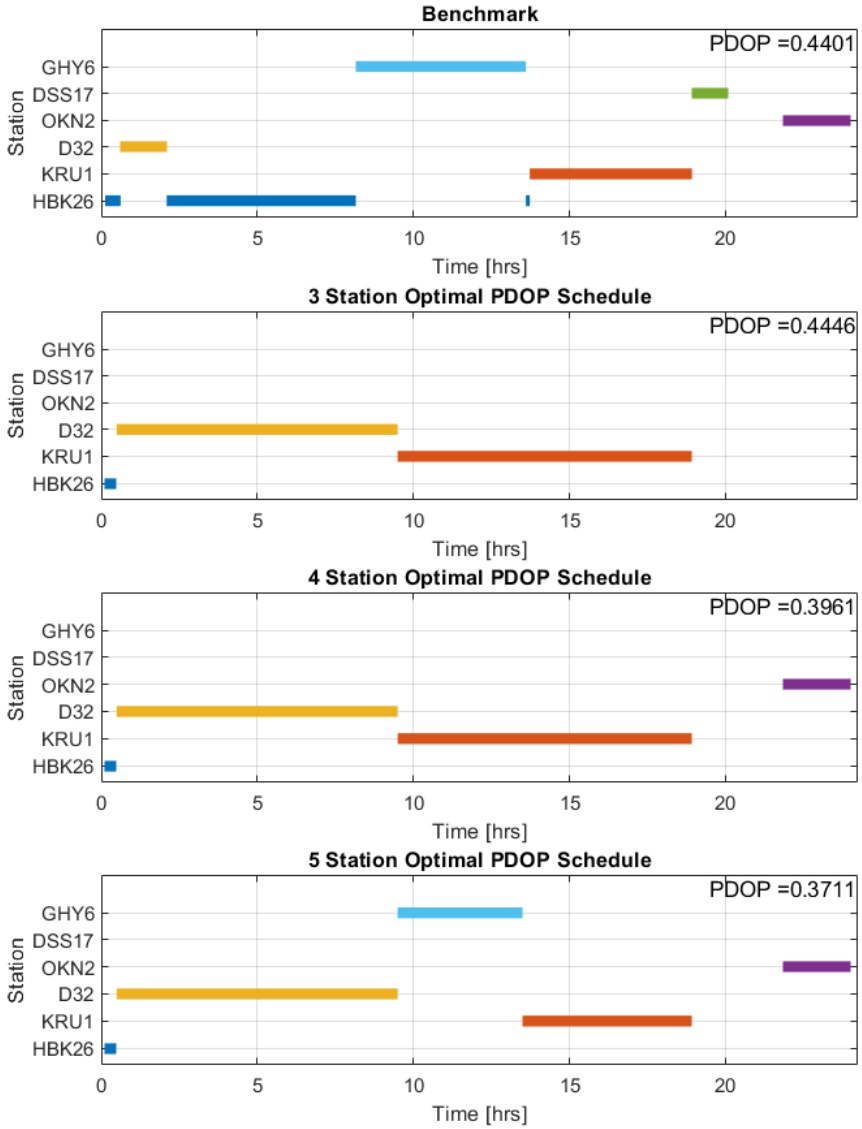

Fig. 8.4: Optimal PDOP Schedule: LVS-CM

Note the optimal configuration with just four stations outperforms the Benchmark that has eight. As previously mentioned, this OD segment is dominated by Earth's gravity and estimation is better than OD segments further in cislunar space.

Figure 8.5 below depicts the optimal PDOP results found by the genetic algorithm for the OD subsegment corresponding to the first half of CM-TCM1:

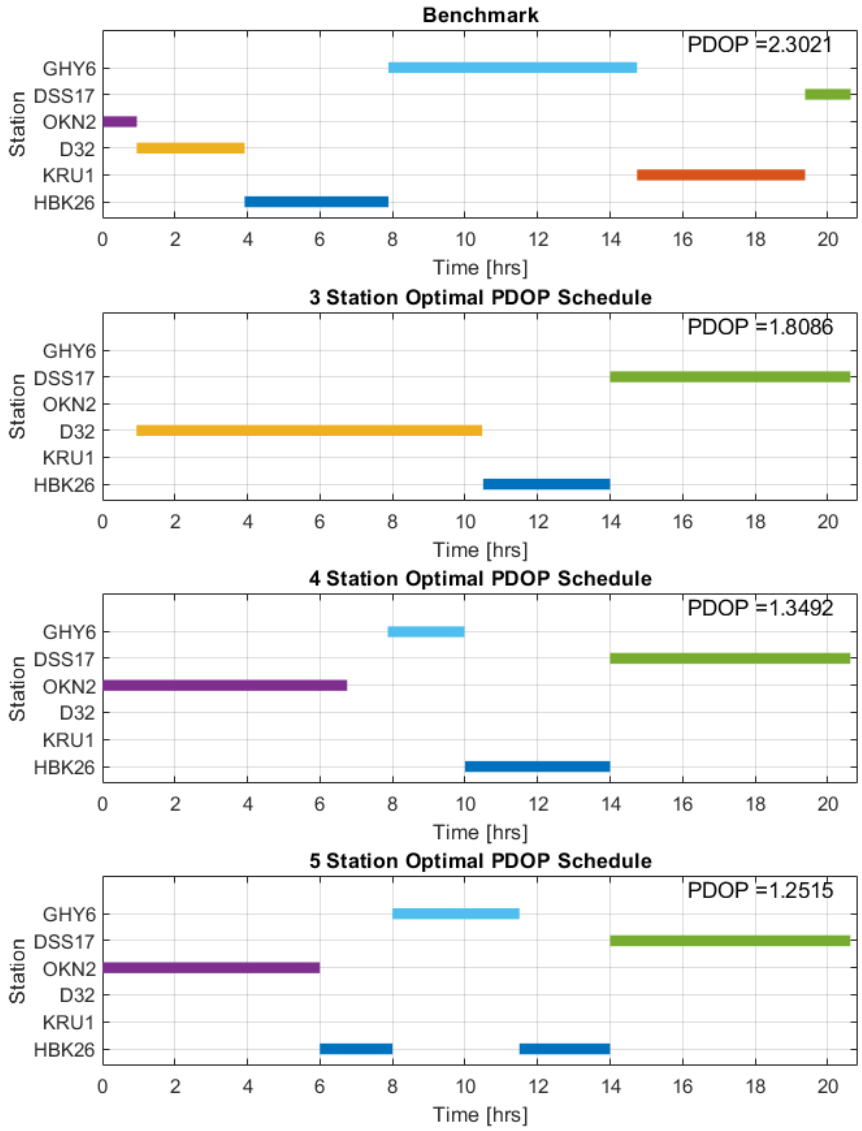

Fig. 8.5: Optimal PDOP Schedule: CM-TCM1H

Note that with just three stations, the optimal configuration outperforms the benchmark by 21%. With the same the number of stations, the optimal configuration performs almost twice as well. Also note the pattern of swapping between GHY6 and HBK26 in the optimal solutions.

Figure 8.6 below depicts the optimal PDOP results found by the genetic algorithm for the OD subsegment corresponding to the second half of CM-TCM1:

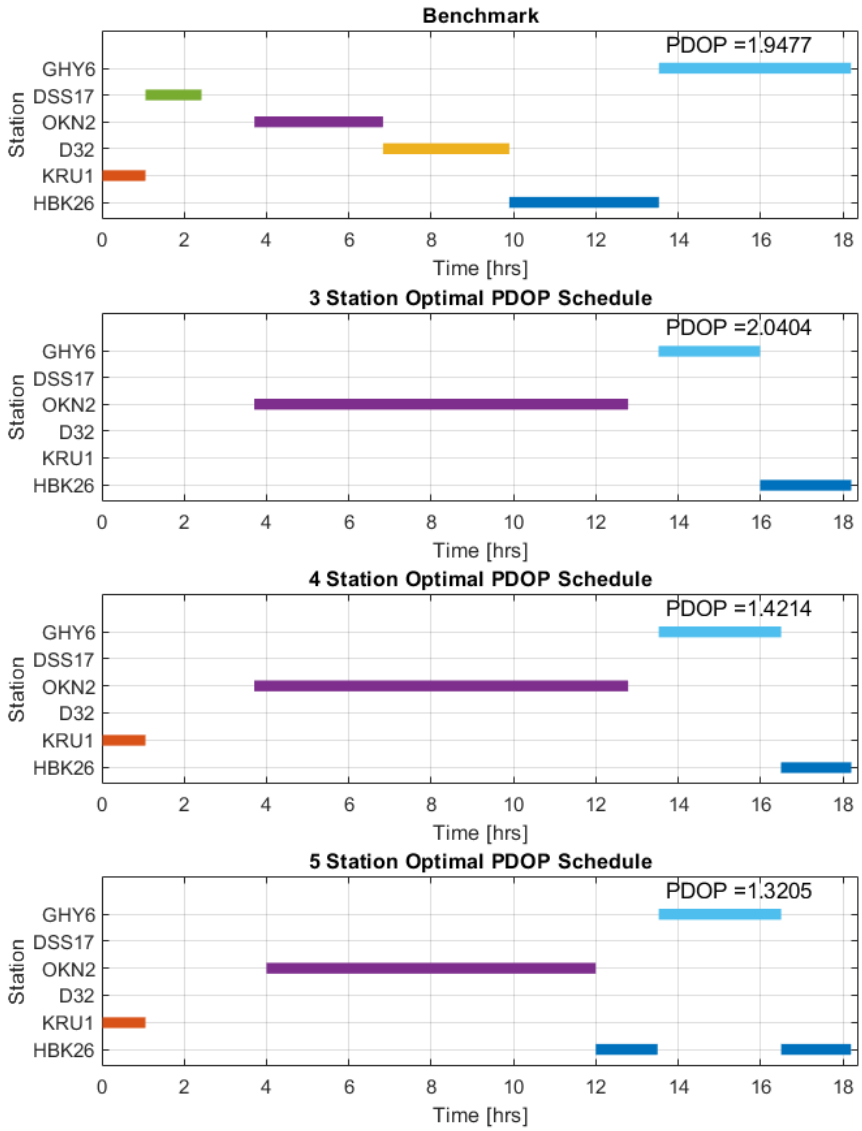

Fig. 8.6: Optimal PDOP Schedule: TCM1H-TCM1

Note that the optimal configuration outperforms the Benchmark with four stations. With four stations, the optimal schedule outperforms the Benchmark by 27%. With five stations, the optimal schedule outperforms the benchmark by 32%. Also note the pattern of swapping between GHY6 and HBK26 in the optimal solutions.

Figure 8.7 below depicts the optimal PDOP results found by the genetic algorithm for the OD subsegment corresponding to the first half of TCM1-TCM2:

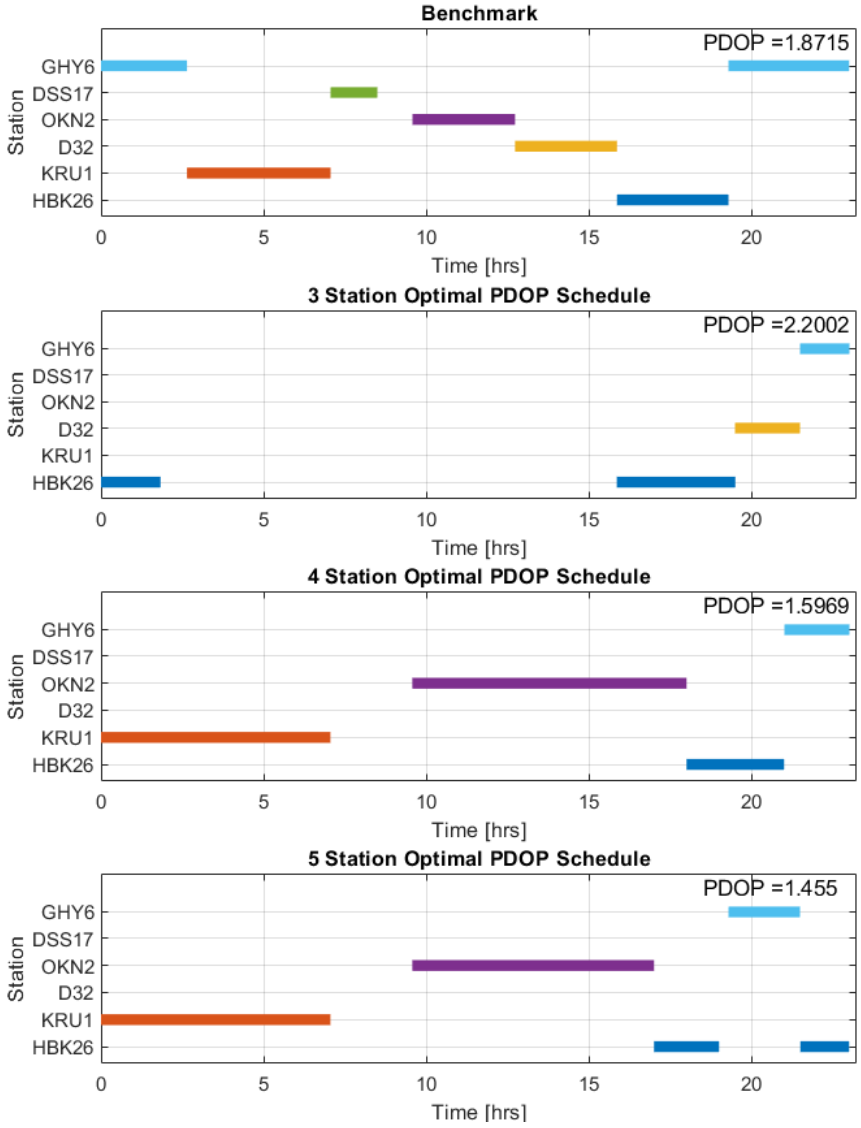

Fig. 8.7: Optimal PDOP Schedule: TCM1-TCM2H

Here the three station optimal schedule demonstrates a "piggyback". The first swap time is 19.5 hours, allowing HBK26 to obtain measurements again after a full Earth rotation. With four stations, the optimal schedule outperforms the Benchmark by 16%, with five stations by 22%.

Figure 8.8 below depicts the optimal PDOP results found by the genetic algorithm for the OD subsegment corresponding to the second half of TCM1-TCM2:

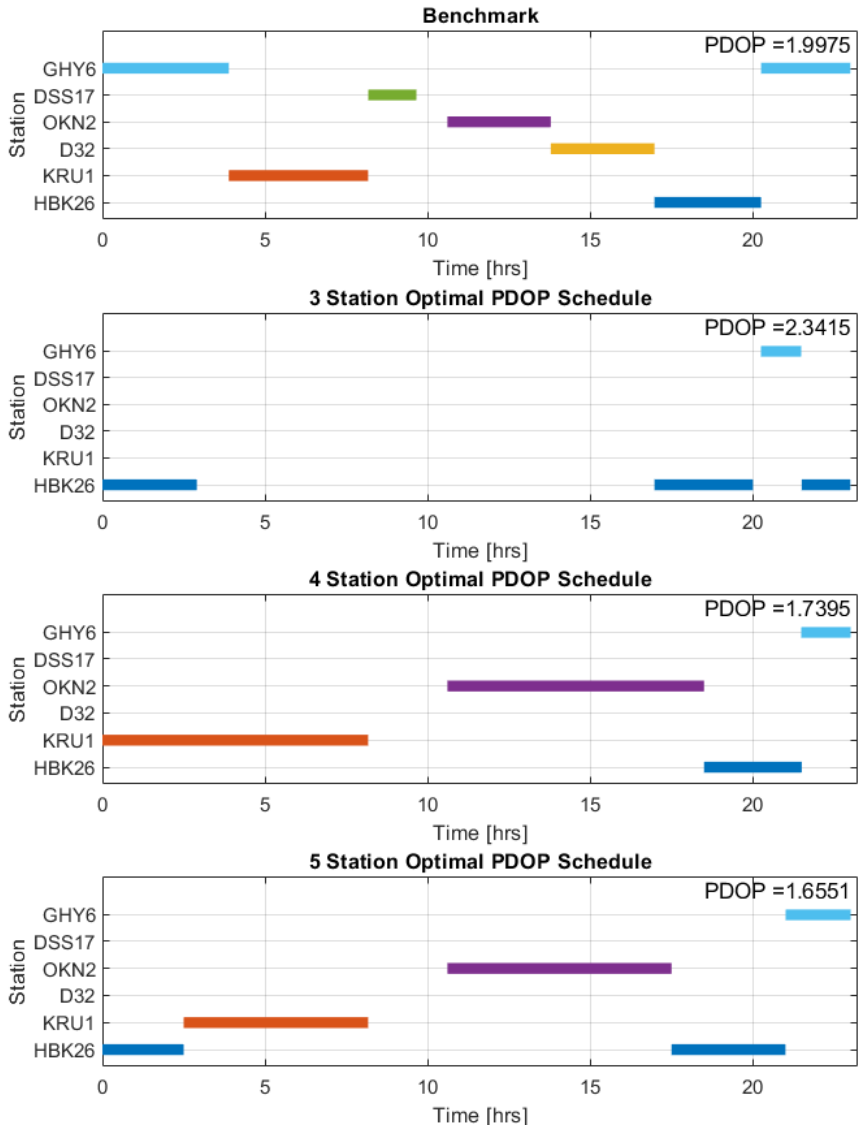

Fig. 8.8: Optimal PDOP Schedule: TCM2H-TCM2

Note that optimal configuration outperforms the benchmark of seven stations with four stations. With four stations, the optimal schedule outperforms the benchmark by 12%. With five stations, the optimal schedule outperforms the benchmark by 17%

Figure 8.9 below depicts the optimal PDOP results found by the genetic algorithm for the OD subsegment corresponding to TCM2-TCM3:

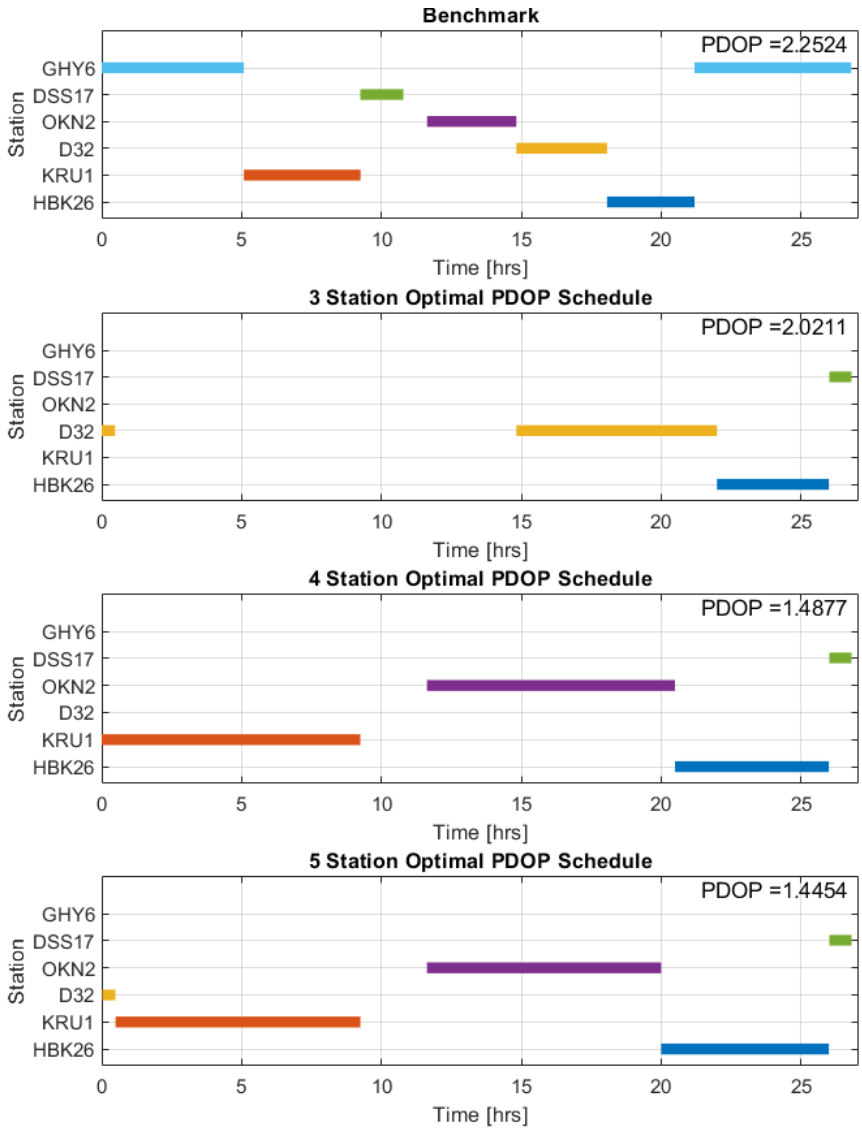

Fig. 8.9: Optimal PDOP Schedule: TCM2-TCM3

With three stations the optimal schedule outperforms the benchmark by 10%, with four stations by 33%, with five stations by 34%. Note that the optimal solutions do not experience the swapping between GHY6 and HBK26. This OD segment is a great example of the need to run the optimization as opposed to following patterns exhibited from other OD segments.

Figure 8.10 below depicts the optimal PDOP results found by the genetic algorithm for the OD subsegment corresponding to TCM3-LOI. Generally, the position errors are very small and less sensitive near perilune, so the final PDOP is taken and minimized two hours prior to LOI.

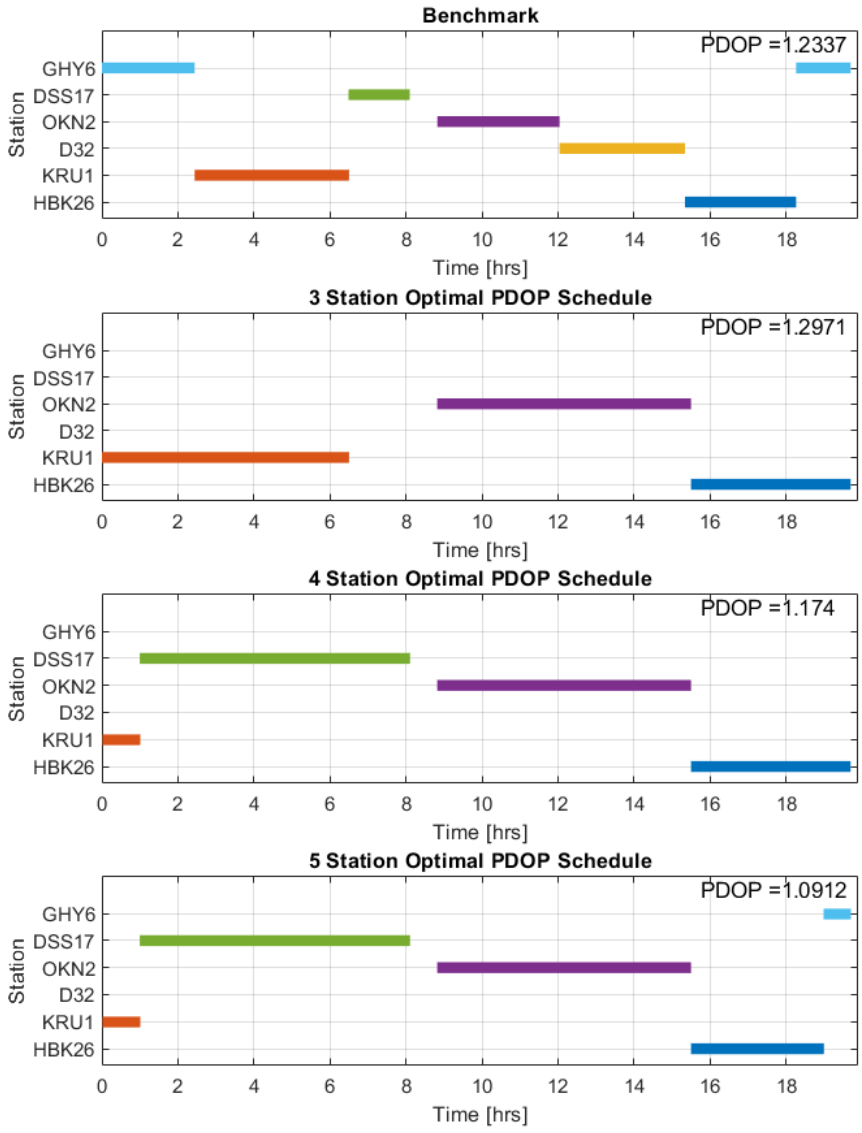

Fig. 8.10: Optimal PDOP Schedule: TCM3-LOI

Note that while the optimal schedules outperform the benchmark by very small margins, they do so with far fewer stations.

Table 8.1 records the PDOP values obtained through the optimization for each OD segment in cislunar space:

Table 8.1: Optimal PDOP Results: Cislunar Space

OD Segment	OD1	OD2.1	OD2.2	OD3.1	OD3.2	OD4	OD5
Benchmark	0.4401 [8]	2.3021 [6]	1.9477 [6]	1.8715 [7]	1.9975 [7]	2.2524 [7]	1.2337 [7]
3 St Optimal	0.4446	1.8086	2.0404	2.2002	2.3415	2.0211	1.2971
4 St Optimal	0.3961	1.3492	1.4214	1.5969	1.7395	1.4877	1.1740
5 St Optimal	0.3711	1.2515	1.3205	1.4550	1.6551	1.4454	1.0912

Note that each optimal solution with just four stations outperforms the benchmark solutions, which include six to eight stations. Thus by carefully analyzing the dynamic measurement geometry, optimal solutions can be found with relatively simple tracking schedules.

8.4 Optimal PDOP Tracking Schedules: Lunar Orbit

Table 8.2 below records the optimal PDOP results found by the genetic algorithm for the OD subsegments in lunar orbit. The Benchmark schedule consists of one station per OD subsegment that produces the best PDOP results.

Table 8.2: Optimal PDOP Schedules: LLO

OD Subsegment:	LLO.1	LLO.2	LLO.3	LLO.4	LLO.5	LL0.6
Benchmark PDOP:	0.3855	0.4649	0.9236	0.4824	0.5131	0.5346
Stations:	KRU1	DSS17	DSS17	OKN2	D32	KRU1
Optimal PDOP:	0.1248	0.2367	0.3796	0.4029	0.3378	0.1870
Stations:	HBK26	KRU1	KRU1	OKN2	D32	HBK26
	DSS17	DSS17	DSS17	D32	OKN2	GHY6
Swap Times [hrs]:	1.4	1.9	1.1	3.1	2.5	2

Note that the dynamics are well defined in lunar orbit, resulting in consistently low PDOP values. Improvement from one station to two stations can decrease PDOP by up to 68%. The smallest improvement occurs in LLO.4, where OKN2 is the only visible station for most of the segment.

8.5 PDOP Results Analysis

Some key patterns occur in the PDOP minimization results. First, as previously discussed, there is a strong emphasis of swapping between stations that vary significantly in latitude. Swapping between GHY6 in England and HBK26 in South Africa provides a large change in latitude, improving measurement geometry. Another powerful change in the measurement geometry comes from swapping between stations that vary in longitude. Swapping between KRU1 in South Guiana and OKN2 in Japan represents swapping between stations that are on opposite sides of the Earth. These two patterns can be used as basic rules of thumb for PDOP optimization. However, some OD segments did not exhibit these patterns, indicating the importance of running the optimization tool.

For all results across cislunar space, the optimal schedules with four stations outperform the Benchmark with six to eight stations. Thus the conclusion is reached that simply adding many stations to an OD segment is not as powerful as carefully analyzing the dynamic measurement geometry.

CHAPTER 9

NEAR-CONTINUOUS NAV-DOLLARS: OPTIMAL TRACKING SCHEDULES

With the optimization of tracking schedules with respect to PDOP complete, analysis regarding station selection and the dynamic measurement geometry is fulfilled in this research. However, reviewing the PDOP values in Table 8.1 indicate that the worst PDOP is only 2.3415 across all OD segments. For a conservative range noise value of $100m$, this tracking schedule would yield a RSS of the position estimation errors of $234m$. Furthermore, it is likely that many combinations of stations producing continuous tracking schedules produce an acceptable PDOP.

This chapter presents the analysis done to find continuous tracking schedules that produce acceptable PDOP values while also reducing operational costs. The metric of Nav-Dollars is introduced and implemented in a genetic algorithm to produce optimal, near-continuous Nav-Dollar tracking schedules. Thus while many continuous tracking schedules produce acceptable PDOP values, an optimal Nav-Dollar schedule has an acceptable PDOP with low operational costs.

9.1 Nav-Dollars and Operational Costs

Nav-Dollars comes from a combination of estimation performance and operational costs. This section outlines how operational costs are defined, how Nav-Dollars are derived, and how near-continuous tracking schedules are implemented to minimize Nav-Dollars.

The operational cost of a station is an estimate of how much the station costs Intuitive Machines to contract and operate during measurement generation. Each ground station is assigned a weighted dollar value, selected from 1, 2, and 2.5, which have been provided by Intuitive Machines [24]. The operational cost for a station is calculated by multiplying the station's operation time by its weighted dollar value. Thus, measurements taken from a station with operational weight of 2 cost twice as much as measurements taken during the same interval from a station with an operational weight of 1.

With each station assigned different weights, the total operational cost of a tracking schedules is calculated by summing the operational cost of each station. The results shown are in units of dollar, but should not be treated as real dollar estimates. Operational costs provide insight into whether an additional station is worth the PDOP improvement. The best case scenario is a tracking schedule that minimizes both PDOP and operational costs. However, the more common scenario is an additional station decreases PDOP and increases operational costs. To analyze the trade off between PDOP and operational costs, the two values are multiplied together to provide a combined metric, referred to as Nav-Dollars.

The Nav-Dollar metric comes from maximizing the information per dollar obtained through a tracking schedule. Optimization traditionally attempts to minimize an objective function, so the inverse of information per dollar is minimized. The dollars per information is calculated by dividing the operational cost by the information obtained from a tracking schedule. Since PDOP is derived from the inverse of the information matrix, minimizing the product of PDOP and operational costs, referred to as Nav-Dollars, is equivalent to maximizing position information per dollar. Furthermore, since PDOP is unitless, Nav-Dollars has a unit of dollars. Nav-Dollars can be viewed as a navigation weighted operational cost.

9.2 Nav-Dollar Implementation

The optimization object for minimizing Nav-Dollars is the same as minimizing PDOP, consisting of station parameters and swap time parameters.

$$\boldsymbol{s} = \begin{bmatrix} N_1 & N_2 & \cdots & N_n & t_{1:2} & t_{2:3} & \cdots & t_{(n-1):n} \end{bmatrix}^T \tag{9.1}$$

A crucial element of Nav-Dollars minimization is that significant state information can be obtained from very few measurements. Initial attempts to minimize Nav-Dollars produced tracking schedules that took measurements for less than 10% of the OD segment. Essentially, Nav-Dollars are minimized by decreasing either operational costs or the final PDOP, and decreasing the operational costs is far easier to do by taking fewer measurements.

While the non-continuous tracking problem is interesting, and is addressed in the next chapter, Intuitive Machines requires continuous tracking for their early lunar missions. Furthermore, the goal of implementing Nav-Dollars in the first place is to determine continuous tracking schedules that produce near-optimal PDOP values for smaller operational costs. Thus, provisions are implemented into the optimization problem to force near-continuous coverage.

While not pursued in depth in this research, the first attempt to force near-continuous tracking was done by placing an upper bound on the PDOP. Any tracking produced by the genetic algorithm that did not produce a PDOP lower than the bound was set to return a large, default Nav-Dollar. As is common with constrained optimization, the optimization algorithm returned minimal Nav-Dollar tracking schedules that produced PDOP values at or near the upper bound. This technique was not further pursued as the upper PDOP bound was set arbitrarily, the resulting optimal schedules varied greatly depending on the upper bound, and often did not produce near-continuous tracking schedules. Furthermore, what is considered an acceptable PDOP for one OD segment may not be for another OD segment.

To effectively produce near-continuous tracking schedules that minimize Nav-Dollars, a lower bound is placed on the percentage of time that measurements are taken. When a tracking schedule does not cover at least the lower bound implemented, the Nav-Dollar is set

at a large, default value. By forcing the algorithm to focus on tracking schedules that take measurements during at least 75% of the OD segment, near-continuous tracking schedules are produced that minimize Nav-Dollars at acceptable PDOP levels.

As was done in the study to minimize PDOP, tracking schedules that minimize Nav-Dollars are found with three, four, and five stations for each OD segment in cislunar space. Two station schedules are found for each OD subsegment in lunar orbit.

9.3 Cislunar Near-Continuous Nav-Dollars Results

Figure 9.1 below depicts the optimal near-continuous Nav-Dollar results found by the genetic algorithm for the OD segment LVS-CM.

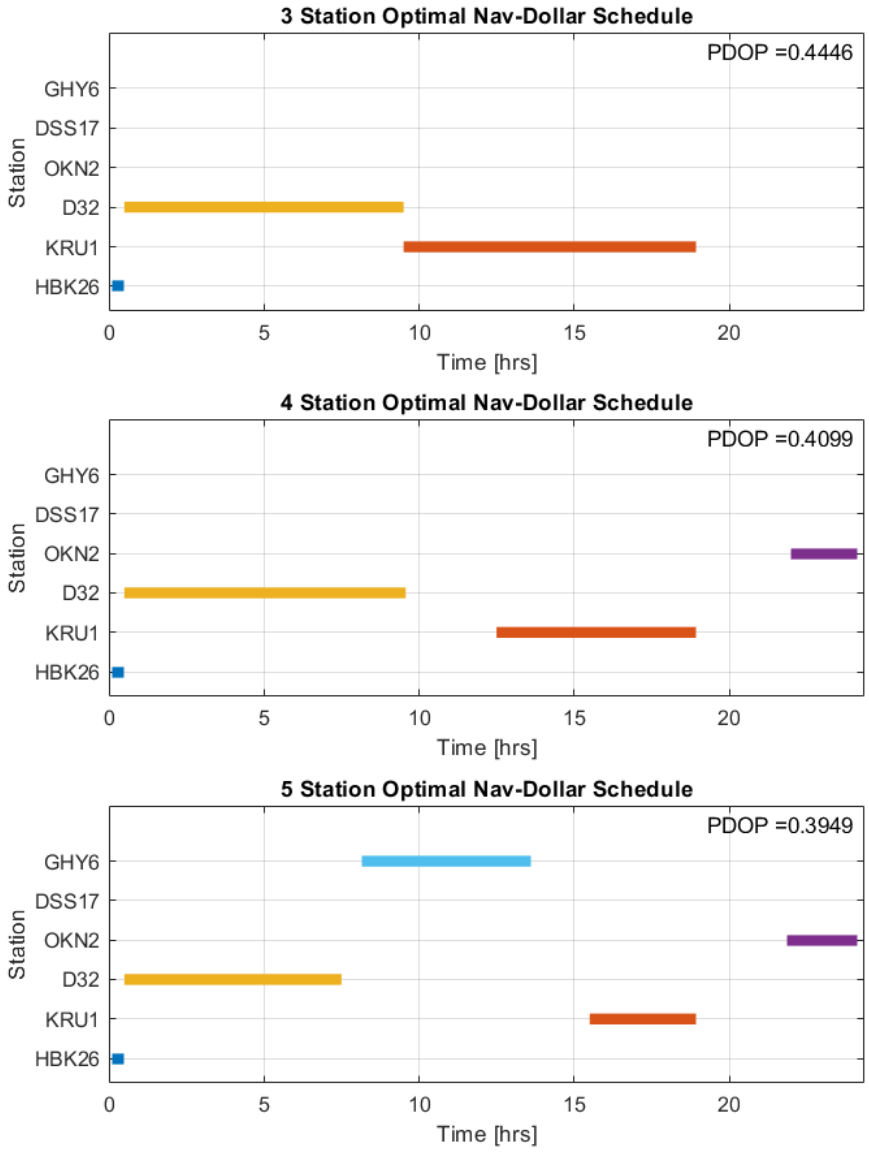

Fig. 9.1: Optimal Nav-Dollar Schedule: LVS-CM

Table 9.1 depicts the PDOP and Nav-Dollars for the optimal Nav-Dollar. For reference, the optimal values from the PDOP optimization are reported in red.

Table 9.1: Optimal PDOP/Nav-Dollar Schedule Comparison: LVS-CM

# Stations:	3	4	5
PDOP:	0.4446 (0.4446)	0.4100 (0.3961)	0.3949 (0.3711)
Nav-Dollars:	5,362 (5,362)	4,502 (5,397)	3,664 (4,258)

Note that by optimizing Nav-Dollars with four and five stations, the Nav-Dollars are less than the optimal PDOP's. But importantly, the PDOP is not increased significantly by optimizing Nav-Dollars. Also note that the tracking schedule that minimizes Nav-Dollars with three stations is the same schedule that minimizes PDOP.

Figure 9.2 below depicts the optimal near-continuous Nav-Dollar results found by the genetic algorithm for the OD subsegment corresponding to the first half of CM-TCM1.

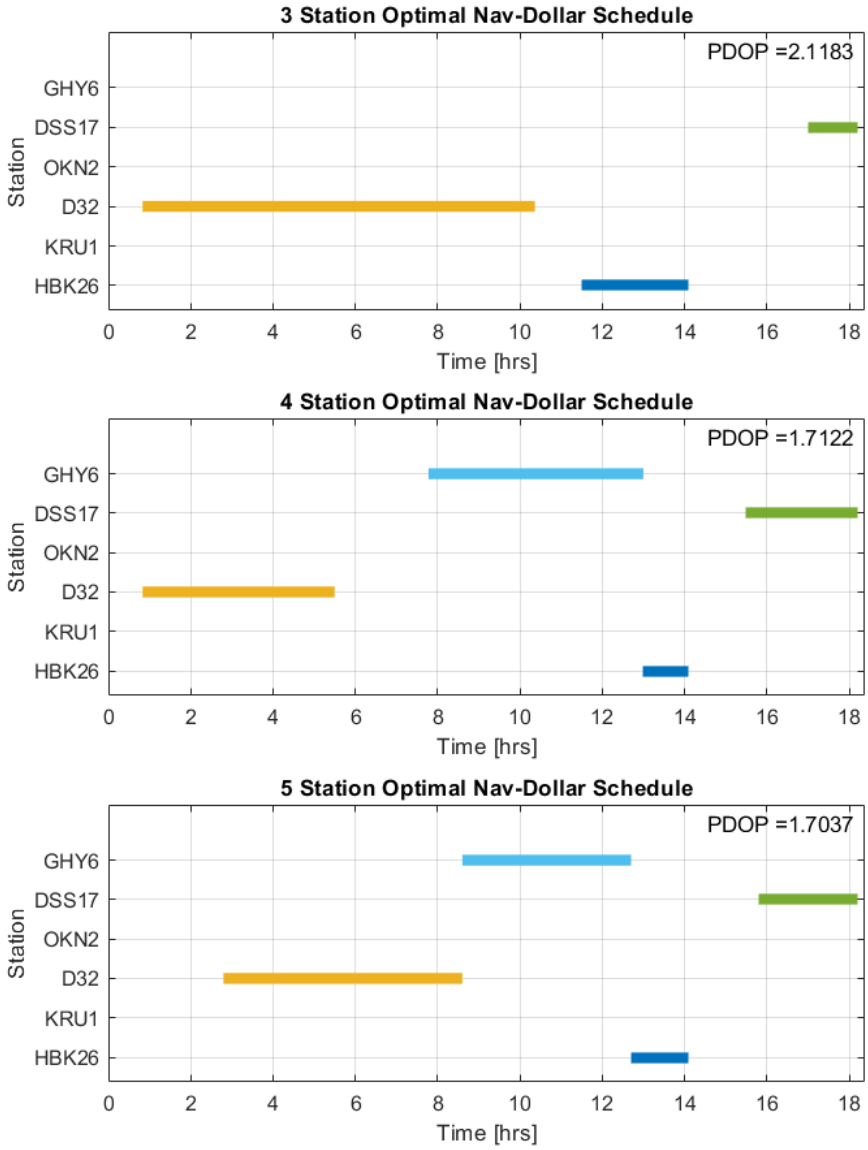

Fig. 9.2: Optimal Nav-Dollar Schedule: CM-TCM1H

Note that the five station schedule does not actually contain five stations. Rather the optimization adds a "ghost station" to the beginning of the OD segment. This allowed the time of D32 to start later, and in turn produce a slightly smaller Nav-Dollar. Table 9.2 shows PDOP and Nav-Dollars found by the optimal schedules. For reference, the optimal

values from the PDOP optimization are reported in red.

Table 9.2: Optimal PDOP/Nav-Dollar Schedule Comparison: CM-TCM1H

# Stations:	3	4	5
PDOP:	2.1183 (1.8086)	1.7122 (1.3492)	1.7037 (1.2515)
Nav-Dollars:	14,665 (17,587)	11,271 (16,391)	11,068 (15,787)

Here note that all optimal Nav-Dollar schedules outperform the Nav-Dollars generated by the optimal PDOP schedules. For this OD subsegment, adding a fifth station to the optimization object only improved Nav-Dollars by altering when the first station begins. While not presented here, adding a sixth station to the optimization object also does not truly add a sixth station, but rather a ghost station.

The question here arises whether the formation of the swap time parameters in the optimization object is appropriate. If the parameters were start and end times, an analysis with four stations could have been produced the same schedule found with five stations in Fig. 9.2.

It is the author's opinion that the current optimization object remains advantageous as it reduces the number of variables from $3N$ to $2N - 1$. Fewer variables consistently improves the run time and convergence consistency of the genetic algorithm. Furthermore with the current configuration the better schedule with four stations is found, just in a roundabout way. Lastly, as Nav-Dollar inherently attempts to reduce the measurement time, start and stop time parameters do not as easily lead to continuous schedules as the swap time parameter does. This OD segment is the only instant in which a ghost station is present.

Figure 9.3 below depicts the optimal near-continuous Nav-Dollar results found by the genetic algorithm for the OD subsegment corresponding to the second half of CM-TCM1.

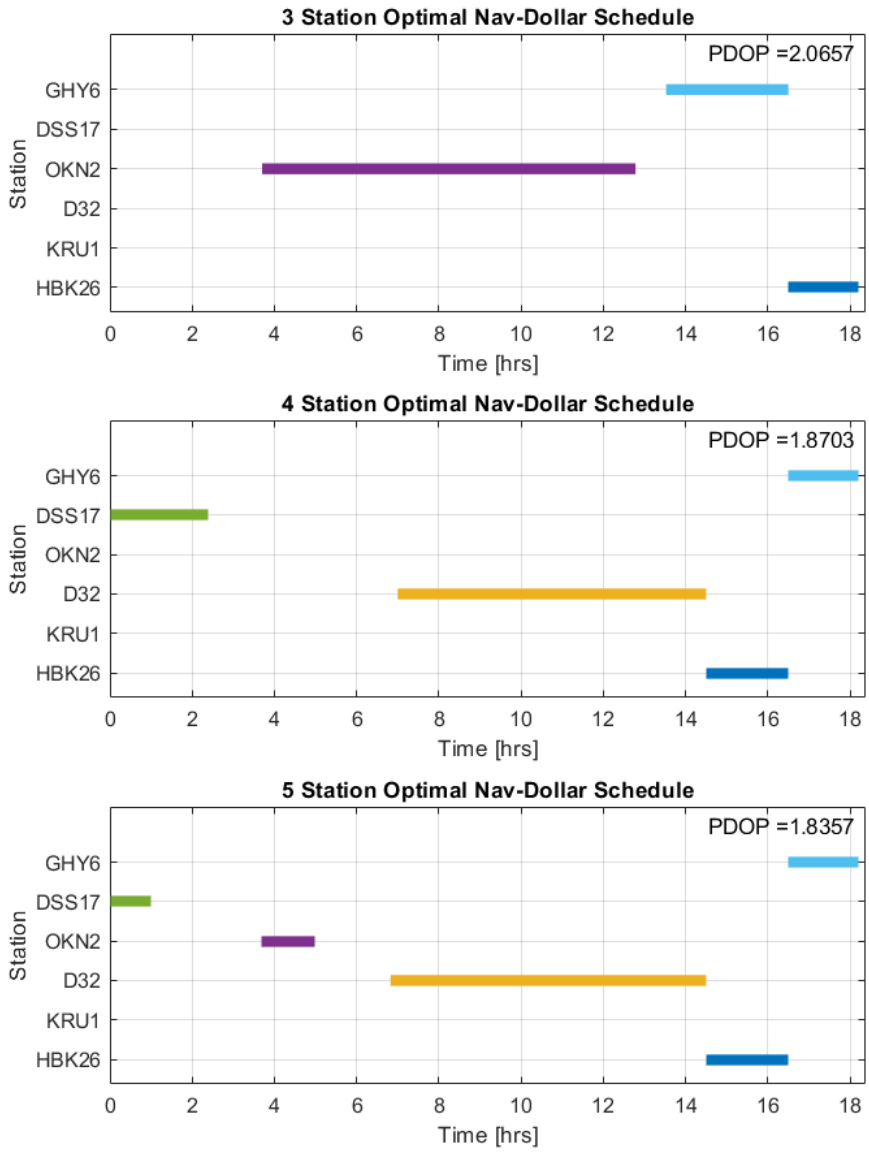

Fig. 9.3: Optimal Nav-Dollar Schedule: TCM1H-TCM1

Table 9.3 records the Nav-Dollar comparisons:

Table 9.3: Optimal PDOP/Nav-Dollar Schedule Comparison: TCM1H-TCM1

# Stations:	3	4	5
PDOP:	2.0657 (1.8086)	1.8703 (1.3492)	1.8357 (1.2515)
Nav-Dollars:	19,099 (19,306)	12,761 (16,225)	12,330 (14,303)

Here note that all optimal Nav-Dollar schedules outperform the Nav-Dollars generated by the optimal PDOP schedules. For this OD subsegment, adding a fifth station does not significantly reduce Nav-Dollars. Interestingly, the only difference between the optimal solutions found by minimizing PDOP and Nav-Dollars with three stations is the time that the stations change.

Figure 9.4 below depicts the optimal near-continuous Nav-Dollar results found by the genetic algorithm for the OD subsegment corresponding to the first half of TCM1-TCM2.

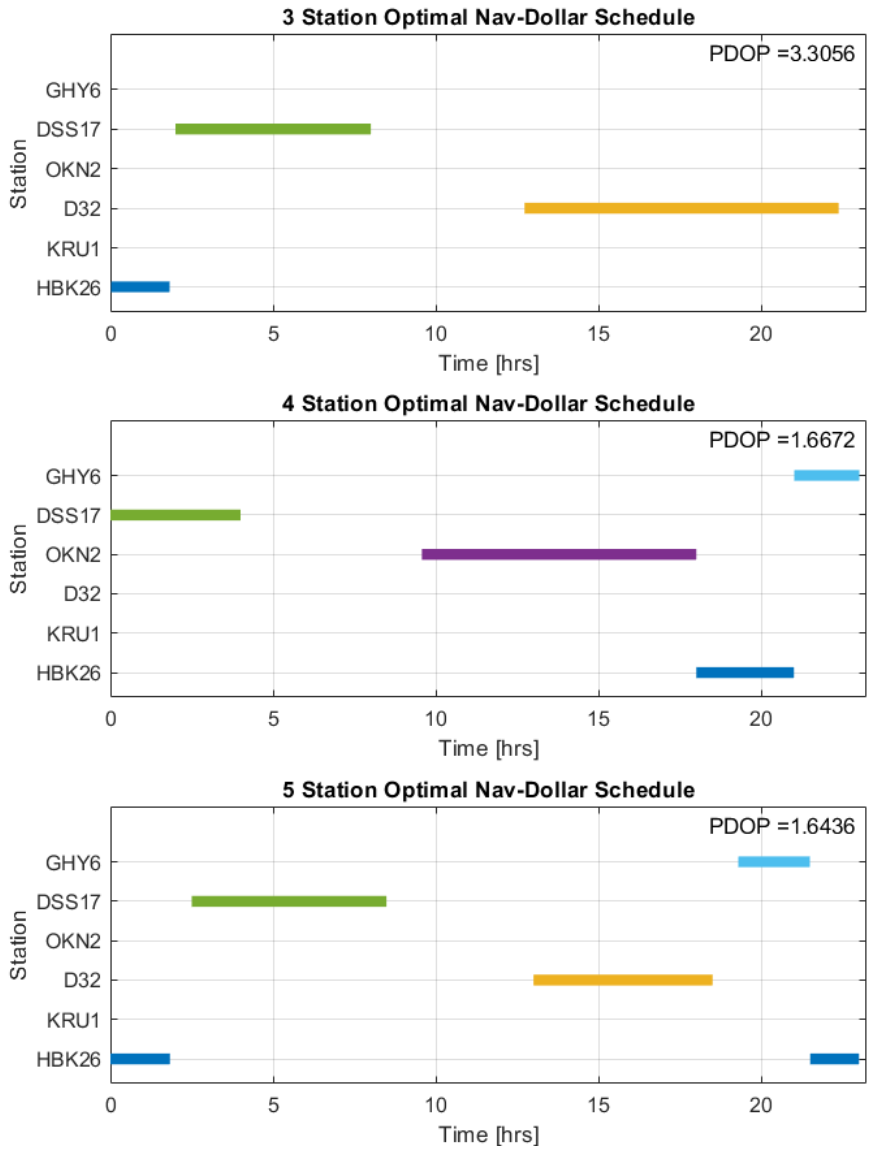

Fig. 9.4: Optimal Nav-Dollar Schedule: TCM1-TCM2H

Table 9.3 records the Nav-Dollar comparisons:

Table 9.4: Optimal PDOP/Nav-Dollar Schedule Comparison: TCM1-TCM2H

# Stations:	3	4	5
PDOP:	3.3056 (2.5623)	1.6672 (1.5696)	1.6436 (1.4550)
Nav-Dollars:	30,730 (44,215)	20,254 (25,051)	16,755 (22,951)

Here note that all optimal Nav-Dollar schedules outperform the Nav-Dollars generated by the optimal PDOP schedules. Note that while the PDOP did not change significantly between the four and five station optimal schedules, the Nav-Dollars did significantly.

Figure 9.5 below depicts the optimal near-continuous Nav-Dollar results found by the genetic algorithm for the OD subsegment corresponding to the second half of TCM1-TCM2.

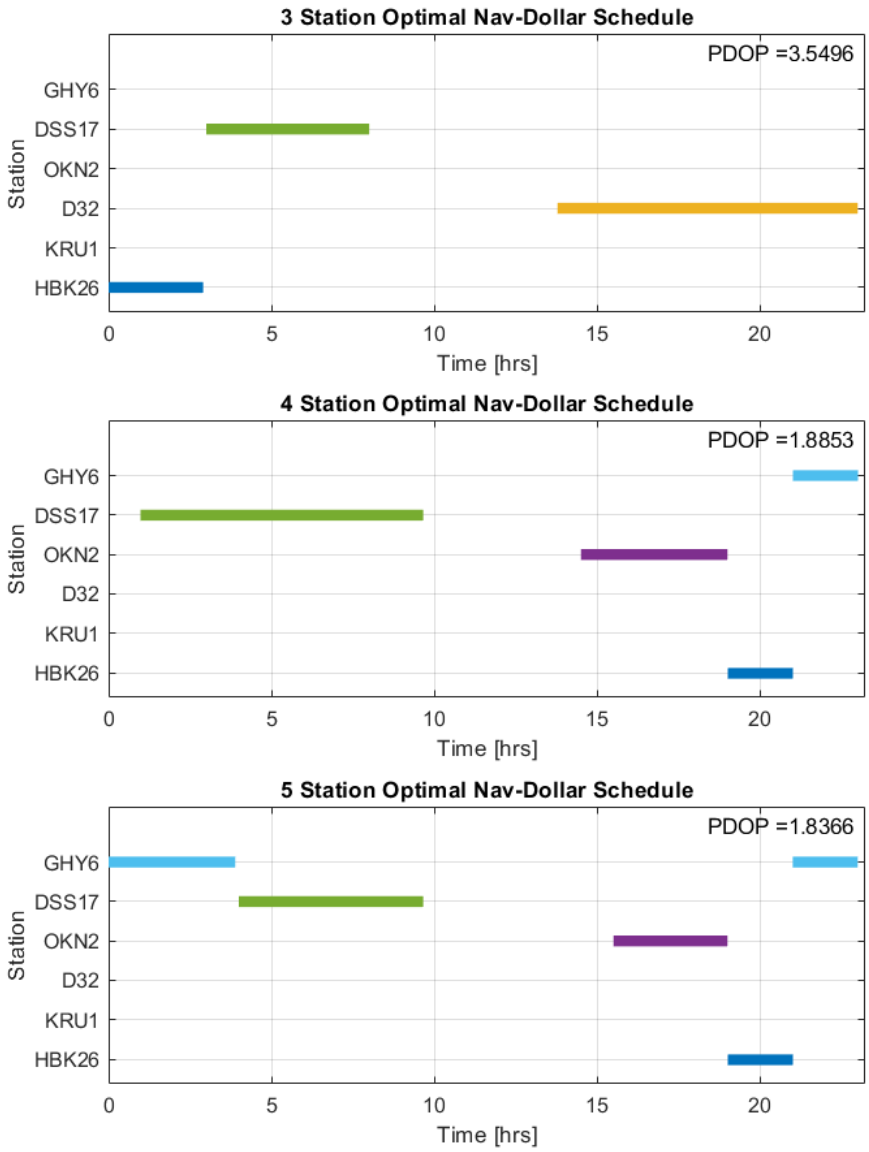

Fig. 9.5: Optimal Nav-Dollar Schedule: TCM2H-TCM2

Table 9.5 records the Nav-Dollar comparisons:

Table 9.5: Optimal PDOP/Nav-Dollar Schedule Comparison: TCM2H-TCM2

# Stations:	3	4	5
PDOP:	3.5496 (1.8086)	1.8853 (1.3492)	1.8366 (1.2515)
Nav-Dollars:	34,316 (46,421)	22,733 (28,082)	19,577 (26,774)

Here note that all optimal Nav-Dollar schedules outperform the Nav-Dollars generated by the optimal PDOP schedules. For this OD subsegment, adding a fifth station does not significantly reduce the PDOP, but does impact Nav-Dollars.

Figure 9.6 below depicts the optimal near-continuous Nav-Dollar results found by the genetic algorithm for the OD segment corresponding to TCM2-TCM3.

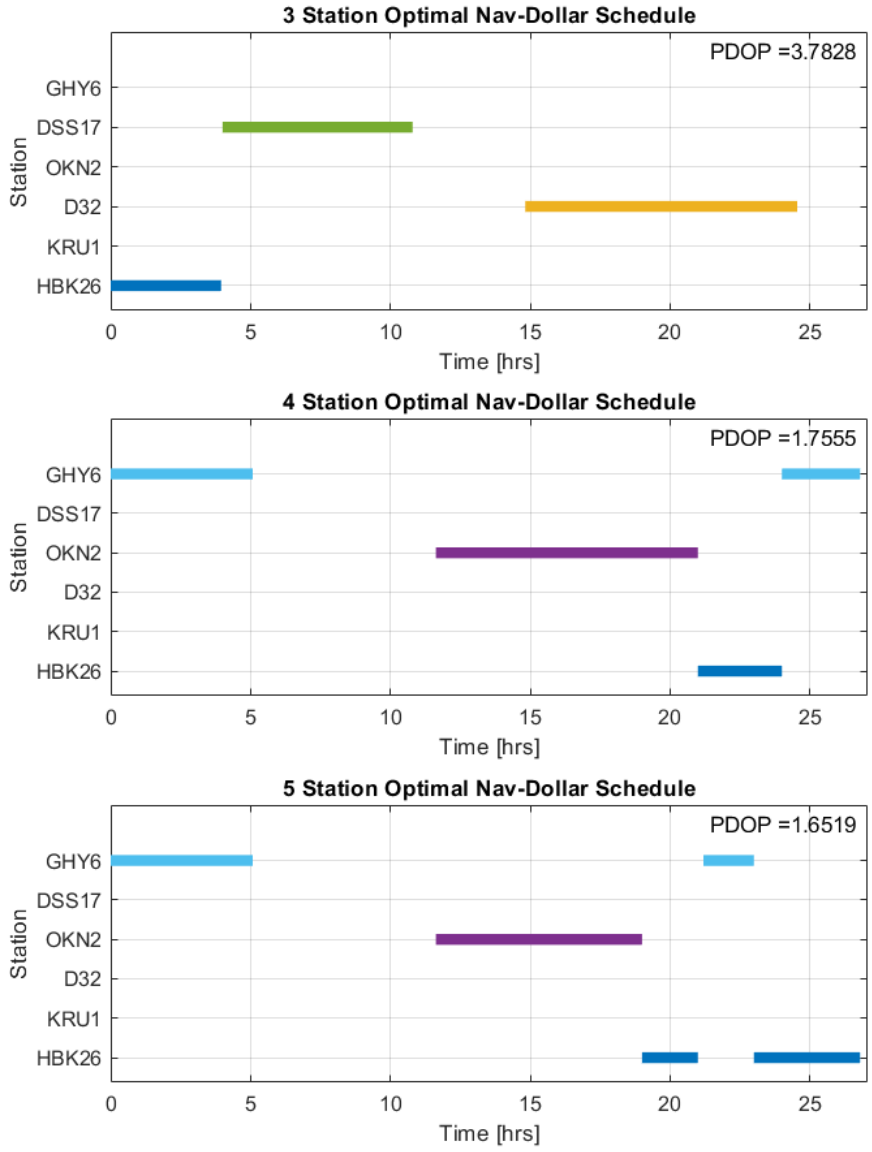

Fig. 9.6: Optimal Nav-Dollar Schedule: TCM2-TCM3

Table 9.6 records the Nav-Dollar comparisons:

Table 9.6: Optimal PDOP/Nav-Dollar Schedule Comparison: TCM2-TCM3

# Stations:	3	4	5
PDOP:	3.7828 (2.7710)	1.7555 (1.4877)	1.6519 (1.4454)
Nav-Dollars:	44,386 (57,542)	21,406 (29,977)	19,574 (28,806)

Here note that all optimal Nav-Dollar schedules outperform the Nav-Dollars generated by the optimal PDOP schedules. Both PDOP and Nav-Dollars decrease notably with the inclusion of additional stations.

Figure 9.7 below depicts the optimal near-continuous Nav-Dollar results found by the genetic algorithm for the OD segment corresponding to TCM3-LOI. Generally the position errors are very small on lunar approach, so the minimization occurs approximately two hours before LOI.

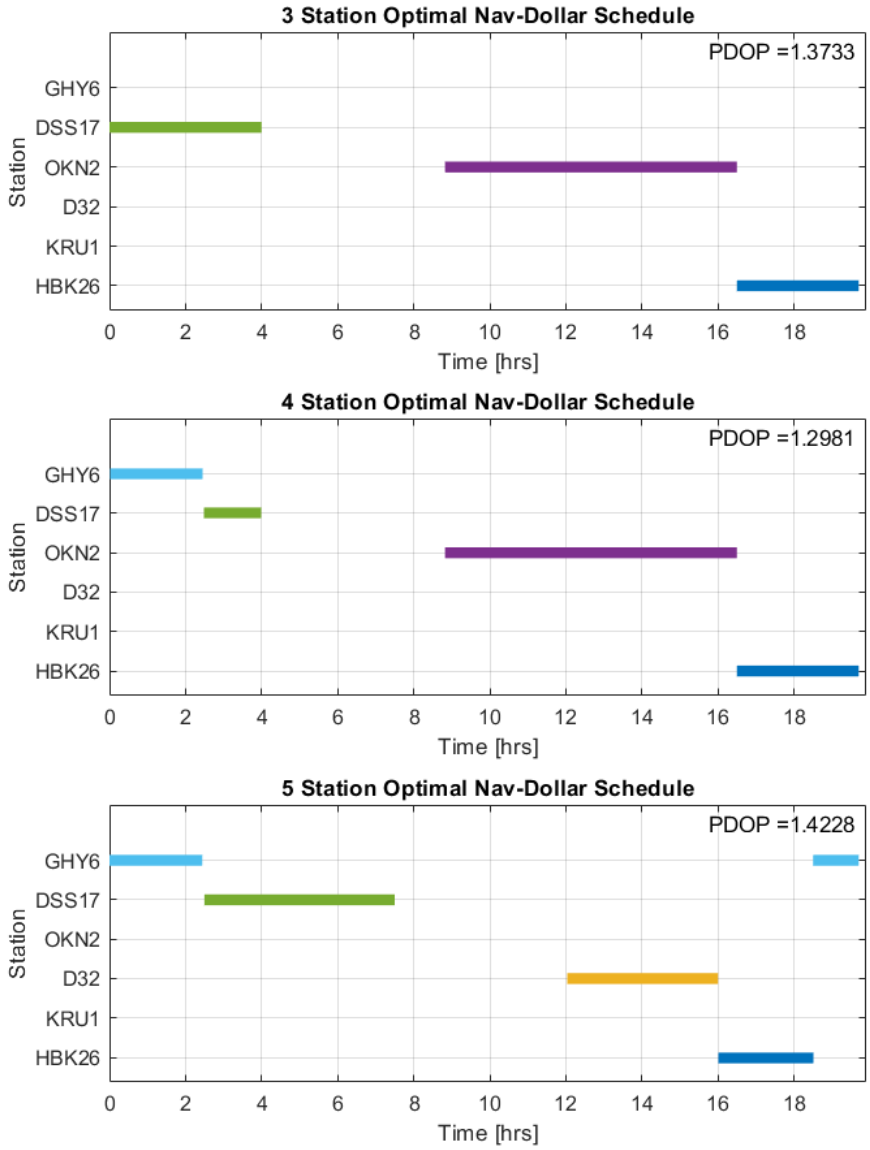

Fig. 9.7: Optimal Nav-Dollar Schedule: TCM3-LOI

Table 9.7 records the Nav-Dollar comparisons:

Table 9.7: Optimal PDOP/Nav-Dollar Schedule Comparison: TCM3-LOI

# Stations:	3	4	5
PDOP:	1.3733 (1.8086)	1.2981 (1.3492)	1.4228 (1.2515)
Nav-Dollars:	15,447 (18,638)	13,477 (17,169)	11,906 (15,469)

Here note that all optimal Nav-Dollar schedules outperform the Nav-Dollars generated by the optimal PDOP schedules. Interestingly, adding a fifth station does reduce Nav-Dollars, but is the only instance of doing so by also increasing the PDOP.

9.4 Lunar Orbit Near-Continuous Nav-Dollars Results

Due to lunar occultation, the solution space covering 75% of the OD subsegments is very limited. Furthermore, it is common for OD subsegments in lunar orbit to only have one to two stations to select. Table 9.8 depicts the Nav-Dollars from the optimal PDOP study compared to the Nav-Dollar optimization.

Table 9.8: Optimal PDOP/Nav-Dollar Schedule Nav-Dollar Comparison: LLO

OD Subsegment:	LLO.1	LLO.2	LLO.3	LLO.4	LLO.5	LL0.6
Optimal PDOP:						
Nav-Dollars:	365	673	912	824	468	343
Stations:	HBK26	KRU1	KRU1	OKN2	D32	HBK26
	DSS17	DSS17	DSS17	D32	OKN2	GHY6
Swap Times [hrs]:	1.4	1.9	1.1	3.1	2.5	2
Optimal Nav-Dollars:						
Nav-Dollars:	301	664	912	824	468	312
Stations:	HBK26	KRU1	KRU1	OKN2	D32	HBK26
	DSS17	DSS17	DSS17	D32	OKN2	GHY6
Swap Times [hrs]:	0.5	1.5	1.1	3.1	2.5	1.5

Note the only differences are in LLO.1, LLO.2, and LLO.6, where the swap times differ in order to spend less time on the more expensive stations. OD subsegments LLO.3, LLO.4, and LLO.5 are exactly the same as the optimal PDOP schedules. Because of the minimal changes in Nav-Dollars and the schedule, it is safe to assume that optimizing PDOP alone is sufficient for reducing Nav-Dollars in lunar orbit. Furthermore, lunar orbit is a crucial mission segment, and optimizing PDOP may be the wiser method.

9.5 Optimal PDOP and Nav-Dollar Comparison and Discussion

Some clear patterns appear through minimizing near-continuous Nav-Dollars that are seen by comparing tracking schedules with the optimal PDOP results. Figure 9.8 shows the optimal PDOP and optimal Nav-Dollar schedule for the first half of CM-TCM1 with four stations:

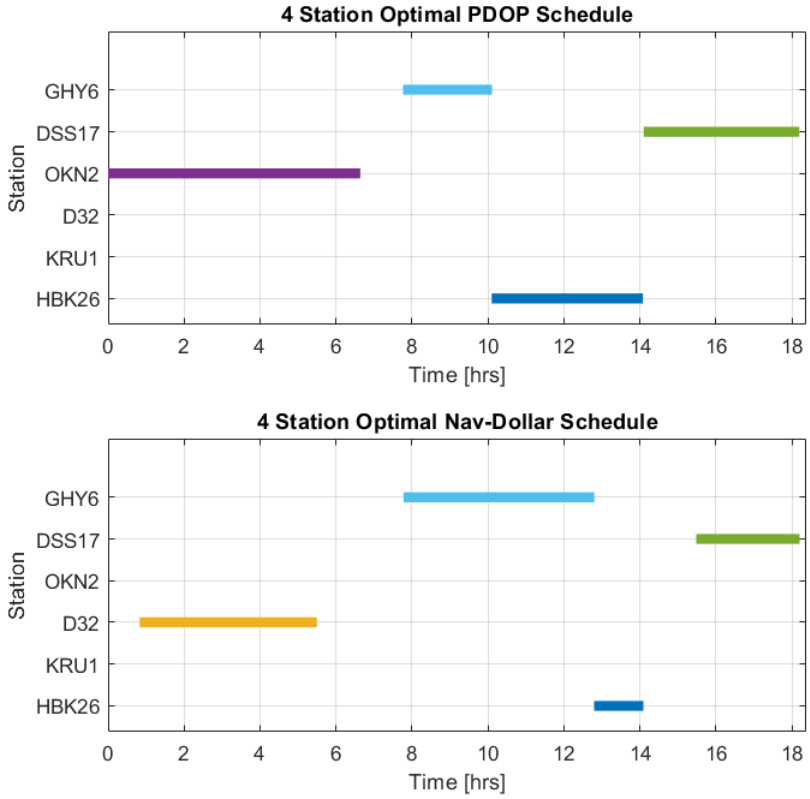

Fig. 9.8: Optimal PDOP and Nav-Dollar Comparison: CM-TCM1H

Note that to minimize PDOP, the stations used are OKN2, GHY6, HBK26, and DSS17, sequentially. To minimize Nav-Dollars, the stations used are D32, GHY6, HBK26, and DSS17, sequentially. The order of the last three stations is the same, as the geometry obtained from those three stations helps reduce PDOP at the final time. Station D32 replaces OKN2 as D32 has a weight of 1 and OKN2 has a weight of 2. GHY6 also has a weight of 1, and is used for more time in the Nav-Dollar minimization over HBK26, which has a weight of 2.5.

Another great example is seen by comparing the schedules for the first half of TCM1-TCM2. Figure 9.9 shows the four station optimal schedules:

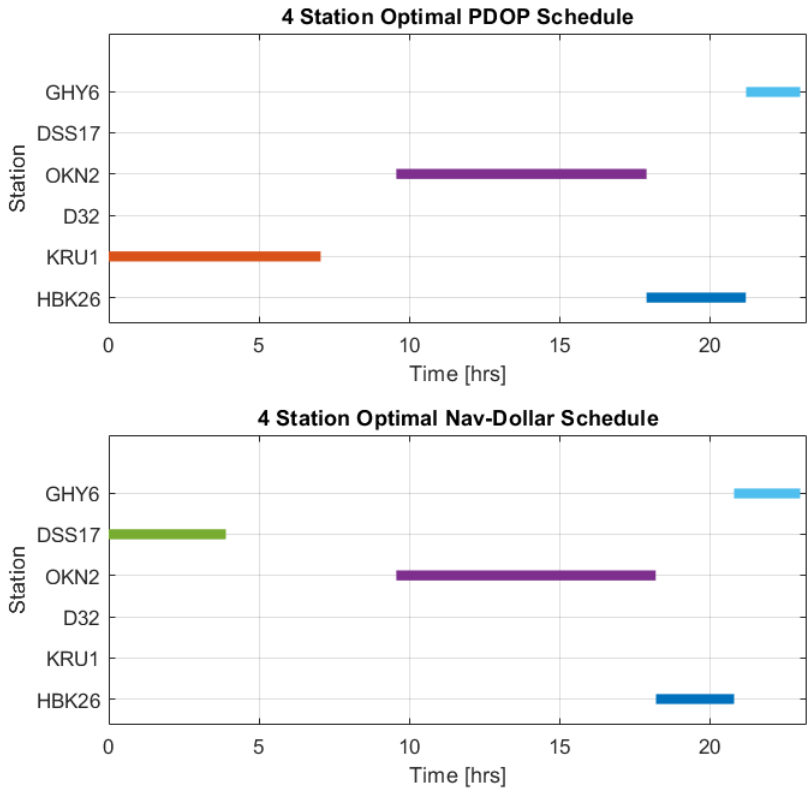

Fig. 9.9: Optimal PDOP and Nav-Dollar Comparison: TCM1-TCM2H

Note the last 12 hours of each OD segment are essentially the same, but the beginning is different. To reduce operational costs, the Nav-Dollar optimal solution replaces KRU1 in South Guiana with DSS17 in Kentucky. Doing so only increases the PDOP from 1.5696 to 1.6672, but decreases Nav-Dollars from 25,051 to 20,254. Interestingly, KRU1 is never used after OD1 in the Nav-Dollar optimization, as DSS17 is almost always visible at the same times for a lower operational cost.

Future work may be done to study how optimal Nav-Dollar schedules change as the lower bound of measurement coverage is altered. The lower bound here is set at 75%, and is generally seen as conservatively low for near-continuous coverage.

CHAPTER 10

NON-CONTINUOUS NAV-DOLLARS: OPTIMAL TRACKING SCHEDULES

As the nature of minimizing Nav-Dollars emphasizes taking fewer measurements, it is appropriate to study how Nav-Dollars are minimized with non-continuous tracking. While non-continuous tracking is not desired for the IM-1 mission, Intuitive Machines has expressed strong interest in low measurement OD segments for circuitous lunar missions and future missions.

This chapter outlines how a non-continuous optimization object is formulated and implemented in a genetic algorithm. Results are shown for each OD segment and subsegment in cislunar space and in lunar orbit. Trends are discussed and the results are compared to the results obtained from near-continuous Nav-Dollar schedules.

10.1 Non-Continuous Optimization Object

In order to create non-continuous tracking schedules, new time metrics are analyzed beside swap time parameters. The optimization object that allows the greatest flexibility includes start and end time parameters. For a schedule with two stations, the optimization object is:

$$\boldsymbol{s} = \begin{bmatrix} N_1 & N_2 & t_{1,s} & t_{1,e} & t_{2,s} & t_{2,e} \end{bmatrix} \tag{10.1}$$

where station N_1 begins taking stations at time $t_{1,s}$ and ends taking measurements at time $t_{1,e}$, and station N_2 begins taking measurements at Where station N_1 begins taking stations at time $t_{2,s}$ and ends taking measurements at time $t_{2,e}$. This pattern is generalized to included any number of stations:

$$\boldsymbol{s} = \begin{bmatrix} N_1 & N_2 & \cdots & N_n & t_{1,s} & t_{1,e} & t_{2,s} & t_{2,e} & \cdots & t_{n,s} & t_{n,e} \end{bmatrix} \tag{10.2}$$

Note that the size of this optimization object is $3N$, where N is the number of stations.

In order to ensure that the stations do not overlap when taking measurements, linear constraints are implemented. The linear constrains when $N = 2$ is expressed as:

$$t_{1,s} + t_b \leq t_{1,e} \tag{10.3}$$

$$t_{2,s} + t_b \leq t_{2,e} \tag{10.4}$$

$$t_{1,e} \leq t_{2,s} \tag{10.5}$$

Or in matrix/vector form:

$$\begin{bmatrix} 0 & 0 & 1 & -1 & 0 & 0 \\ 0 & 0 & 0 & 1 & -1 & 0 \\ 0 & 0 & 0 & 0 & 1 & -1 \end{bmatrix} \begin{bmatrix} N_1 \\ N_2 \\ t_{1,s} \\ t_{1,e} \\ t_{2,s} \\ t_{2,e} \end{bmatrix} \leq \begin{bmatrix} -t_b \\ 0 \\ -t_b \end{bmatrix} \tag{10.6}$$

The first two indicate that a station, when used, must have start and end times that are at least time t_b apart. As previously discussed, a scheduled station must realistically be used for some minimum time or it cannot be scheduled at all. The last constraint ensures that the second station does not begin until after the first station. Thus this optimization object allows for flexible, non-continuous tracking schedules to be created and found by the genetic algorithm.

However, through optimizing several OD segments a clear pattern emerged that once again indicated Nav-Dollars are minimized by taking as few measurements as possible. When the linear constraints were implemented, the optimal schedules produced stations that took as few measurements as possible according to:

$$t_{n,s} + t_b = t_{n,e} \tag{10.7}$$

As this pattern was consistent across OD segments, the optimization object for minimizing non-continuous Nav-Dollars is altered to include only the start times:

$$\boldsymbol{s} = \begin{bmatrix} N_1 & N_2 & \cdots & N_n & t_{1,s} & t_{2,s} & \cdots & t_{n,s} \end{bmatrix} \tag{10.8}$$

where measurements are taken from station N starting at time t_s for a set measurement duration t_b. Implementing this new optimization object reduces the number of parameters from $3N$ to $2N$.

10.2 Number of Stations Implemented

As discovered in the previous chapter on near-continuous Nav-Dollars, on occasion adding an additional station does not truly add an additional station, but rather a ghost station. This is done by the genetic algorithm primarily to obtain flexibility with the swap time parameters.

As the non-continuous optimization object is designed to promote non-continuous schedules, if the author and future users intend to produce schedules with N stations, N stations must actually be used. Thus if an optimization object with four stations is implemented, four stations must be in the tracking schedule with no ghost stations. Provisions are taken within the optimization to penalize schedules that produce ghost stations.

Thus adding a station to the optimization object forces more measurement time, increasing operational costs. As is indicated in some OD segments, adding an additional station does not reduce Nav-Dollars. It is crucial to recall that the optimal schedules are optimal given the number of stations. As a truly optimal PDOP schedule is optimal with constant coverage with many stations, a truly optimal Nav-Dollar schedule may include measurements from only two or one station.

As including additional stations often increases Nav-Dollars, optimal schedules in cislunar spaced are analyzed with three and four stations, omitting a study on five stations. All cislunar schedules have a measurement duration of 1 hour. The setup in lunar orbit remains the same with two stations per OD subsegment, but with a half hour measurement duration.

10.3 Cislunar Non-Continuous Results

Figure 10.1 depicts optimal schedules with three and four stations for OD segment LVS-CM:

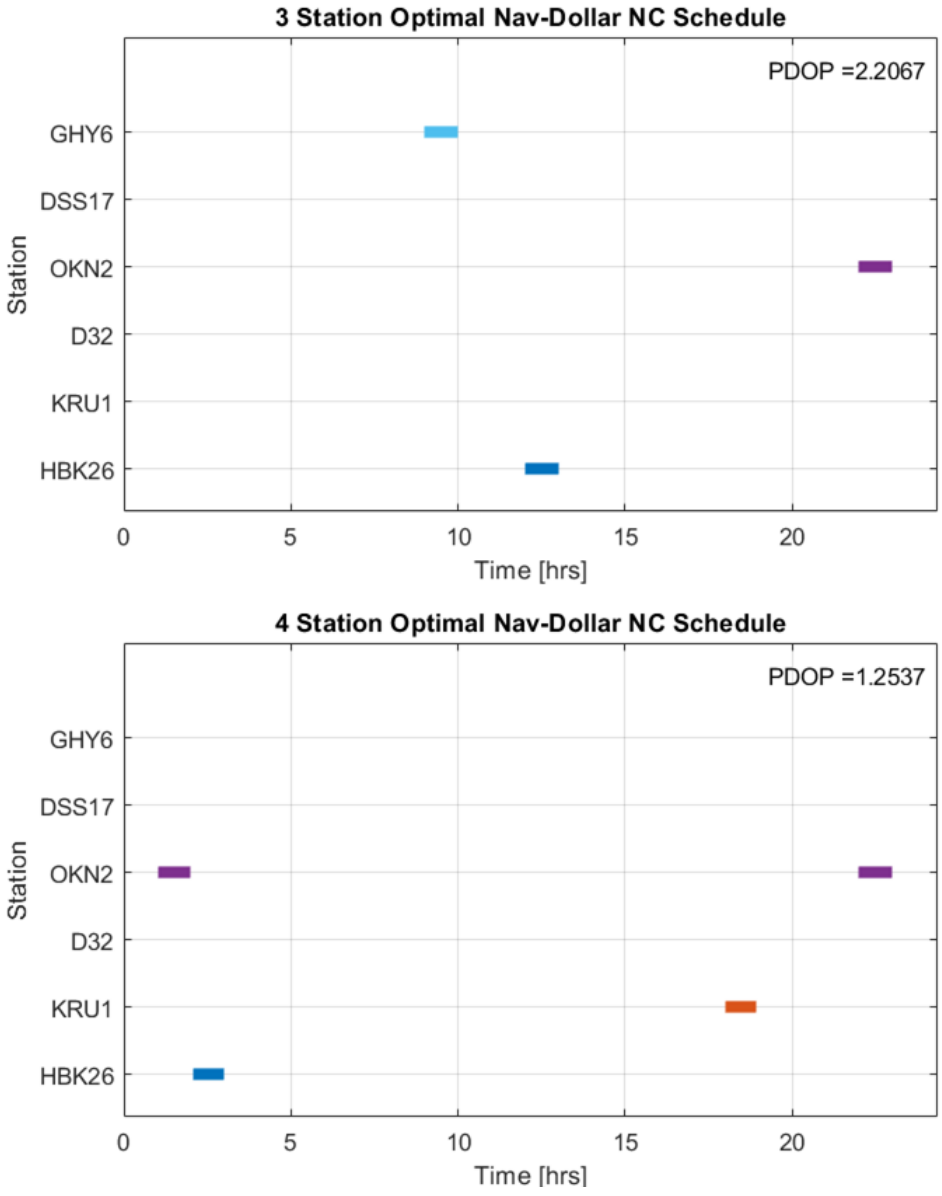

Fig. 10.1: Non-Continuous Nav-Dollars: LVS-CM

No clear pattern is evident in this first portion, but note that while only using three to four hours of tracking, the PDOP is less than 2.5 for each schedule. Table 10.1 shows the Nav-Dollar comparison to the near-continuous Nav-Dollar schedules, shown in blue:

Table 10.1: Nav-Dollar Schedule Comparisons: LVS-CM

# Stations:	3	4
PDOP:	2.2067 (0.4446)	1.2537 (0.4100)
Nav-Dollars:	4,369 (5,362)	3,852 (4,502)

Figure 10.2 depicts optimal schedules with three and four stations for the first half of OD segment CM-TCM1:

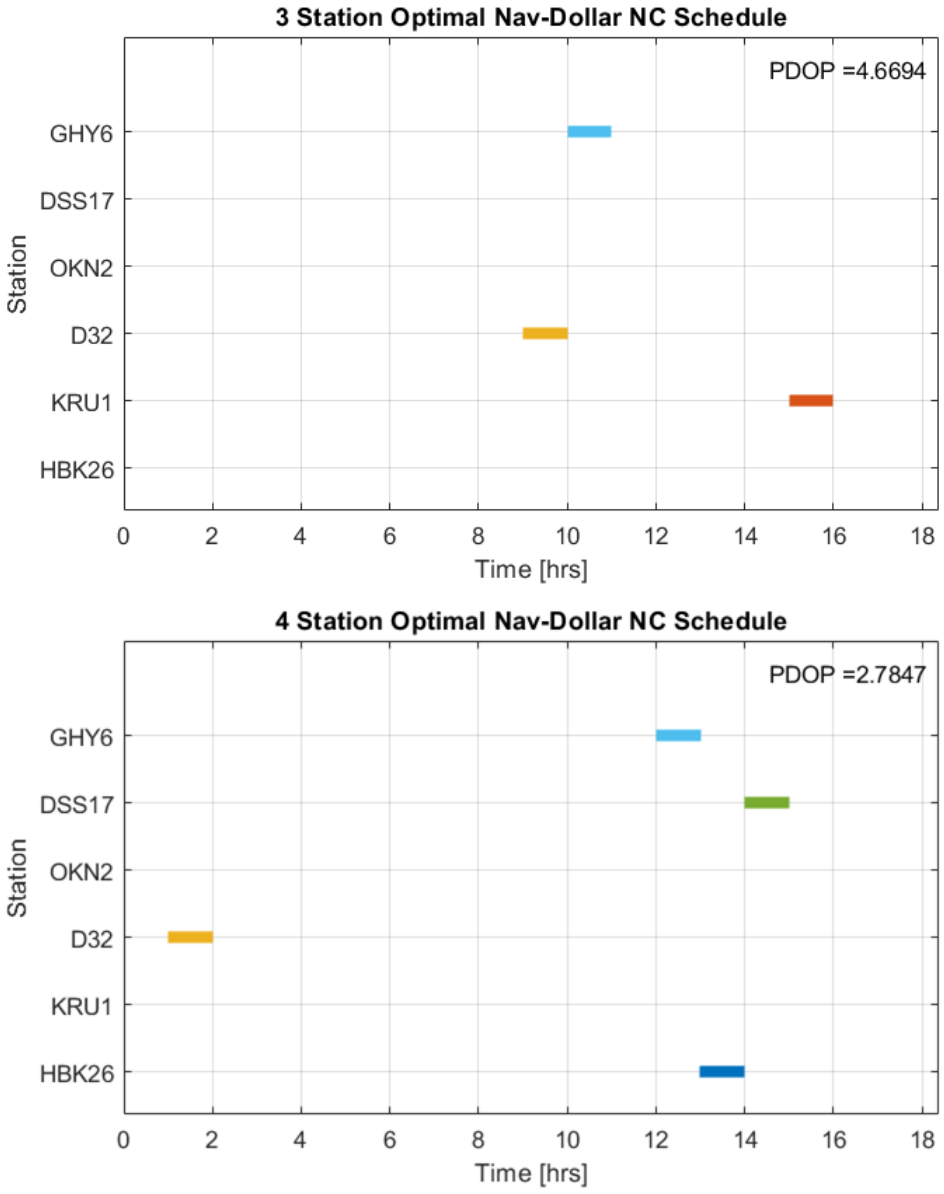

Fig. 10.2: Non-Continuous Nav-Dollars: CM-TCM1H

Here note that with four stations, three are placed near the end of the OD segment in to reduce PDOP at the final time. Table 10.2 shows the Nav-Dollar comparison to the near-continuous Nav-Dollar schedules, shown in blue:

Table 10.2: Nav-Dollar Schedule Comparisons: CM-TCM1H

# Stations:	3	4
PDOP:	4.6694 (0.7060)	2.7847 (0.4100)
Nav-Dollars:	7,564 (14,665)	6,516 (11,207)

Figure 10.3 depicts optimal schedules with three and four stations for the second half of OD segment CM-TCM1:

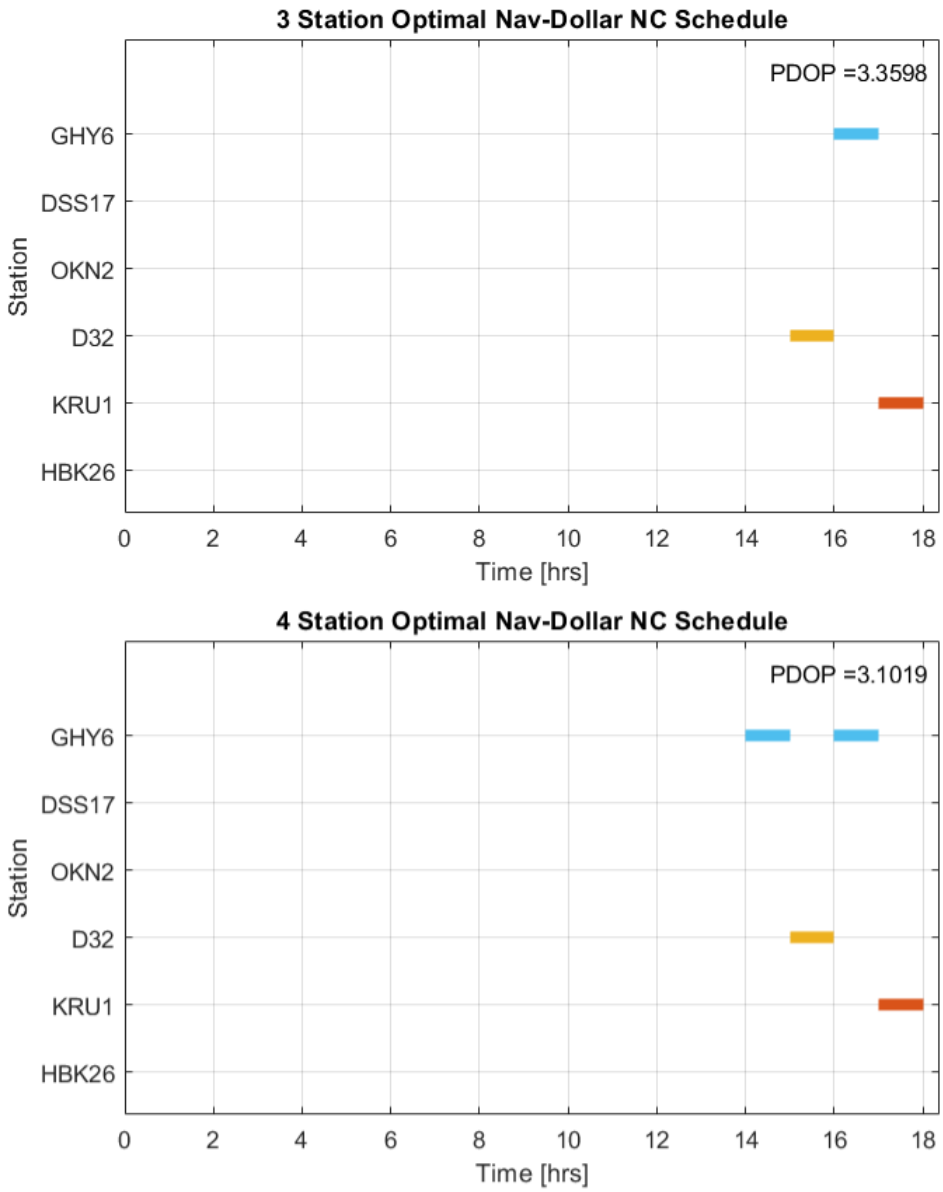

Fig. 10.3: Non-Continuous Nav-Dollars: TCM1H-TCM1

Note that both schedules push the station segments towards the end of the OD segment. Also note how GHY6 is given additional time with four stations, as GHY6 is the farthest north in latitude. Table 10.3 shows the comparison to the near-continuous Nav-Dollar schedules:

Table 10.3: Nav-Dollar Schedule Comparisons: TCM1H-TCM1

# Stations:	3	4
PDOP:	3.3958 (2.0167)	3.1019 (1.8703)
Nav-Dollars:	5,501 (19,099)	5,552 (12,761)

Figure 10.4 depicts optimal schedules with three and four stations for the first half of OD segment TCM1-TCM2:

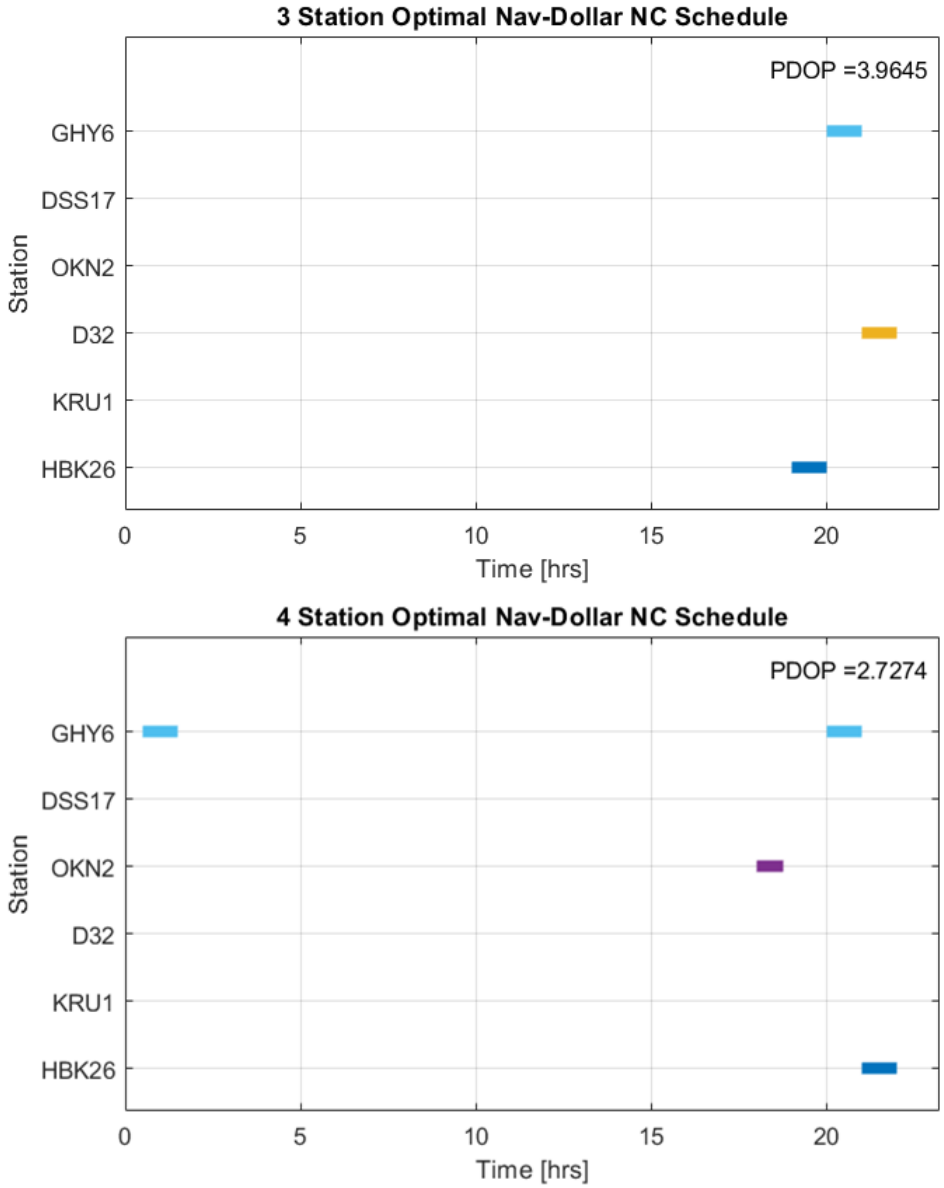

Fig. 10.4: Non-Continuous Nav-Dollars: TCM1-TCM2H

Both schedules push stations toward the end; however, the solution with four stations places a segment at the very beginning, reducing estimation error growth immediately. Table 10.4 shows the Nav-Dollar comparison to the near-continuous Nav-Dollar schedules:

Table 10.4: Nav-Dollar Schedule Comparisons: TCM1-TCM2H

# Stations:	3	4
PDOP:	3.9645 (3.3056)	2.7274 (1.6672)
Nav-Dollars:	6,423 (30,730)	5,934 (20,254)

Figure 10.5 depicts optimal schedules with three and four stations for the second half of OD segment TCM1-TCM2:

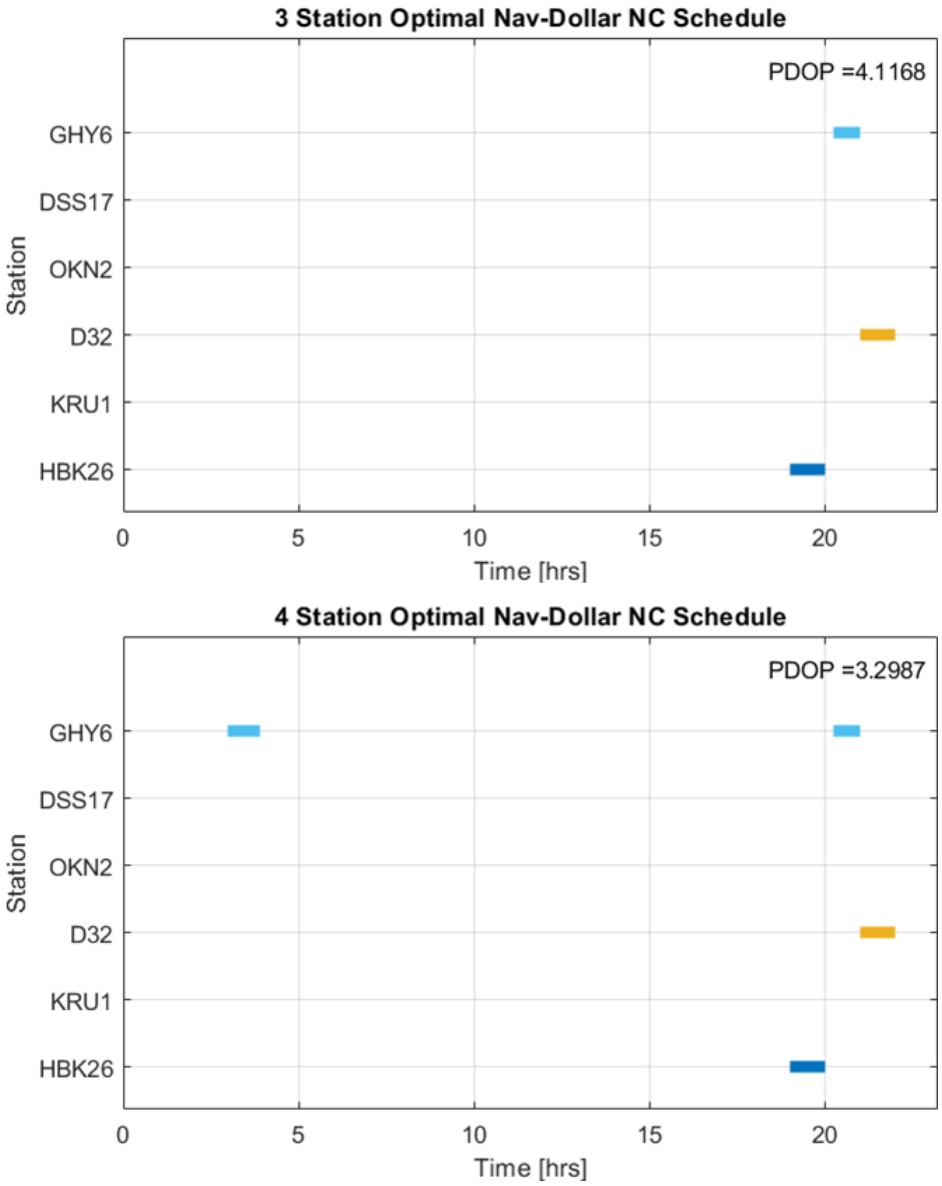

Fig. 10.5: Non-Continuous Nav-Dollars: TCM2H-TCM2

Both schedules push stations toward the end; however, the solution with four stations places a segment at the beginning, reducing estimation error growth immediately. Table 10.5 shows the Nav-Dollar comparison to the near-continuous Nav-Dollar schedules:

Table 10.5: Nav-Dollar Schedule Comparisons: TCM2H-TCM2

# Stations:	3	4
PDOP:	4.1168 (3.3496)	3.2987 (1.8853)
Nav-Dollars:	6,302 (34,316)	6,105 (22,733)

Figure 10.6 depicts optimal schedules with three and four stations for the OD segment TCM2-TCM3:

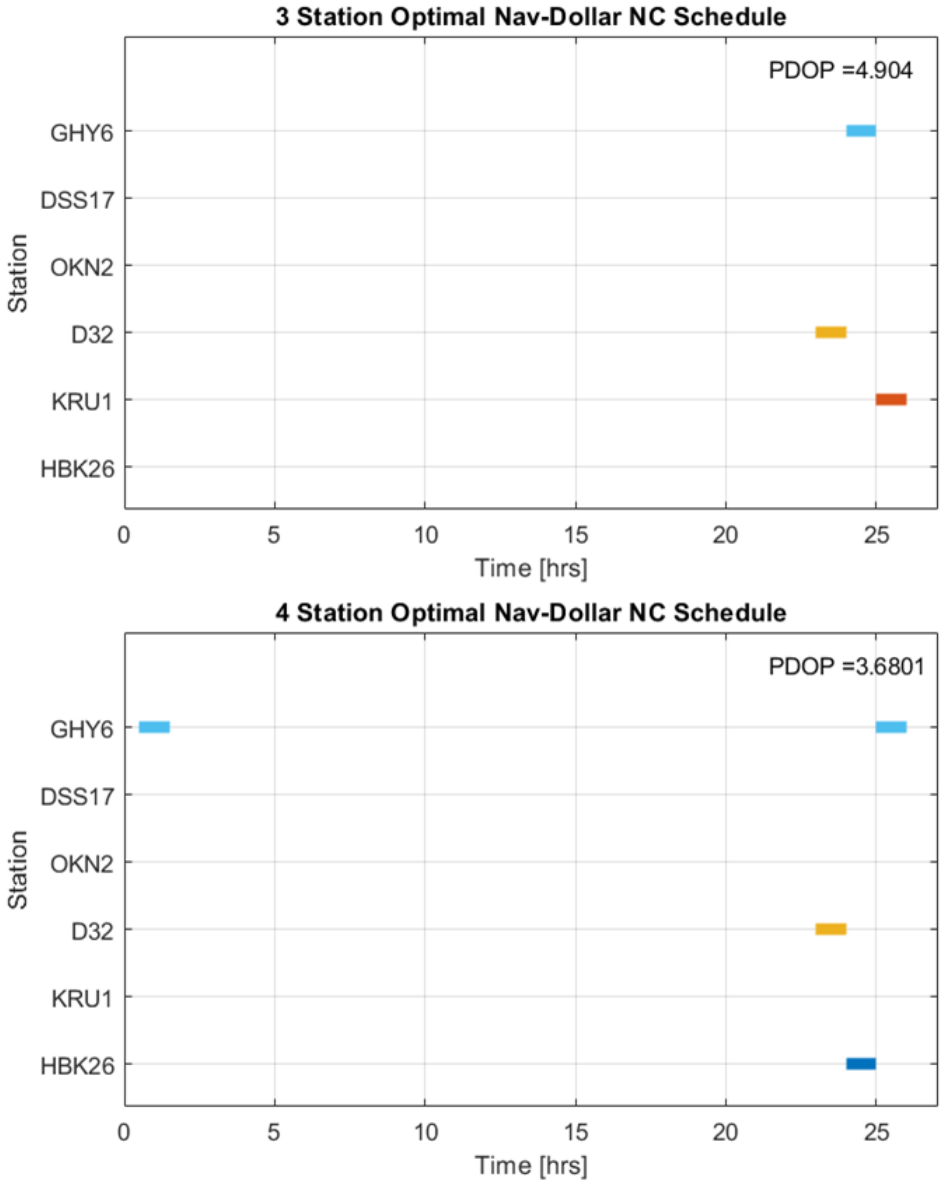

Fig. 10.6: Non-Continuous Nav-Dollars: TCM2-TCM3

Both schedules push stations toward the end; however, the solution with four stations places a segment at the beginning, reducing estimation error growth immediately. Table 10.6 shows the Nav-Dollar comparison to the near-continuous Nav-Dollar schedules:

Table 10.6: Nav-Dollar Schedule Comparisons: TCM2-TCM3

# Stations:	3	4
PDOP:	4.9040 (3.7828)	3.6800 (1.7555)
Nav-Dollars:	7,632 (44,386)	7,286 (21,406)

Figure 10.7 depicts optimal schedules with three and four stations for the OD segment TCM3-LOI:

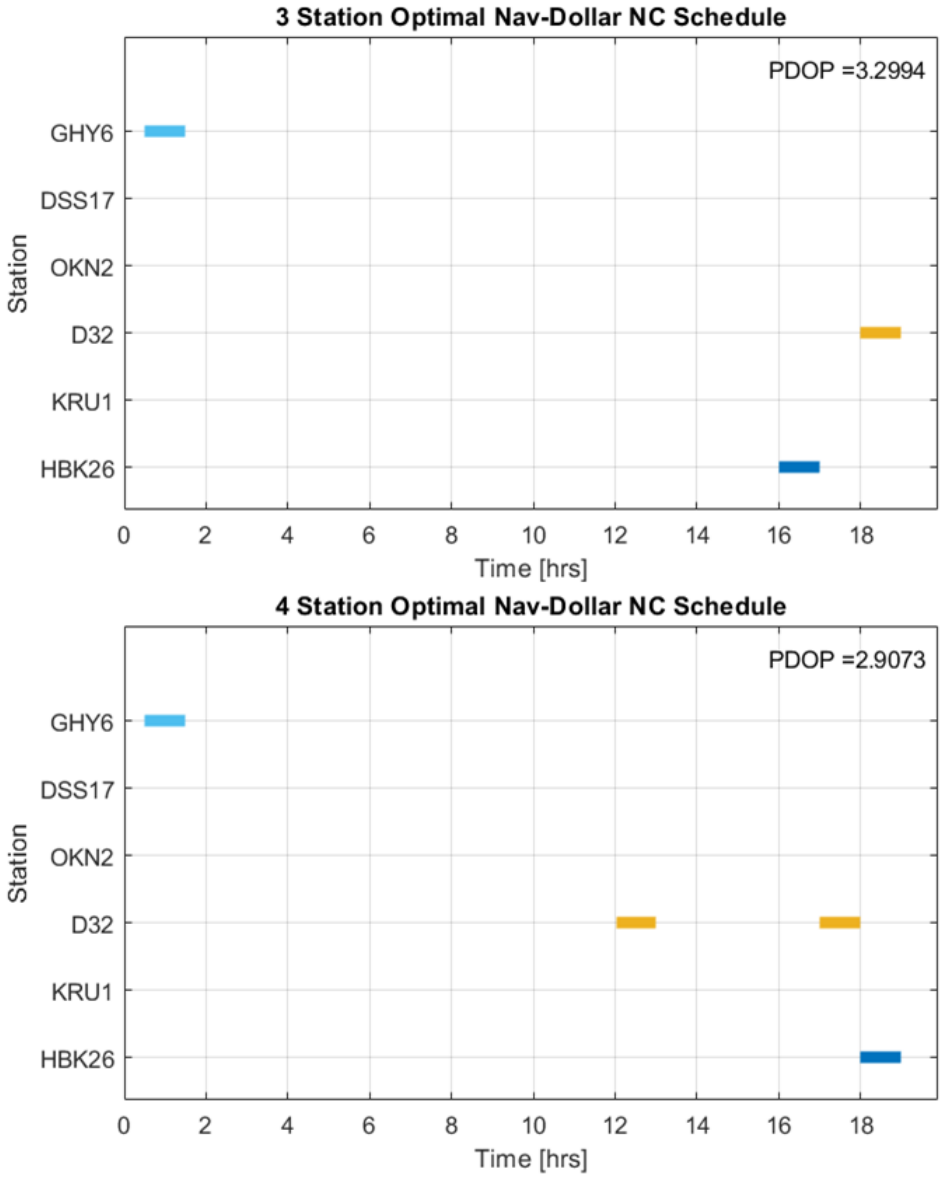

Fig. 10.7: Non-Continuous Nav-Dollars: TCM3-LOI

On lunar approach, the pattern of pushing measurement segments to the end of the OD segment is no longer evident. Table 10.7 shows the Nav-Dollar comparison to the near-continuous Nav-Dollar schedules, shown in blue:

Table 10.7: Nav-Dollar Schedule Comparisons: TCM3-LOI

# Stations:	3	4
PDOP:	3.2994 (3.7828)	2.9073 (1.7555)
Nav-Dollars:	5,345 (15,447)	5,715 (13,477)

10.4 Lunar Orbit Non-Continuous Nav-Dollar Results

Unlike the case where near-continuous Nav-Dollars experiences a restricted solution space in lunar orbit, non-continuous Nav-Dollars does not. Figure 10.8 depicts the optimal non-continuous Nav-Dollar schedules in lunar orbit with a measurement duration of 30 minutes.

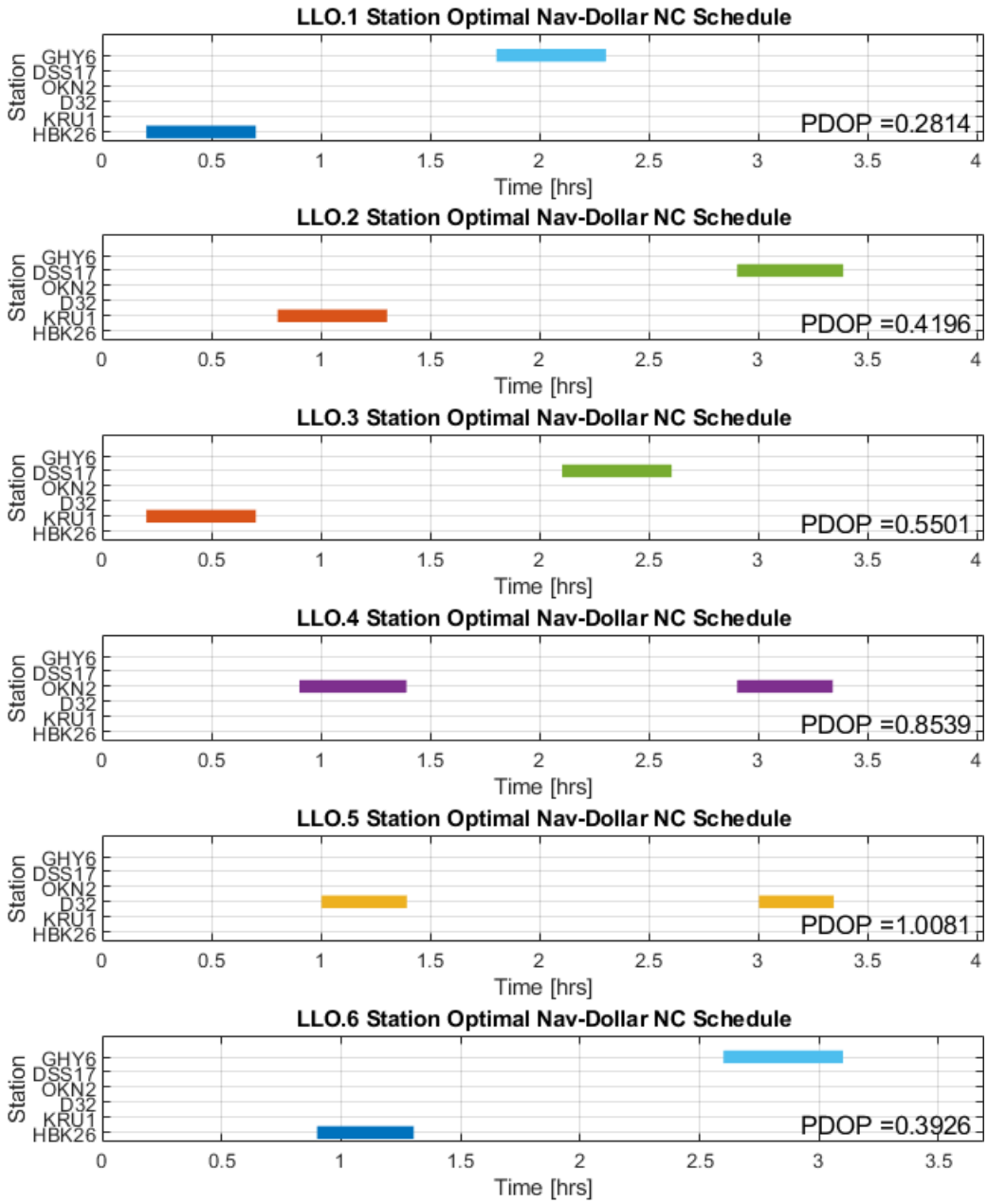

Fig. 10.8: Non-Continuous Nav-Dollars: LLO

Table 10.8 records the Nav-Dollar values from the non-continuous tracking schedules and compares them to the near-continuous tracking case:

Table 10.8: Nav-Dollar (NAVD) Schedule Comparison: LLO

OD Subsegment:	LLO.1	LLO.2	LLO.3	LLO.4	LLO.5	LL0.6
Near-Continuous NAVD:						
Nav-Dollars:	301	664	912	824	468	312
Stations:	HBK26	KRU1	KRU1	OKN2	D32	HBK26
	DSS17	DSS17	DSS17	D32	OKN2	GHY6
Swap Times [hrs]:	0.5	1.5	1.1	3.1	2.5	1.5
Non-Continuous NAVD:						
Nav-Dollars:	177	339	446	607	302	213
Stations:	HBK26	KRU1	KRU1	OKN2	D32	HBK26
	GY6	DSS17	DSS17	OKN2	D32	GHY6
Start Time t_1 [hrs]:	0.2	0.7	0.2	0.9	1.0	0.9
Start Times t_2 [hrs]:	1.7	2.9	2.2	2.9	3.0	2.7

Note how in lunar orbit significant information can be gathered with smaller tracking times. The Nav-Dollars produced are around half of those obtained through the other optimal schedules. As is seen in Fig. 10.8, all PDOP values are either less than 1 or just around 1.

10.5 Non-Continuous Discussion

The clearest pattern in the non-continuous Nav-Dollar study is that for OD segments in deep cislunar space, it is advantageous to place either some or all of the station segments at the end. Doing so provides a significant reduction in PDOP at the end while saving greatly on operational costs. When the dynamics are better defined by the 2-body problem near Earth or the Moon, this patter is not evident.

Furthermore, GHY6 is the most consistently utilized station due to its geographical advantage. GHY6 is also frequently paired with southern stations such as HBK26 or D32 to obtain a sufficient geometry lock. Future work can be done to alter the time in which stations must take measurements, along with how many stations are used. As adding even a fourth station did not always reduce Nav-Dollars, four stations is seen as sufficient for this research.

Non-continuous measurements may be implemented in future lunar missions once Intuitive Machines has developed a significant presence in the industry. Note that despite the PDOP values for non-continuous coverage being larger than other optimization studies , the largest PDOP found was only 4.9040. For ground station networks, the noise on range measurements is unlikely to be greater than $100m$, resulting in a RSS of the position errors of $490m$. Less than half a kilometer of position errors for cislunar estimation is still acceptable.

CHAPTER 11
CONCLUSION AND FUTURE WORK

Various topics have been covered in this thesis research, many of which carry significant conclusions and potential for future work. The main conclusions and takeaways from various chapters are discussed below, including the impact of the LinCov validation and the potential it possesses for future navigation optimization. The conclusions and impact of the DOP algorithm are discussed, and the trends in the optimal tracking schedules are presented.

11.1 Monte Carlo and Linear Covariance Analysis

The importance of Monte Carlo for navigation analysis cannot be understated. The ability to quantify the estimation errors from an EKF and the nonlinear gravitational dynamics and measurements will continue to be a large area of research for the author, Intuitive Machines, and the space industry.

However, the time required to properly analyze EKF estimation performance with a Monte Carlo analysis is time consuming and incredibly ill-suited for ground station optimization. Thus the principles of linearization were introduced and a LinCov tool developed. The LinCov tool on average runs 12,000$\times$ faster than a Monte Carlo analysis, making it ideal for navigation optimization problems.

Before LinCov can be used with confidence in the results, it must be validated through Monte Carlo analysis. While Monte Carlo analysis has previously validated LinCov analysis for cislunar trajectories [17], the research presented represents the first known work to the author in which LinCov has been validated given the exactly the same environment and measurement models.

The Monte Carlo and LinCov analyses incorporated many factors not previously incorporated in other research. First, all station biases and SRP disturbances were modeled as ECRVs, whereas in previous analyses the Monte Carlo tool modeled them as constants

[17]. Second, the gravitational dynamics for both models were the same, incorporating gravitational accelerations from the Sun, Earth, and Moon. The Earth and Moon were modeled with spherical harmonic models, while in previous studies point mass models were used for LinCov. Thanks to the work done by Carlos Roithmayr [33], the gravity gradient partials were correctly implemented to model the Earth as an 8×8 body and the Moon as a 25×25 body. Lastly, both studies implemented Kalman filters, whereas the previous study implemented a batch filter for the Monte Carlo analysis.

With the LinCov tool validated by the Monte Carlo analysis, LinCov can be confidently implemented for cislunar analyses and optimization problems. It is highly likely that LinCov will need to be re-validated for future IM mission trajectories, but this work is a strong indication that LinCov is valid for most cislunar trajectories.

11.2 Optimal Range Measurement Placement

With the validated LinCov tool, the study on optimal range measurement placement was performed. By holding the range-rate schedule constant, constrained range measurements were placed along the tracking schedule and the navigation performance analyzed with LinCov. The final position and velocity errors were analyzed for each possible combination for a one and two segment case.

The placement of one range segment demonstrated a strong linear pattern in the final velocity errors, with the best placement almost consistently occurring at the beginning of the OD segment. More interestingly, the final position errors indicated that station GHY6 in Goonhilly, England was consistently chosen. While this pattern may not be strictly true for all range-rate tracking schedules, it was true for the Benchmark schedule provided by Intuitive Machines.

The placement of two range segments demonstrated that final velocity errors are not as sensitive to the range placement as final position errors. The combination of using GHY6 and HBK26 yielded the optimal final position errors. The clear pattern of emphasizing northern and southern stations with range measurements led to a deeper analysis into Dilution of Precision techniques and analyzing the dynamic measurement geometry.

11.3 Dilution of Precision Methods

The work presented to derive the Dilution of Precision algorithm represents considerable work done by the author and his peers. The generalized Dilution of Precision model from NASA [37] was taken and patterns were carefully recognized to create a recursive DOP model. The recursive model was improved by applying the matrix inversion lemma, thus eradicating the need for constant matrix inversion to calculate PDOP. The implementation of a condition number tolerance ensured numerical stability and result accuracy, allowing for both recursive methods to be implemented together to produce an algorithm that runs approximately 10 times faster than a LinCov analysis.

A weighted DOP analysis was introduced that allowed for a dimensionless PDOP value to be obtained. A ratio between the range and range-rate measurements was implemented, allowing the DOP algorithm to run without knowing specific measurement noise values. Thus the DOP algorithm analyzes solely the dynamic measurement geometry, independent of noise, by incorporating both range and range-rate measurements.

11.4 PDOP Optimal Schedules

The DOP algorithm was embedded into a genetic algorithm to produce optimal tracking schedules that reduced PDOP at final times for key OD segments and subsegments. Optimal tracking schedules with three, four, and five stations were found that reduced PDOP to values beyond a Benchmark schedule that included more stations than the optimal schedules.

The optimization showed key trends in minimizing PDOP. Varying stations in latitude greatly improved the dynamic measurement geometry. Also varying stations in longitude, including the natural rotation of stations, helped reduce PDOP. Ultimately the results indicated that significant information can be obtained with just three stations, outperforming the results obtained from a Benchmark schedule with more stations.

Significant future work with this optimization tool will be done by Intuitive Machines for their lunar missions. Optimal schedules will vary depending on the trajectory, launch date, and available stations. Thus this optimization tool will remain a powerful device for many years and missions to come.

Future analysis is to be considered with different noise ratios k. The work done in this thesis corresponded to $k = 1e^4$. Varying the value of k has already shown to produce different optimal schedules, and selecting the correct k value will be crucial for best performance.

11.5 Nav-Dollar Optimal Schedules

Many continuous tracking schedules produce PDOP values that are acceptable for mission success. Thus the Nav-Dollar metric, derived from maximizing information per dollar, was implemented to create near-continuous and non-continuous tracking schedules. The near-continuous Nav-Dollar schedule demonstrated a pattern of keeping expensive stations for their geographical advantages, while substituting as much time as possible from more expensive stations with cheaper stations.

The genetic algorithm's consistent attempts to minimize Nav-Dollars with as few measurements as permitted led to non-continuous tracking schedules. These non-continuous tracking schedules, while only covering up to 4 hours, reduced the PDOP to acceptable levels for an extremely low operational cost.

Considerable future work is to be done with Nav-Dollars, as Intuitive Machines wishes to save money to promote their commercial payload business. The minimum time required for near-continuous Nav-Dollars will be set at different percentages, and different range-measurement durations implemented for non-continuous schedules.

Ultimately the optimization tool created for this thesis is to be delivered to Intuitive Machines for future use. As the tool can be applied to many trajectories, the work done will continue to arise in many topics and the field of optimal navigation planning will continue to become a more common discussion in the space industry.

REFERENCES

[1] Lincoln J Wood. The evolution of deep space navigation: 1962-1989. *AAS*.

[2] Richard H Battin. *An introduction to the mathematics and methods of astrodynamics*. Aiaa, 1999.

[3] Harold W Sorenson. Least-squares estimation: from gauss to kalman. *IEEE spectrum*, 7(7):63–68, 1970.

[4] BF Cockrell. Rtcc requirements for mission g-lunar module attitude determination using onboard observation. project apollo. Technical report, 1968.

[5] C Christensen and S Reinbold. Navigation of the mariner 10 spacecraft to venus and mercury. In *Mechanics and Control of Flight Conference*, page 844, 1974.

[6] RK Russell and J Ellis. Orbit determination for a jupiter orbiter tour of the galilean satellites. *Journal of Spacecraft and Rockets*, 12(6):368–373, 1975.

[7] Bob van Noort. The gravity of titan: Analysis of cassini's doppler tracking data and solar radiation pressure. 2021.

[8] P Axelrad, RG Brown, BW Parkinson, and JJ Spilker. Gps navigation algorithms. *Global Positioning System: Theory and applications.*, 1:409–433, 1996.

[9] Richard B Langley et al. Dilution of precision. *GPS world*, 10(5):52–59, 1999.

[10] Rudolph Emil Kalman. A new approach to linear filtering and prediction problems. 1960.

[11] Peter S Maybeck. *Stochastic models, estimation, and control*. Academic press, 1982.

[12] Gary Bishop, Greg Welch, et al. An introduction to the kalman filter. *Proc of SIGGRAPH, Course*, 8(27599-23175):41, 2001.

[13] David Geller. Traditional linear covariance analysis.

[14] David C Woffinden and David K Geller. Relative angles-only navigation and pose estimation for autonomous orbital rendezvous. *Journal of Guidance, Control, and Dynamics*, 30(5):1455–1469, 2007.

[15] M Benjamin Rose and David Geller. Linear covariance techniques for powered ascent. In *AIAA guidance, navigation, and control conference*, page 8175, 2010.

[16] Timothy Crain and Robert Bishop. Mars entry navigation: atmospheric interface through parachute deploy. In *AIAA Atmospheric Flight Mechanics Conference and Exhibit*, page 4501, 2002.

[17] Quinn Moon and David Geller. *American Astronautical Society.*

[18] Catherine L Thornton and James S Border. *Radiometric tracking techniques for deep-space navigation.* John Wiley & Sons, 2003.

[19] Timothy Pham, Jason Liao, EJ Wyatt, Benjamin Malphrus, Jeffrey Kruth, Robert Kroll, Michael Combs, Tobias Gedenk, Sarah Wilczewski, Jacob Lewis, et al. System development and spacecraft testing of the morehead state university ground station. 2019.

[20] Bob Schutz, Byron Tapley, and George H Born. *Statistical orbit determination.* Elsevier, 2004.

[21] Quinn P. Moon and Joel Getchius. Ground station tracking scheduling, Sep 2022.

[22] Christian Fuchs and Florian Moll. Ground station network optimization for space-to-ground optical communication links. *Journal of Optical Communications and Networking*, 7(12):1148–1159, 2015.

[23] Eylem Erdogan, Ibrahim Altunbas, Gunes Karabulut Kurt, Michel Bellemare, Guillaume Lamontagne, and Halim Yanikomeroglu. Site diversity in downlink optical satellite networks through ground station selection. *IEEE Access*, 9:31179–31190, 2021.

[24] Quinn Moon, David Geller, and John Graves. Ground station costs and connections, Jun 2022.

[25] VJ Rayward-Smith. Combinatorial optimization by william j. cook, william h. cunningham, william r. pulleyblank and alexander schrijver, wiley, new york, 1998. isbn 0-471-55894-x. no. of pages: 355. price:£ 24.95., 1998.

[26] Mengchun Xie, Koki Furuya, and Mitsutoshi Murata. Study on solving the tsp using the slime mold algorithm including partial solutions.

[27] John H Holland. Genetic algorithms. *Scientific american*, 267(1):66–73, 1992.

[28] Adam Wuerl, Tim Crain, and Ellen Braden. Genetic algorithm and calculus of variations-based trajectory optimization technique. *Journal of spacecraft and rockets*, 40(6):882–888, 2003.

[29] Joseph Kopacz, Jason Roney, and Roman Herschitz. Optimized ground station placement for a mega constellation using a genetic algorithm. 2019.

[30] Charles H Lee and Kar-Ming Cheung. Mixed integer programming & heuristic scheduling for space communication networks. In *2012 IEEE Aerospace Conference*, pages 1–10. IEEE, 2012.

[31] Matthew Bolcar, J Scott Smith, and David Aronstein. Recursive branching simulated annealing algorithm. Technical report, 2012.

[32] Sung Wook Paek, Sangtae Kim, and Olivier de Weck. Optimization of reconfigurable satellite constellations using simulated annealing and genetic algorithm. *Sensors*, 19(4):765, 2019.

[33] Carlos M Roithmayr. Contributions of spherical harmonics to gravitational moment. *AIAA Journal*, 57(10):4291–4299, 2019.

[34] NASA. Spice concept: https://naif.jpl.nasa.gov/naif/spiceconcept.html.

[35] Navigation filter best practices. Technical report, 2018.

[36] The MathWorks Inc. Matlab version: 9.13.0 (r2022b), 2022.

[37] Obed S Sands, Joseph W Connolly, Bryan W Welch, James R Carpenter, Todd A Ely, and Kevin Berry. Dilution of precision-based lunar navigation assessment for dynamic position fixing. In *Proceedings of the 2006 National Technical Meeting of The Institute of Navigation*, pages 260–268, 2006.

[38] T.K. Moon and W.C. Stirling. *Mathematical Methods and Algorithms for Signal Processing*. Prentice Hall, 2000.